SILICON NANOWIRES BY METAL-ASSISTED CHEMICAL ETCHING AND ITS INCORPORATION INTO HYBRID SOLAR CELLS

by

SFISO ZWELISHA KHANYILE

A thesis submitted in fulfilment

of the requirements of the degree of

Doctor of Philosophy

In the

DEPARTMENT OF PHYSICS AND ASTRONOMY

UNIVERSITY OF THE WESTERN CAPE

Supervisor: **Prof. C. J. Arendse, University of the Western Cape**

Co-Supervisors: **Prof. C. Oliphant, National Metrology Institute of South Africa**

Prof. P. Miceli, University of Missouri

March 2021

DEDICATION

This thesis is dedicated to:

The loving memory of my late loving father

Samson Enock Khanyile

And

My loving and caring mother

Agnes S`bongile Khanyile

KEYWORDS

"SILICON NANOWIRES BY METAL-ASSISTED

CHEMICAL ETCHING AND ITS INCORPORATION

INTO HYBRID SOLAR CELLS"

Solar cells

Photovoltaics

Silicon Nanowires

Metal assisted chemical etching

Doping

Polymer

Poly(3-hexylithiophene-2, 5-diyl)

Fullerene

Photoluminescence

Hybrid solar cells

ABSTRACT

"SILICON NANOWIRES BY METAL-ASSISTED CHEMICAL ETCHING AND ITS INCORPORATION INTO HYBRID SOLAR CELLS"

S. Z. KHANYILE

PhD Thesis, Department of Physics and Astronomy, University of the Western Cape

The rapid increase in global energy demand in recent decades coupled with the adverse environmental impact of conventional fuels has led to a high demand for alternative energy sources that are sustainable and efficient. Renewable solar energy technologies have received huge attention in recent decades with the aim of producing highly efficient, safe, flexible and robust solar cells to withstand harsh weather conditions. c-Si has been the material of choice in the development of conventional inorganic solar cells owing to it superior properties, abundance and higher efficiencies. However, the associated high costs of Si processing for solar cells have led to a gravitation towards alternative organic solar cells which are cheaper and easy to process even though they suffer from stability and durability challenges. In this work, combination of both inorganic and organic materials to form hybrid solar cells is one of the approaches adopted in order to address the challenges faced by solar cell development.

This work began with the successful fabrication and doping of inorganic silicon nanowires (Si NWs) using the metal assisted chemical etching method. Properties of these Si NWs were investigated and found to have diameters ranging from about 80 to 200nm with a crystalline core and amorphous shell structure. enhanced photoluminescence emission peaks were observed from the doped NWs as a result of structural artefacts acting as recombination centres for emission. Enhanced antireflective properties were also observed from these NWs with reflectivity values below 2% which ideal for solar absorption in photovoltaic applications. The doping of these Si NWs was

also found to enhance the electron transport properties as exhibited by the improved conductivity values of the doped versus intrinsic NWs. The successful doping of these Si NWs was further confirmed by the presence of both n and p type bonds in the analysed samples.

The organic materials used in this work were based on a conjugated polymer and fullerene blend consisting of poly(3-hexylithiophene) (P3HT) and [6,6]-phenyl C_{71}-butryc acid methyl ester (PCBM). Successful fabrication of photoactive inorganic/organic hybrid thin films and hybrid solar cell devices was achieved by incorporating the previously n-doped Si NWs into a P3HT:PCBM matrix. The impact of varying the Si NW load ratio and the effects of different NW dopant levels were investigated in order to realize optimal performance from such inorganic/organic hybrid architectures.

The variation of the amount of Si NWs in the organic matrix, was found to exhibit a nonhomogeneous thin film with evenly distributed Si NWs which formed random clusters which increased with the load. Furthermore, high resolution transmission microscopy was employed to investigate the interfacial interaction between the Si NWs and the polymer/fullerene blend. Structural information obtained from the grazing incidence XRD (GIXRD) showed minimal peak shifting with varying Si NW ratios indicative of strain on the hybrid thin film. Chemical analysis from X-ray photoelectron spectroscopy did not show the presence of Si due to sensitivity limitations however broadening of the polymer peaks was observed. UV-Vis absorption of the hybrid thin films was found to improve with the addition of Si NWs while the photoluminescence quenching also increased due to the addition of doped Si NWs. Improved mobility and conductivity of the hybrid thin films was observed upon the addition of Si NWs.

The impact of different dopant levels of Si NWs was investigated and exhibited a uniform nanowire distribution for all samples while an increase in PL emission with increasing dopant level was observed and enhanced UV-Vis on the highly doped sample. Hall-effect measurements showed significant increase in conductivity with increasing dopant concentration while there was a less significant drop in carrier mobility as the dopant concentration increased. These observations correlated very well with the J-V characteristics whereby the highly doped sample yielded the highest PCE with a significant gain of over 100% compared to sample without Si NWs.

DECLARATION

I declare that,

"SILICON NANOWIRES BY METAL-ASSISTED

CHEMICAL ETCHING AND ITS INCORPORATION

INTO HYBRID SOLAR CELLS"

is my own work, that has not been submitted for any degree or examination in any other university and that all the resources I have used or quoted have been indicated and acknowledged by means of complete references.

Signed: Date: March 2021

SFISO ZWELISHA KHANYILE

ACKNOWLEDGEMENTS

Mvelinqangi, nani nonke boKhanyile, oNgwane, Mthiyane, mlonjana o Sogodi, omahlab`inkom engayidli anik`abafokazana, ngiyabonga ukuba nami kuloluhambo olude oluze lwaba yimpumelelo.

I wish to express my sincere heartfelt gratitude towards the following people and organisations without whom this phenomenal piece of work would have not been a success. This would be done in no particular due to their combined contributions towards the success of this work:

My main Supervisor, Prof. Christopher Arendse (Department of Physics, University of Western Cape), for excellent supervision, encouragement and expertise in the field.

My co-supervisor Prof. Clive Oliphant (National Metrology Institute of South Africa), for his dedication, continuous support, supervision and the daily interactions.

My co-supervisor Prof. Paul Miceli (University of Missouri), for his support, supervision, mentoring and training offered during research visits to different laboratories.

The Materials Characterization (NMISA) colleagues, for their continued support, encouragement and access to state of the art facilities.

The management and staff of the UWC Physics Department.

The Solid-State Research group (UWC) colleagues for hosting me during research visits and those lab after hours with Siphesihle Magubane.

My mother, brothers, sisters and my partner for supporting me emotionally and financially.

My close friends and colleagues from the NMISA and UWC for encouraging me during tough times.

Special thanks to Katlego Tlholoe from NMISA (HCD) for her sincere and unwavering support throughout this journey.

The National Metrology Institute of South Africa (NMISA) and the National Research Foundation (NRF) for financially supporting this project.

TABLE OF CONTENTS

LIST OF FIGURES

LIST OF TABLES

LIST OF ACRONYMS

AgNPs	Silver Nanoparticles
BHJ	Bulk heterojunction
EDS	Electron dispersive X-ray spectroscopy
EFTEM	Energy-filtered transmission electron microscopy
Eq	Equation
FF	Fill factor
GIXRD	Grazing incidence X-ray diffraction
HAADF	High-angle annular dark field
HOMO	Highest occupied molecular orbital
HRTEM	High resolution transmission electron microscopy
ITO	Indium tin oxide
J_{sc}	Short-circuit current density
LUMO	Lowest unoccupied molecular orbital
MACE	Metal assisted chemical etching
OSC	Organic solar cell
P3HT	Poly(3-hexylthiophene)
PCBM	Phenyl-C71-butryl acid methyl ester
PCE	Power conversion efficiency
PEDOT:PSS	Poly(3,4-ethylenedioxythiophene) poly(styrenesulfonate)
PL	Photoluminescence spectroscopy
R_s	Series resistance
R_{sh}	Shunt resistance
SEM	Scanning electron microscopy
Si NCs	Silicon nanocrystals
Si NWs	Silicon nanowires
STEM	Scanning transmission electron microscopy
UV-Vis	Ultraviolet-visible spectroscopy
V_{oc}	open-circuit voltage
XPS	X-ray photoelectron spectroscopy

Chapter 1

Introduction and Overview

1.1 Global Energy Outlook

The constantly increasing global energy demand causes the rapid depletion of fossil fuel reserves, which are to a large extent still the main energy source, especially for developing nations. The generation of energy from fossil fuels have contributed to adverse environmental effects such as global warming (climate change). Renewable energy technologies such as solar energy, have received huge public interest as a viable alternative and have seen rapid development in the last decade [1.1]. Presently, 80% of the global energy consumption is from fossil fuels such as oil and coal which can be directly linked to the rampant water/air pollution and climate change through greenhouse gas emissions [1.2]. As a result of population and economic growth, the energy demand increases drastically making it impossible for the fossil reserves to meet future energy demands and this compels the exploration of other sustainable alternative energy technologies such as, wind, solar, geothermal, biodiesels and biomass energy sources. In the past few decades, solar energy power has emerged as one of the most promising renewable energy sources that could be explored and developed extensively in order to address the ever-increasing energy demand.

There have been several attributes identified which render solar energy as the most viable alternative energy technology such as abundance, free availability and no pollution. Some parts of the world such as Africa can receive as much as about 2500 hours of sunshine per year with a high solar irradiation average of about 220 W/m^2 for most southern African regions compared to the 150 W/m^2 and 100 W/m^2 received by the USA and Europe respectively [1.3]. This abundance of solar energy has been the main drive behind the research interests in the development of newer and efficient solar photovoltaic (PV) technologies of harvesting solar energy in order to address current and future global energy demands.

In recent times, the solar PV industry has grown considerably to become one of the mainstream electricity sources unlike a few decades ago whereby solar PV could only be realised in small scale applications for gadgets and off-grid household applications. The rapid growth of the global cumulative installed capacity is evident on the growth from 5 gigawatt (GW) in 2005 to 177 GW in 2014 [1.4]. Since then, the cumulative installed capacity has seen an exponential growth to about 480 GW in December 2018 as published by the International Renewable Energy Agency (IRENA) following a 94.2 GW capacity injection in 2018 alone compared to a 71.4 GW capacity addition observed in 2016 [1.5].

As reported in the Renewable Capacity Statistics 2019, Asia is the largest continental contributor to cumulative installations with about 274.6 GW whereby, China at 175 GW leads followed by Japan-55.5 GW, India-26.8 GW, South Korea-7.8 GW, Thailand-2.7 GW and lastly Taiwan with 2.6 GW. Europe comes in as the second largest contributor to the total cumulative installations with a combined 119.3 GW followed by a 55.3 GW contribution from North America while Oceania and Africa make about 10 GW and 5.1 GW respectively. Lastly, the South and Central America together with the Caribbean contribute about 7.1 GW combined to the total global cumulative installed capacity [1.6].

From the published solar PV statistics, it is evident that China has become the leaders in solar PV by a wide margin followed by Japan and USA in a fierce contest while Germany rests at fourth place. These statistics display an exponential growth of China while Germany experienced a decline in growth which may have been heavily influenced by the change in political landscape and support. Furthermore, most European, American and Japanese solar PV manufacturers have since experienced fierce competition from Chinese rivals which have now become the main suppliers of

PV modules. Furthermore, emerging markets such as South Africa, Mexico, Chile Turkey, have greatly influenced the dominance of China as a leading solar PV supplier/manufacturer due to the rapid growth of the solar PV market in these countries.

In South Africa, solar PV`s have seen tremendous growth and popularity owing to its low running costs and being one of the affordable small-scale forms of electricity generation [1.7]. Within Africa, South Africa has been identified as the largest solar market with an installed capacity of about 2.5 GW followed closely by Egypt with its rapidly growing solar PV market [1.7]. A report published by the IRENA in 2019 showed that Egypt, South Africa, Kenya, Namibia and Ghana are the primary drivers in the African continent with a combined newly installed PV capacity of 1067 MW [1.8].

On average, South Africa receives over 2500 hours of sunshine per year with an average solar irradiation range between 4.5 – 6.5 KWh/m^2 , making it one of the most readily available and sustainable resource for electricity generation [1.9]. A report by Mordor intelligence shows an expected compound annual growth rate of 10% by the solar PV market in South Africa between 2018 and 2025 and this accelerated growth is linked to the several cost cutting measures by the solar industry [1.9]. Furthermore, increased electricity demand, environmental sustainability awareness and the basic need for stable energy supply are some of the factors promoting the solar PV market amid the load-shedding problem in South Africa.

Several measures have been undertaken by the South African government to promote the growth of the solar industry which include the deregulation of private sector power generation and accelerated licencing of independent power producers in order to achieve the 5000 MW target for Eskom`s generation capacity plan [1.10].

However, with the presence of the covid-19 pandemic, huge declines in terms of growth and targets are projected as result of slow economic activity and other factors associated with the current global pandemic. Some reports have earmarked small scale generations such as roof top projects to boom and boost the overall installed capacity in a bid to bridge the supply and demand gap withing the South African solar market [1.9].

Irrespective of the advantages of solar energy and the tremendous growth in cumulative installed capacity, solar PV still forms a small percentage of the global electricity production scale [1.4]. This indicates that even though there has been considerable growth observed, there are still limiting factors prohibiting effective solar PV deployment. One of the main limitations for solar PV is the initial capital costs involved which always tend to be higher due to high costs of solar panels and sophisticated energy storage facilities. The long payback period of solar PV has also been one of the factors scarring away investments from corporations and individuals.

As much as most solar PV devices are silicon (Si) based which is abundantly available, the costs of Si wafer technology where purification and processing of the raw Si into efficient and stable solar devices with unique properties remains very high. For the longest time since the 1950`s, crystalline Si based solar cells have dominated the solar PV industry. Currently the highest recorded c-Si solar efficiency stands at 26,7% [1.11,1.12] achieved in 2017 which is very close to the theoretically predicted limit of about 29%. This milestone has been achieved as result of heavy research dedicated to high efficiency and low-cost solar PV modules.

Interestingly, it can be noted that the successful implication of a solar PV industry is not just solely dependent on the economic landscape but also hinges on government

policies and the political will to shape up the solar PV future. Several areas of development that have been identified include, grid infrastructure, energy storage facilities and conducive agreements that incentivize different stakeholders to partake in the future of PV`s globally.

1.2 The Photovoltaic Effect (PV)

The photovoltaic effect is a phenomenon that describes processes which involve the conversion of sunlight (photo) energy into electrical (voltage) energy and this phenomenon was discovered by French physicist by the name of Edmond Becquerel in 1839 [1.13]. He discovered that illuminating metal (platinum) electrodes immersed into a conductive solution with white light resulted in current production. Light in its nature consists of small packets of energy called photons and when these energetic photons strike a photovoltaic material, ground state electrons get excited and some are released leaving holes behind while the free charges get collected on the electrodes to produce electricity.

In more detail, the photovoltaic effect consists of four steps namely, light absorption, charge formation, charge transport and lastly charge collection [1.14]. In semiconducting materials, incident light waves (photons) get absorbed, and the energy of the absorbed photons is dependent on the band gap and extinction coefficient of the semiconducting material. For inorganic semiconductors, when photon energy absorption occurs, ground state electrons get excited resulting in free charge carriers leaving holes behind while for organic semiconductors both the electron and hole pair exist in an energy bound state called an exciton. This exciton requires a certain large amount of energy to result in the dissociation and formation truly free charge carriers [1.15] which are ready for the charge transportation stage. During charge transport, free carriers are transmitted through charge pathways within

the semiconductor medium towards the electrodes where they get collected or extracted.

The efficiency of charge transportation can be easily degraded by artefacts such as defects which become charge traps or barriers hindering efficient movement of charge carriers through the semiconducting medium and resulting in poor photovoltaic performance. Therefore, enhancing charge transport properties of a material can help achieve better photovoltaic performance. The last process involved in a photovoltaic process is charge collection. At this stage the transported charges are extracted from the semiconducting material through the cathode or anode electrode interface. This interface between the electrode and semiconducting material is very crucial and should be optimized for resistance free flow of the specific charge carriers.

1.3 Brief History of the Photovoltaic Solar Cell

The astounding photovoltaic effect discovery by Edmund Becquerel in the 1830s marked the birth of solar cell development. Since then, several works conducted on the subject by various researchers leading to several patents and great strides in the development of solar cell knowledge. In 1876, about four decades after the PV effect was observed from an electrolytic solution, William Adams and Richard Day also realised the PV effect from selenium placed between platinum electrodes marking the first solid-state PV device [1.16].

About 20 years later in 1894, the first large area solar cell was made by Charles Fritts whereby he sandwiched the selenium with gold and another metal. This was followed by huge interests and lots of works done in exploring materials such as copper/copper oxides and lead/thallium sulphide thin film structures. The basic structure of all these solar cells was; metal electrode / semiconductor/ semi-transparent thin metal contact leading to a Schottky barrier device. This architecture

had several limitations such as poor light transmission through the semi-transparent contact and let to power conversion efficiencies below 1%.

In the 1950s, the development of silicon electronics resumed, and ways of fabricating p-n junctions were discovered. These p-n junction structured silicon devices exhibited much better photovoltaic response than the previous Schottky barrier devices and this led to the first silicon solar cell in 1954 by Chapin, Fuller and Pearson. This silicon solar cell had a power conversion efficiency of about 6% [1.17]. Consequently, this milestone sparked new interests to explore other materials such as gallium arsenide, cadmium telluride and indium phosphide in the quest for higher efficiencies as predicted theoretically. However, these newer promising materials also had their disadvantages such as high toxicity levels, scarcity of materials and high production costs and this ensured that silicon-based devices remained the beacon of hope for PV technology [1.18].

A global oil crisis in the 1970s ensured that more efforts and research resources were channelled towards developing better PV devices and processing methods that were efficient and cost effective [1.19]. Several improvements in silicon thin film technology were achieved for both amorphous and microcrystalline Si in order to reduce production costs. Furthermore, to increase the efficiency, tandem structure and semiconductor band gap modifications were explored in order to improve the efficiencies and provide an alternative to fossil fuels. However, the costs involved remained higher than the fossil fuel prices. Form the 90`s throughout to the 2000`s the pressure to find alternative energy sources mounted. Besides the oil prices and strain on fossil fuels, new environmental issues linked to global warming further revived the interest towards PV technologies and this led to a huge shift towards green energy by most governments. In the first decade of the 2000s, solar PV technologies showed

rapid growth and continues to grow at an exponential rate from 2010 till to date. This is evident even from the all-time highest record efficiencies of 26.7% that's quickly approaching the theoretical limit of solar cells.

1.4 Solar Cell Categories

Solar cells can be categorized into three different categories based on the nature of the base materials used during their fabrication. Solar cells can be fabricated from inorganic materials such as Si, Zn, Cd etc, organic materials such as polymers and can also be a combination of both inorganic/organic materials to form hybrid solar cells.

Inorganic solar cells are those solar cells which are based on high quality inorganic materials which are stable and efficient such as silicon which can be microcrystalline or polycrystalline, copper indium gallium selenide (CIGS), cadmium telluride and many more. Over the years, silicon has emerged as the most dominant material in the PV industry since it has been studied extensively as a material while manufacturing and processing technologies have been well optimized over the last few decades. Other advantages of silicon over its counterparts include its abundancy in nature as a raw material, being non-toxic and having a wide range of other good properties that may not be directly for PV beneficiation. However, even though the processing techniques for Si have been developed, the huge problem of the high costs involved in processing silicon as a raw material into a final PV device hinder the widespread and full-blown dissemination of solar PV technology globally.

Organic solar cells are solar cells based on conductive organic polymer materials. Organic materials have since been extensively investigated owing to their promising properties of offering cheaper, lighter and flexible solar cells. These organic solar cells have a vast range of applications on flexible substrates that can be used on

windows, walls and still be foldable for easy storage. However, the drawbacks of these devices include poor electrical properties which prevent them from achieving higher efficiencies. Structurally, they have been found to be very unstable and require careful encapsulation since they degrade quickly when directly exposed to environmental conditions such as light and moisture or humidity.

Hybrid solar cells are a new generation of solar cells which come as a result of extensive research and innovative work that seeks to combine the two convectional types of solar cells in order to have them coexist in one PV module complementing each other. In this cell, organic and inorganic materials are reconciled in such a way that the drawbacks of each are countered by the presence of the other material hence the name hybrid. This "new" type of solar cells has received a lot of interests from researchers since both types have been studied extensively and are well understood in the scientific community. As indicated earlier, poor electrical properties of organic materials can be improved by the inclusion of highly conductive inorganic nanostructured materials with superior charge-carrier transport properties. Furthermore, organic solar cells can be fabricated by spin coating or printing over larger flexible surfaces at an even lower cost than conventional inorganic solar cells. The most common hybrid architecture involves the use of inorganic nanostructures such as nanowires or nanoparticles which get embedded in an organic medium [1.20]. Latest developments in hybrid solar cells have resulted in perovskite solar cells that have even reached efficiencies of about 20% within a short period of time since inception [1.21,1.22].

1.5 Motivation and Objectives of Thesis

Despite the great progress made in the development of efficient solar cells over the years, high production costs associated with these solar cells remains as the main challenge which affects accessibility to this wonderful technology. Considerable progress has been achieved in the field of materials science and more specifically nanotechnology in order to have a deeper and well-informed understanding of materials that can be used to produce cheaper and more efficient solar cells. The developments in nanotechnology have enabled researchers to understand the unique properties of nanostructured materials and their applications.

The focus of this thesis is on hybrid thin films for solar PV applications which have been found to be a cheaper alternative to c-Si yet more stable than conventional organic thin films. In comparison to a conventional solar cell system, hybrid solar cell systems based on Si have several advantages which include improved performances and cost-effective production methods that can reduce costs by up to 15% [1.23]. These advantages are relevant to developing countries like South Africa whereby there's a need for accelerated growth of alternative power production methods to ensure stable power supply for economic growth and other developments.

Hybrid solar cell technology has been one of the initiatives by scientist to mitigate challenges faced by either inorganic or organic solar cells. As much as the incorporation of nanostructures into organics has yielded promising results [1.24], a great need to find nanostructured materials which improve the electrical properties of such hybrid architectures still exists. This exercise can also be used to improve on the stability of most organic solar cells which are known to degrade rapidly [1.25].

Silicon nanowires have been identified as the best candidate material to circumvent such challenges owing to their superior optical absorption properties and

electrical properties which can enhance charge separation and transport significantly. It is for these reasons that this work focuses on the incorporation of silicon nanowires into organic solar cells to enhance their photovoltaic performance.

A summary of the objectives of this work are presented as;

(i) Synthesis of dense n-type Si NW arrays using a low-cost top-down method known as the metal assisted chemical etching (MACE) technique. This method is described in detail in the following chapters (chapter 2 and chapter 3). The fabricated Si NW properties will be characterized and investigated with various appropriate techniques. The optimal etching time and NW length shall be investigated and optimized. Furthermore, potential solar PV application of the as-synthesized NW arrays will be explored in detail.

(ii) Synthesis of photovoltaic organic thin films that will be mixed with Si NWs of optimal length as established in objective (i) to form hybrid organic/inorganic thin films. In this instance, the optimal Si NW load ratio on the organic matrix will be investigated and optimized for hybrid solar cell performance.

(iii) Investigate the effect of different Si NW dopant levels on the performance of the hybrid solar cells fabricated. After establishing the optimal Si NW load ration from (ii), Si NWs doped at different will be mixed with the organic material at the optimal ratio and be investigated for hybrid solar cell performance.

References

[1.1] REN21.2019, Renewables 2019 Global Status Report; Web page: https://www.ren21.net/wp-content/uploads/2019/05/gsr_2019_full_report_en.pdf

[1.2] G. Marland, J. Ind. Ecol. 12(2) (2008).

[1.3] R. Gouws, T. Lukhwareni, Int. J. Phys. Sci. 7(48) (2012) 6169-6180

[1.4] International Energy Agency – Photovoltaics Power Systems Programme. A snapshot of global PV markets 2014.

[1.5] International Energy Agency – Renewable Statistics Report 2018

[1.6] E. Bellini, Global Cumulative Capacity tops 480 GW, IRENA says. (2019); Web page:https://www.pv-magazine.com/2019/04/02/global-cumulative-pv-capacity-tops-480-gw-irena-says/

[1.7] T. Hendriks, Op-ed: The future of solar energy in the south African context. (2020); Web page: https://www.esi-africa.com/industry-sectors/renewable-energy/op-ed-the-future-of-solar-energy-in-the-south-africa-context/#_ftn1

[1.8] ESI – Africa, The big 5 – Africa`s fastest growing solar energy markets. (2019); Web page: https://www.esi-africa.com/industry-sectors/renewable-energy/the-big-5-africas-fastest-growing-solar-energy-markets-2/#:~:text=According%20to%20the%20International%20Renewable,installed%20PV%20capacity%20in%202018.

[1.9] Mordor Intelligence, South Africa photovoltaic market – Growth, trends, and forecasts (2020-2025). (2020); Web page: https://www.mordorintelligence.com/industry-reports/south-africa-solar-power-market-industry

[1.10] Eskom Media statement. September 2020; Web page: https://www.eskom.co.za/news/Pages/2020Sep14.aspx

[1.11] K. Yoshikawa, H. Kawasaki, W. Yoshida, T. Irie, K. Konishi, K. Nakano, T. Uto, D. Adachi, M. Kanematsu, H. Uzu, K. Yamamoto, Nat. Energy. 2 (2017) 17032.

[1.12] L.C. Andreani, A. Bozzola, P. Kowalczewski, M. Liscidini, L. Redociri, ADV. PHYS-X. 4(1) (2018) 1548305.

[1.13] T. Markvart, Ed., Solar Electricity, John Wiley & Sons, Chichester, U.K., (1994).

[1.14] S.R. Forrest, MR S Bull. 30 (2005) 28-32.

[1.15] M. Knupfer, Appl. Phys. A: Mater. Sci. & Proc., 77 (2003) 623-626.

[1.16] Y. N. Sudhakar, M. Selvakumar, D. Krishna Bhat, Bio-polymer Electrolytes-fundamentals and applications in energy storage. (2018); Web page: https://www.sciencedirect.com/science/article/pii/B9780128134474000017

[1.17] E. Lorenzo, Solar Electricity: Eng. Of Photovoltaic System. (Progrensa, 1994).

[1.18] D. A. Anderson, Clean Electricity from Photovoltaics. (London Imperial College Press, 2001).

[1.19] J. Pinkse, D. Van den Buuse, Energy Policy. 40 (2012) 11-20.

[1.20] L. He, C. Jiang, D. Lai, H. Wang, Rusli, App. Phys. Lett. 99 (2011) 021104.

[1.21] A. Kojima, K. Teshima, Y. Shirai, T. Miyasaka, J. Am. Chem. Soc. 131(17) (2009) 6050-6051.

[1.22] W. S. Yang, J. H. Noh, N. J. Jeon, S. Ryu, Y. C. Kim, J. Seo, S. I. Seok, Science. 348 (2015) 1234-1237.

[1.23] H. Movla, F. Sohrabi, A. Nikniazi, M. Soltanpour, K. Khalili, Solar Cells – New aspects and Solutions, InTech, (2011) 397-414.

[1.24] B. V. R. S. Subramanyam, P. C. Mahakul, K. Sa, J. Raiguru, I. Alam, S. Das, M. Mondal, S. Subudhi, P. Mahanandia, Sol. Energy. 186 (2019) 146-155.

[1.25] A. Seemann, T. Sauermann, C. Lungenschmied, O. Ambruster, S. Bauer, H. J. Egelhaaf, J. Hauch, Sol. Energy. 85 (2011) 1238-1249.

Chapter 2

Literature Review

Abstract

A detailed literature review is presented that covers the basic principles underlying the operation of a basic solar cell and solar cell parameters. Furthermore, a discussion of silicon materials in photovoltaics and organic materials is presented. Lastly, the interaction between organic and inorganic materials for hybrid solar cell structures is discussed.

2.1 Basic Solar Cell Theory

2.1.1 Solar cell principle of operation

A solar panel is used to harness solar energy from the sun and convert it to electrical energy. A solar panel consists of a collection of even smaller sub-units called solar cells which are interconnected to produce the collective output power of the solar panel. The key processes responsible for converting photo energy incident onto the solar cell into electrical energy include: photo absorption, charge separation/ transport and charge collection at the electrodes. Conventionally, a solar cell is made up of semiconducting materials which are oppositely doped such that there is a potential difference when the two materials are brought in close contact. In a silicon (Si) solar cell, oppositely doped Si layers are brought in close contact whereby one layer has a high concentration of electrons and referred to as the n-layer while the other layer has a higher concentration of holes and referred to as the p-layer. In order to achieve a n-doped Si layer, Si is doped with a group V element such as phosphorous (P) which has an extra electron that remains as a negative free charge carrier moving in the conduction band resulting in a n-type semiconductor. Similarly, to achieve p-type Si, a group III element such as boron is used since it has 3 valence electrons and one vacancy known as a hole [2.1]. Upon bonding with Si, the vacant “hole” remains as a free positive charge carrier hence the p-type. When these layers are brought together

in contact, a p-n junction is created at the interface resulting in the formation of an inbuilt electric field and this electric field force is responsible for electron-hole pair separation and charge transportation within the solar cell.

When the n- and p-type Si layers are brought to contact, a difference in carrier concentration is created across the p-n junction at the interface resulting in the diffusion of charge carriers which try to balance the charges on opposite sides of the junction. This means that holes close to the junction from the p-type diffuse into the n-type side leaving negatively charged ions. Similarly, electrons from the n-type side diffuse across the junction into the p-type side leaving positively charged ions on the n-type side closer to the interface junction. These opposite static charges at the junction result in an electric field which counters the diffusion process by repelling majority carriers from either side of the junction and this leads to a charge carrier depleted region around the p-n junction also known as the space charge region (SCR) or space charge layer (SCL).

The localized electric field force at the p-n junction acts in opposite directions for charges of different polarity and this results in the retention of electrons within the n-type material while the holes are retained in the p-type material thus preventing further "diffusion" of charge carriers. This means that the "diffusion" and "drift" currents cancel each other until an equilibrium is reached whereby an electric field is formed across the p-n junction. This built-in electric field is responsible for the diode behaviour of the junction since it allows electrons to only flow from the p-type material to the n-type material only.

When light photons are incident on a solar cell, the semiconducting material absorbs only those photons with energy larger than the bandgap energy of that semiconductor. During this process, atoms absorb these photons and electrons are

ejected resulting in the formation of electron-hole pairs which move within the semiconducting material. When these electron hole pairs are within the vicinity of the SCL, the localized electric field acts on the electron-hole pair such that the electron is attracted into the n type layer while the hole gets attracted into the p-type layer as a result of the diode behaviour and this process is known as charge dissociation. This results in additional charge carriers on the n- and p-side of the junction which can be extracted by connecting metal electrodes on both the n- and p-regions such that electrons and holes can flow out to an external circuit. It is through such mechanisms that a solar cell can deliver power output to an external circuit as a product of current and voltage which also result from the flow of electrons and built-in electric field, respectively.

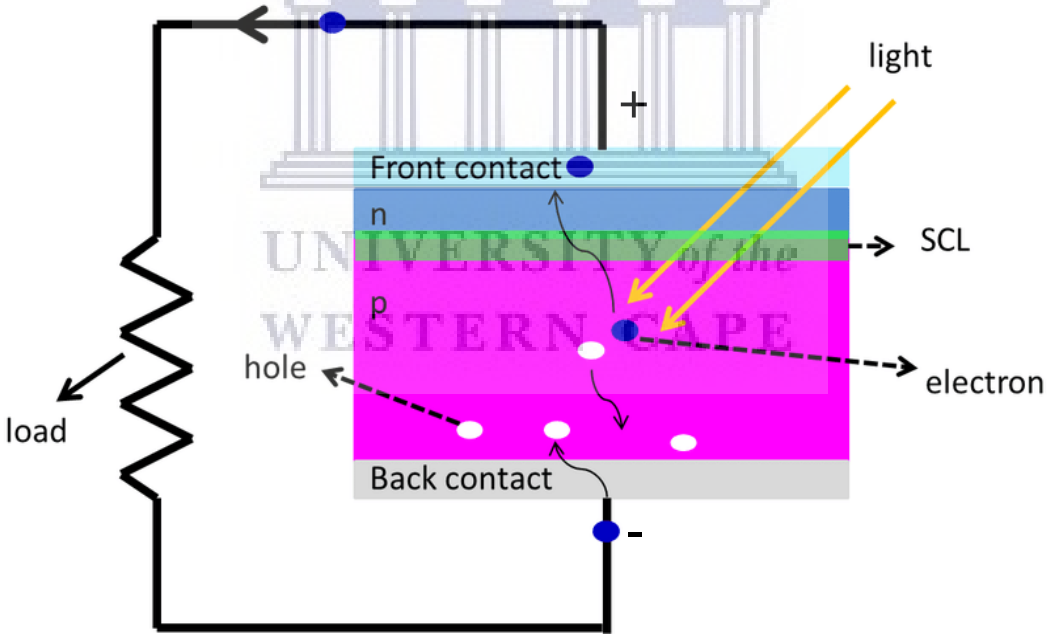

Figure 2.1: Solar cell schematic showing the p-n junction [2.2].

2.1.2 Solar cell parameters

The preceding discussion clearly shows how a solar cell can exhibit diode characteristics, and it is for that reason that an “ideal” solar cell can be depicted as a current generator coupled in parallel with a diode to maintain unidirectional flow of the

generated current. However, experimentally it has been established that an actual solar cell cannot be ideal as described above due to the existence of other electrical properties that co-exist with current and voltage. These properties are the series resistance and shunt (parallel) resistance. In a Si solar cell, the series resistance can be attributed to the; (i) contact resistance between the metal electrodes and the Si. (ii) the actual resistance of the top and bottom contacts. (iii) the actual bulk resistance of the semiconducting materials used to make the solar cell.

On the other hand, shunt resistance of a solar cell can be attributed to current leakage through the p-n junction and poor insulation around solar cell edges which may provide alternatives path for current leakage instead of the desired electrodes. A schematic depicting a solar cell circuit with a current generator, diode and the resistance is shown in figure 2.2.

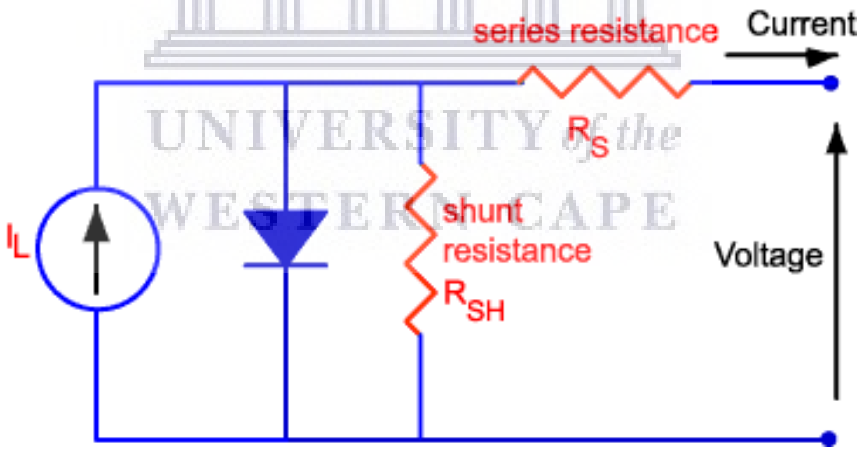

Figure 2.2: Solar cell circuit model [2.3].

Having established the presence of series and shunt resistance properties of a solar cell, the current (I) and voltage (V) characteristics can be given by the expression in eq. (2.1) below:

$$I = I_L - I_0 \left(\exp\left[\frac{q(V+IR_{series})}{nk_BT}\right] - 1\right) - \frac{V+IR_{series}}{R_{shunt}} \qquad (2.1)$$

Where by I_L represents the photo-current from the solar cell, I_0 is the saturation current of the diode, V being the voltage across the solar cell electrodes, k_B is the Boltzmann's constant, q is the electron charge, n is ideality factor, T represents temperature, R_{series} is the series resistance of the cell and R_{shunt} is the shunt resistance of the solar cell.

The performance of a solar cell and the quality of the p-n junction can be quantified by the following basic solar cell parameters such as the: open circuit voltage (V_{oc}), short circuit current density (J_{sc}), fill factor (FF) and the conversion efficiency (η). These solar cell parameters can be extracted from the graphical presentation of the solar cell`s current-voltage characteristics known as the J-V curve. These characteristics are obtained under dark and illuminated conditions, whereby it exhibits diode behaviour in the dark state while varying voltage without light illuminating the solar cell and the curve passes through the origin as shown in figure 2.3. Under illumination the J-V curve gets shifted from the origin by an amount equivalent to the photo current generated by the solar cell.

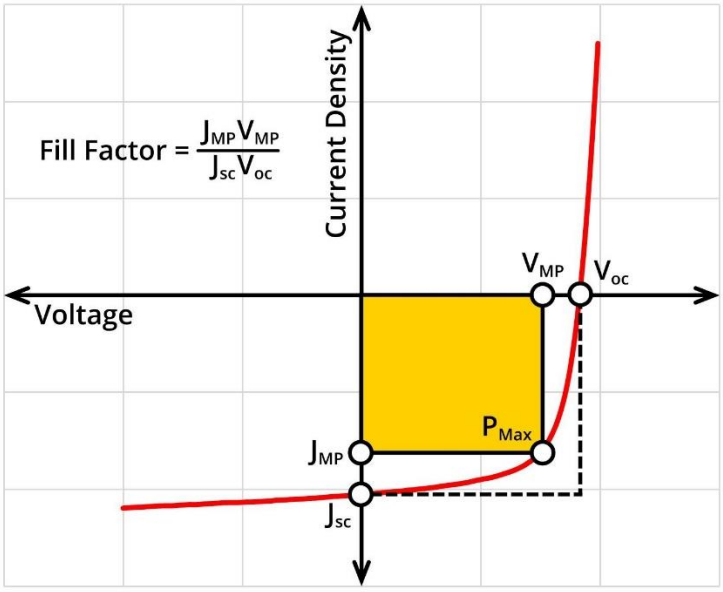

Figure 2.3: J-V curve of a solar cells [2.4].

The short circuit current density (J_{sc}) of the solar cell refers to the current flowing through the solar cell when it is short-circuited and can be determine from the curve intersection with the y-axis at zero voltage. The open-circuit voltage (V_{oc}) is the maximum voltage provided by a solar at zero current and can be obtained where the curve intersects the x-axis under illumination. In figure 2.3, the FF of a solar cell quantifies the "squareness" of the J-V curve which is the ratio of maximum power obtained P_{max} and the maximum theoretical power P_{th}. Since P_{max} and P_{th} are obtained at (J_{mp}, V_{mp}) and (V_{oc}, J_{sc}) respectively, the FF can therefore be defined as the ratio of solid and dashed line rectangles as shown if figure 2.3 and given by eq. (2.2):

$$FF = \frac{V_{mp} \cdot J_{mp}}{V_{oc} \cdot J_{sc}} \qquad (2.2)$$

Generally, the performance of solar cells can be quantified and compared using their power conversion efficiency (η) which determines the overall quality of the solar cell. This parameter can be defined as ratio of the maximum power P_{max} output to that of the incident power P_{in} source as shown in eq. (2.3):

$$\eta = \frac{P_{max}}{P_{in}} = \frac{V_{mp} \cdot J_{mp}}{P_{in}} = \frac{V_{oc} \cdot J_{sc} \cdot FF}{P_{in}} \quad (2.3)$$

Clearly, it can be observed from the above equation that efficiency is unitless quantity which can be expressed as a percentage. The accurate measurement of efficiency requires a set of standard test conditions (STC) to be met and these include: a solar irradiance of 1000 W/m^2, temperature of 25 ℃ and an air mass of AM1.5. These conditions and measurement can be achieved in a laboratory setup using a solar simulator with filters to simulate solar irradiation.

2.2 Silicon materials and photovoltaics

Amid the latest developments in PV technologies, the global solar PV market is still highly dominated by Si based wafer solar cells by over 90% [2.5]. The observed Si dominance can be attributed to several inherent factors such as the high abundancy of Si on earth with a bandgap of about 1.12 eV which is well-matched for efficient PV conversion and it is nontoxic with high stability. Furthermore, Si technologies form the core of the current existing chemical and semiconductor microelectronics industries [2.6]. Structurally, Si is a semiconducting group 4 element which consists of a *diamond lattice* crystal structure made up of two overlapping FCC Bravais lattices forming a tetrahedral structure. In more detail, this tetrahedral structure can be described as a body centred cubic structure without four (4) of its corner atoms as shown in figure 2.4. Furthermore, this configuration ensures that each atom has 4 covalent bonds with four equidistant neighbours forming the basic unit of a Si lattice as shown.

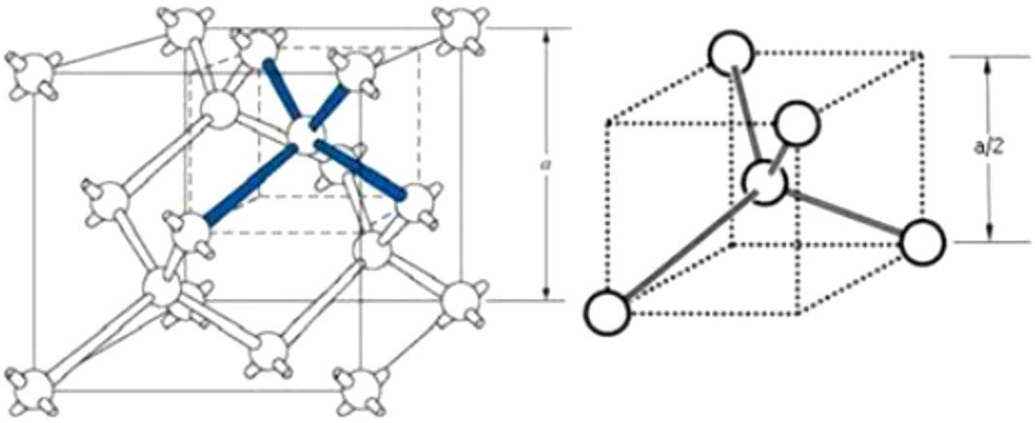

Figure 2.4: Si crystal structure showing lattice constant a, the Si–Si bonds and atomic arrangement [2.7].

The crystal lattice shown in figure 2.4 represents an intrinsic Si crystal lattice without impurities or dopants. However, since Si is a semiconducting material, it can therefore be doped using impurities to become an extrinsic semiconductor and hence altering its natural properties. Si doping involves shifting of the electron-hole balance through introduction of species either with one more or one less valence electron leading to n-type or p-type Si, respectively. To produce n-type Si, group V elements such as phosphorous (P) with 5 valence electrons can be used to form 4 covalent bonds with Si leaving one free extra electron that becomes a charge carrier for conduction. This results in more electrons in the conduction band than the number of holes in the valence band leading to a negative net charge for carrier hence the “n-type”. For p-type Si, a group III element such as boron with 3 valence electrons is used as a dopant material. Upon doping, the group III element only has 3 electrons available to bond with the Si which requires to form 4 covalent bonds. The electron deficiency of the dopant results in the formation of hole which then leads to an overall positive net carrier charge due to more holes in the valence band. In a doped semiconducting material, the type of charge carrier with a higher number is referred to

as a “majority carrier” while the lower concentrated type is referred to as the “minority carrier”.

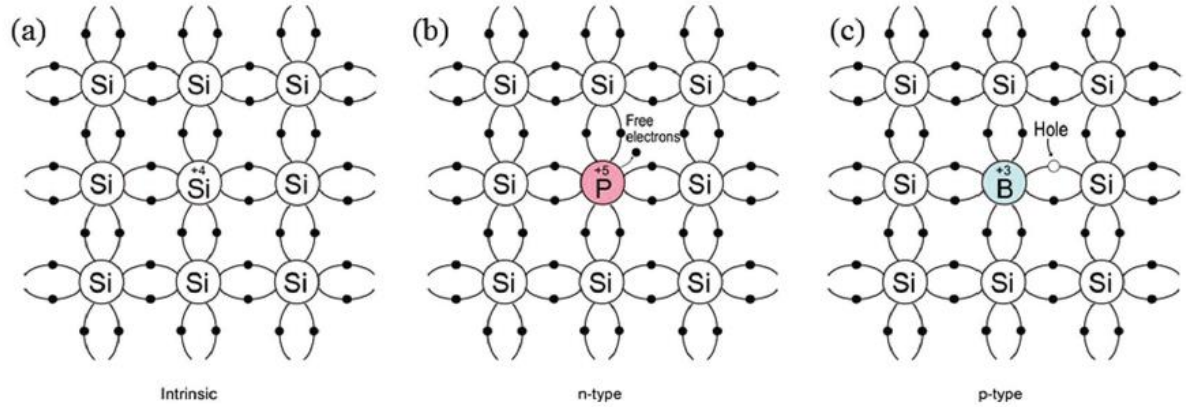

Figure 2.5: The schematic structure of (a) intrinsic, (b) n-type and (c) p-type Si [2.1].

The schematics shown in figure 2.5 depict the structural schematic of Intrinsic, n type and p type Si as previously explained. In n-type semiconductors, the extra electrons are donated into the conduction band hence n-type dopants can be referred to as donors. For p-type, the dopant accepts electrons from neighbouring atoms hence they are acceptors. In semiconductors, the band theory shows that the addition of dopant impurities alters the band structure of that semiconductor such that new energy levels are created within the band gap of the semiconductor. In a n-type semiconductor, an electron energy level closer to the conduction band is created such that the free electrons can be easily excited into the conduction band and this is called the donor level. This results in an effective Fermi level shifting to midway between the donor and conduction band. In a p-type semiconductor, acceptor impurities are added, creating a low energy acceptor level for holes very close to the valence band such that electrons can easily be excited from the valence band to the acceptor level leaving mobile holes within the valence band as charge carriers. This further results in the shift

of the effective Fermi level to between the hole level and valence band as shown in figure 2.6.

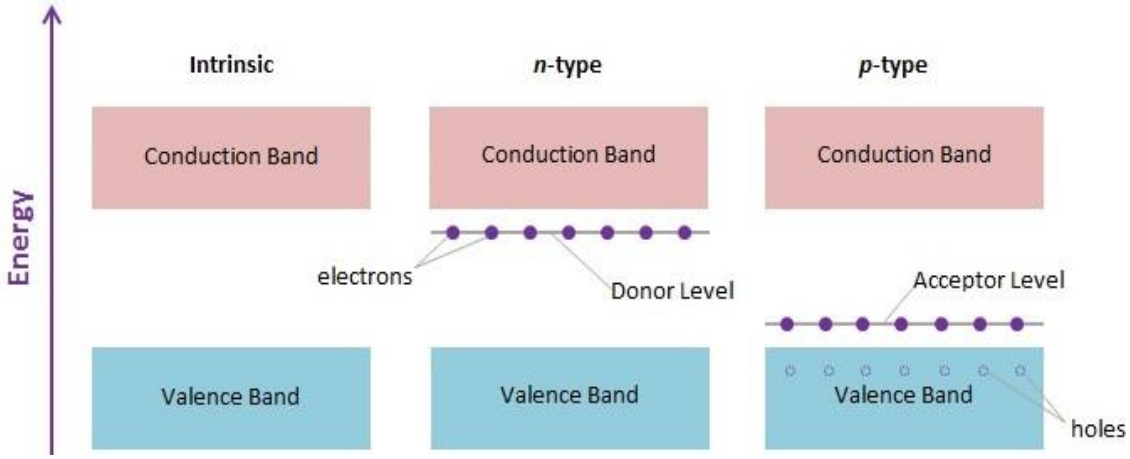

Figure 2.6: Energy bands of an intrinsic, n-type and p-type semiconductor [2.8].

2.2.1 Nanostructured silicon materials for photovoltaics

In recent years, several nanostructured Si architectures such as, nanowires [2.9-11], nanorods [2.12-13] and nanoparticles [2.14] have drawn enormous attention as candidates for efficient energy conversion materials due to their superior properties than their bulk Si counterparts such as physical, chemical, electrical and optical properties etc. The superiority of nanostructured Si materials emanates from the ability to tune their properties based on their size and shape (high aspect ratio).

2.2.2 Silicon nanowires, fabrication and properties

Silicon nanowires (Si NWs) can be identified as one-dimensional thin hair-like structures with diameters below 100 nm and a length that can range from nanometres to a few micrometres [2.15]. These novel structures have received tremendous growth and attention from researchers in a bid to improve fabrication methods, properties and the applications of such structures [2.16]. Several approaches have been developed

for the growth of Si NWs and these methods can be categorized as top down or bottom-up methods as shown in figure 2.6. Top-down approaches include dry reactive ion etching (RIE) [2.17-18] and wet chemical etching techniques [2.19] while bottom-up approaches comprise of vapour-liquid-solid (VLS) growth [2.20-21], chemical vapor deposition (CVD) [2.22] and plasma enhanced CVD (PECVD) [2.23-24] methods.

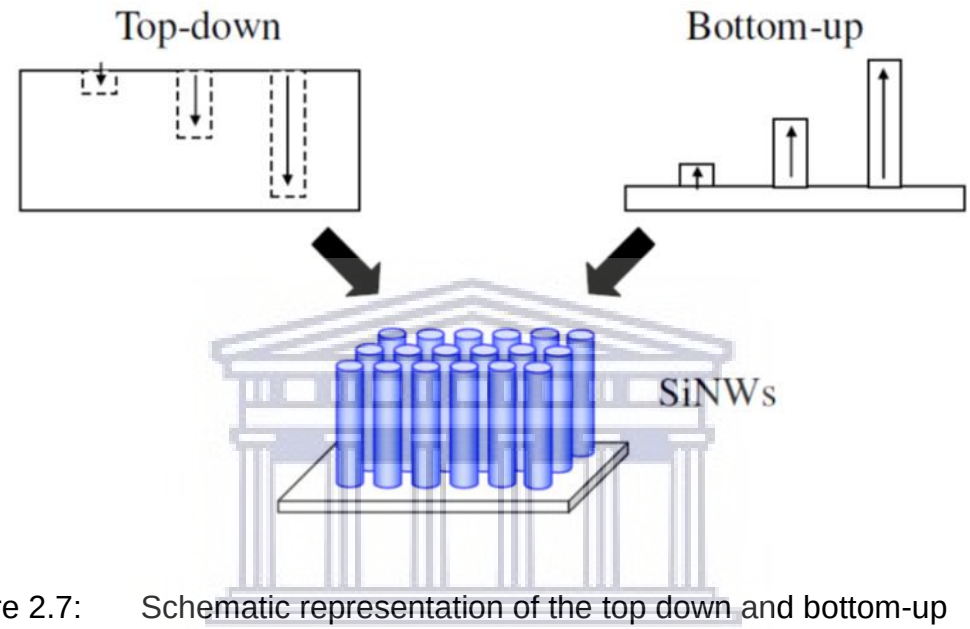

Figure 2.7: Schematic representation of the top down and bottom-up approaches [2.25]

2.2.3 Bottom-up methods

Most bottom-up techniques such as CVD involve the growth of Si NWs from the basic atomic level into one-dimensional structures from different Si precursors. There have been several Si NW growth techniques that have been developed based on this approach and these include thermal evaporation, CVD, laser ablation, solution-based growth, molecular beam epitaxy (MBE), and magnetron sputtering. Among these techniques, the main differentiator is the type of Si precursor used for each growth technique. In laser ablation, a solid Si-Fe target is used as a precursor while solution-based techniques use monophenylsilane ($SiH_2C_6H_8$) as the precursor for one dimensional NW growth. The most common CVD growth techniques utilise Si vapor

precursor gases such as silane (SiH_4), silicon tetrachloride ($SiCl_4$) and even Si powders that can be thermally activated [2.26].

The bottom-up growth of Si NWs from atomic scale up to one-dimensional structures can be ascribed to several growth mechanisms which include: vapour-solid-solid (VSS), vapour-liquid-solid (VLS), solid-liquid-solid (SLS), solution-liquid-solution, oxide-assisted growth (OAG), sulphide-assisted growth and template-based growth. Of all these mechanisms, the VLS growth mechanism is one of widely used growth mechanisms [2.27] to produce high quality crystalline Si NWs with minimal structural defects and this can be attributed to the high ability to control and optimize growth conditions [2.28]. In order to achieve monocrystalline Si NW growth from VLS, the crystallinity of the metal catalyst has a direct influence on the NW crystallinity while an etched c-Si substrate is used to achieve epitaxial grown Si NWs. a schematic presented in figure 2.8 shows the processes involved in VLS growth.

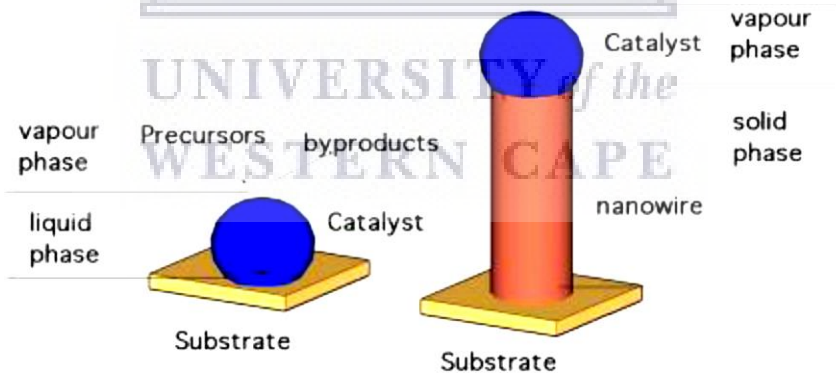

Figure 2.8: Schematic of the VLS process [2.29].

The bottom-up approaches such as VLS, OAG etc, have exhibited a high capability to produce Si NWs of small diameters of about 1 nm with Ma et al. achieving 1.3 nm using OAG method during thermal evaporation of SiO_2 powder [2.30].

2.2.4 The top-down approach

In this method, a Si substrate or an existing layer of Si is sculpted to form one-dimensional Si nanostructures via lithographic or etching techniques. The etching methods can be classified into two categories being a dry and wet etching process whereby the former includes techniques such as reactive ion etching (RIE) and metal-assisted chemical etching (MACE) for the latter. The RIE technique is a microfabrication process that combines the use of reactive chemical species and direct ion bombardment on the Si wafer in order to achieve anisotropic Si structures. The combination RIE and lithography at low plasma pressures of about 10-100 mTorr can be used to achieve better control of the size and density of a Si NW array while maintaining the original dopant levels of starting Si wafer [2.31-33]. However, these dry etching techniques can be time consuming, require complex vacuum systems and costly optical equipment while they still result in rough structures due to surface damage caused by ion bombardment [2.34].

Wet chemical etching techniques such as the MACE method [2.19] have received great attention and development in recent years for industrial applications. The MACE method is a simple, low-cost method that can be used to produce high aspect ratio Si NW arrays over larger areas using liquid chemicals without the need for complex and costly equipment needed for RIE. This method employs a noble metal catalyst that can either be Au, Pt, Ag, Pd and Cu [2.35-36] which facilitate the etching of Si material at the catalyst/Si substrate interface leading to vertical etching and formation of one-dimensional structures.

2.3 Metal-Assisted Chemical Etching of Silicon Nanowires

During MACE, a Si wafer substrate is cleaned and then immersed in a noble metal containing solution such as HF-$AgNO_3$ in order to initiate metal deposition on

the wafer whereby the silver (Ag) catalyses the etching process in the oxidant/HF solution. This coating process can be classified as a galvanic process [2.37-39] while the etching process comprises of a series of cathodic and anodic reactions.

The coating process begins with the extraction of electrons from the Si wafer surface onto the silver ions (Ag^+) contained in the $HF/AgNO_3$ solution which then results in the formation of negatively charged Ag ions nucleating and localising at the Si surface (figure 2.9 (a)). Further Ag^+ in solution preferentially get attracted to the already negatively charged Ag nuclei instead of the uncovered Si surface to get more electrons which consequently leads to formation of larger Ag nanoparticles (Ag NPs) as more Ag^+ accumulate as shown in figure 2.9 (b). The size and distribution density of these Ag NPs are highly dependent on the duration of this process and these two factors have a direct bearing on the Si NW geometry. Extended coating durations can result in the formation of a continuous Ag layer which will bar the etchant solution from reaching the Si surface [2.40].

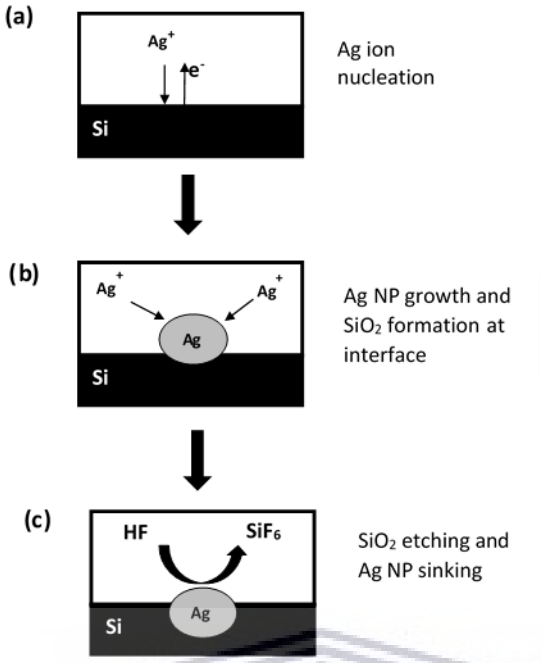

Figure 2.9: Schematic showing the (a) Nucleation of Ag NPs (b) Ag NP growth and (c) Etching of Si wafer as Ag NP sinks [2.40].

During the etching process, the Ag NP coated Si wafer is exposed to an etchant solution consisting of a mixture of HF/H_2O_2 whereby the H_2O_2 reacts with Ag to form an unstable oxidant compound AgO(OH) which oxidizes the interfacial Si (anodic reaction) to form SiO_2 that gets etched by the HF acid. In more detail, the surface of the metal catalyst (Ag NPs) becomes the cathode whereby the oxidant is reduced (cathodic reaction) such that holes (h^+) are injected from metal catalyst to Si while electrons (e^-) move from Si to the catalyst via the interface. This leads to an interfacial Si that is highly oxidized (SiO_2) and has a high hole concentration which consequently gets dissolved by the HF acid leaving an etched layer below the catalyst. Thus, the Ag NPs dig deeper into the Si wafer resulting in the formation of Si NWs. The etching direction of the Ag NP is anisotropic and occurs along preferred crystal orientations and temperature dependant [2.41]. Once the desired length of Si NWs is achieved,

the Ag NPs are dissolved in a strong nitric acid solution resulting in a clean Si NW array.

2.3.1 Etching rate and direction

Several works done on the MACE of Si NWs have been able to show that the etching rate is directly proportional to the etching duration. In earlier studies, Cheng et al. successfully demonstrated that the etching rate and duration have a linear relationship under uniform etching conditions [2.42] such as etchant concentration and temperature. Furthermore, in other investigations, it was successfully demonstrated that NPs of different shapes with same surface area result in a uniform etching rate whereby smaller NPs showed a higher etching rate [2.43].

The chemical etching of a Si wafer involves a bond breaking process whereby the strength of the back-bonds has a direct bearing on the etching rate and direction hence the MACE direction can be explained using the bond-breaking theory [2.44]. Typically, Si exhibits anisotropic back-bond strength along different crystal orientations such that each atom has two and three back-bonds on the (100) and (110/111) planes, respectively [2.45]. Therefore, the <100> etching direction has been found to be the most preferential for the MACE of Si as demonstrated in other works [2.46]. However, Si NWs with non <100> orientations, such as the <110> and <111> direction, have been obtained from p-type Si (100) as evident from the work of Chem et al. [2.47]. These observed anomalies were a result of varying etchant concentration ratios ($HF:H_2O_2$) which consequently led to further weakening of back-bond strength at higher oxidant concentrations [2.48].

There have been various factors and experimental conditions that have been found to influence etching direction in MACE of Si wafers. An in-depth understanding

of the chemical reactions resulting in such variations is necessary to achieve desired Si NW growth direction and establish relation between HF concentration, etching direction and Si wafer type. As mentioned previously, the back-bond strength of the Si type together with the [HF]:[oxidant] ratio have a direct influence on the etching rate and direction. During wet chemical etching of Si (111), a low oxidant concentration ratio in the etchant solution leads to etching along the <100> direction while at sufficiently high oxidant concentrations, the etching occurs along the vertical <111> direction as shown in figure 2.10 [2.49]. At low oxidant concentrations, the dominant surface termination of the Si wafer starts off as Si–H which then progressively changes to Si–OH with increasing the oxidant content and eventually becomes SiO_2 at sufficiently high oxidant concentrations. The SiO_2/Si-OH presence at the etching site results in a weakened back-bond strength effect hence making non-<100> etching directions possible [2.50].

However, a Si (100) substrate displays an opposite relation to the [HF]:[oxidant] ratio than that of Si (111). During MACE of a Si (100) wafer, etching along the <100> direction is achieved at low oxidant ratios due to the least number of Si atoms to be etched along the (100) plane while increasing the oxidant ratio results in etching along other non-<100> directions with more Si surface atoms such as <110> and <111> [2.51].

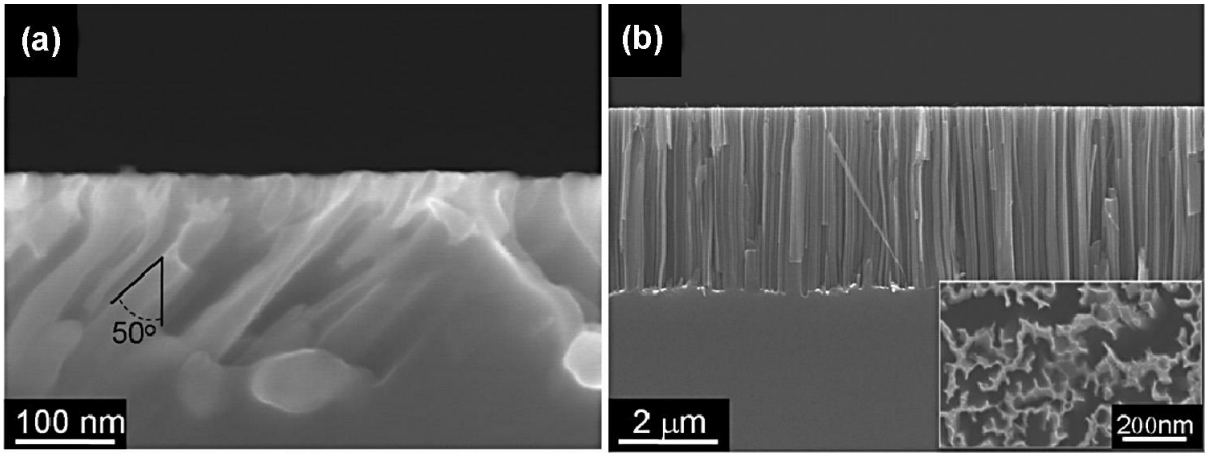

Figure 2.10: Si (111) wafer etching along (a) <100> and (b) <111> direction [2.49]

2.3.2 Porosity in MACE Si NWs

The formation of porous Si NWs during MACE fabrication has since gained huge interests from researchers due to the need for understanding the porosity mechanism and controlling it. Several mechanisms have been proposed to explain the pore formation in Si NWs when heavily doped Si is etched via MACE.

To date, porous Si NWs have been realised from both heavily and lightly doped Si wafers whether p- or n-type [2.50]. In one of his works, Hochbaum et al. suggested that the formation of porous Si during MACE is an electrochemical mechanism like the conventional electrochemical method of forming porous Si [2.52]. However, the main distinction is that, during MACE, the porosification is driven by the continuous reduction of Ag^+ while in conventional electrochemical process it is induced by an applied bias on the electrical back contacts. Increased dopant levels in p-type Si result in a decrease in the energy barrier at Si/electrolyte interface because the Ag^+ / Ag^0 potential is below the valence band of Si. This means that under a constant potential, the lower energy barrier allows more charge flow resulting in more roughness and high porosity in etched Si nanostructure [2.52]. Furthermore, due to the insulating nature of

porous-Si, the holes (h^+) cannot be transported across the energy barrier except the Ag^+ / Ag^0 redox agents which can diffuse through the etched pores [2.53].

In other works, Qu et al. proposed a different mechanism to explain the formation of porous Si NWs whereby the dissolution and re-deposition of Ag was identified as the main cause of porosity [2.54-55]. During etching, high concentrations of H_2O_2 can result in high rates of Ag^+ ion dissolution and in-turn lead to the ions not being fully re-absorbed back to their original nuclei but remain suspended in solution. When the Ag^+ concentration in the solution reaches a certain threshold, nucleation of these Ag^+ may occur at defect sites on the sidewalls of already etched Si NWs. Localised lateral or random etching can therefore occur at these defect sites leading to porosification of Si NWs [2.50].

2.3.3 Optical properties of Si NWs

Efficient solar energy harvesting has been one of the challenges in solar cell development whereby a huge portion of incident solar radiation is reflected from the surface and not trapped within the solar cell resulting in absorption losses. These absorption and transmission losses are very crucial factors which have a negative impact on the overall power conversion efficiency (PCE) of the solar cell. However, these reflection and transmission losses can be circumvented by the incorporation of anti-reflective and light trapping capable materials such as Si NWs.

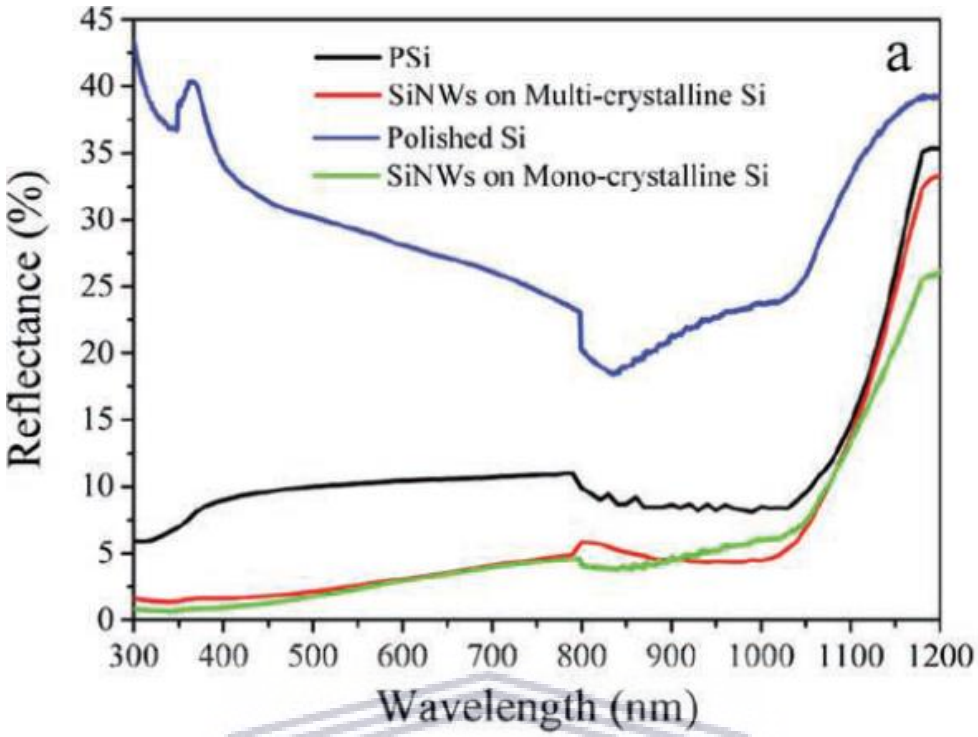

Figure 2.11: Reflectance measurement comparisons between c-Si wafer, porous-Si and Si NW arrays [2.56]

The experimental evidence shown in figure 2.11 presents Si NWs to be one of the most ideal candidate materials that can be used to enhance anti-reflective and light trapping properties in solar cells. This leads to a low optical reflection property of Si NWs as exhibited by Si NW arrays which reduce optical reflectance to below 1.4% over a wider range (300 – 600nm) of the solar spectrum as shown in figure 2.10.

These exceptional antireflection properties displayed by Si NWs can be attributed to the small diameter of Si NWs which is below the visible wavelength range and consequently lead to a sub-wavelength surface (SWS). This surface becomes antireflective supressing reflection over a wide range of wavelengths since the surface resembles a surface-relief grating with a period shorter than the wavelength of light [2.56]. Similarly, other Si nanostructured architectures such as nano cones/tapered NWs have been able to exhibit enhanced optical absorption and antireflective properties. These characteristics can be attributed to the gradual refractive index

transition from air into the NW which is a result of the diameter variation from the tip to the bottom of a NW hence the reflectance through most parts of the optical spectrum is attenuated [2.57-58].

The accurate determination of the enhancement of light trapping/absorption by Si NWs is a very intricate subject matter hence to date, there has been very limited literature on the accurate approach to understand the concept accurately. In an ideal setup, pristine Si NWs would be fabricated from a thin c-Si film that is grown on a transparent substrate such that there would be no parasitic absorption of incident light due to substrate contribution. Realizing such an experimental setup is a very challenging exercise however, Si NWs etched from a mc-Si thin film that was grown on a glass substrate have been successfully investigated by Sivakov et al. [2.59]. In their work, Sivakov et al. were able to demonstrate that Si NWs etched from a 2.5 – 3 µm mc-Si thin film exhibit zero transmission of light within the 300-500 nm range hence his work was a clear demonstration of enhanced light trapping from Si NWs.

Several approaches have been employed in commercial solar cells in order to improve their light trapping ability and these include surface modifications such as the texturization/roughening method which involves incorporation of pyramid-like structures to enhance absorption [2.60]. Texturization of the air-semiconductor interface results in random light propagation paths within the active layer which leads to higher total internal reflection and hence the higher absorption enhancement.

However, even after texturization, anti-reflective coatings are still necessary in commercial thin film solar cells in order to realize very low reflectance. This circumstance is a consequence of the fact that the texturization technique is limited by the Yablonovitch limit which states that, enhanced light absorption cannot surpass the $4n^2/\sin^2\theta$ factor whereby n is the refractive index of the active material and θ is the

angle of the emission cone [2.61]. The development of the Yablonovitch limit was solely based on the statistical ray optics perspective which models light as a straight line and has been extensively used to successfully to understand the optical phenomena [2.61].

Nevertheless, the proposed model (Yablonovitch limit) does not account for the electromagnetic wave aspect of light and fails in nanophotonic films with dimensions similar or less than the light wavelength since the assumptions made in the conventional theory do not hold. The employment of an advanced statistical coupled-mode theory with meticulous electromagnetic perspective has demonstrate the limitations of the Yablonovitch limit to only bulk structures [2.62]. Numerically, this model has been able to demonstrate absorption enhancements far beyond the conventional limit in the nanophotonic regime dependant on the design quality. Furthermore, the use of highly advanced wave concepts such as plasmonic material, dielectric waveguides, photonic crystal, sharp features, nanowire-based cells have also demonstrated that the Yablonovitch limit can be exceeded [2.63].

As recently indicated, nanowire-based structures such as Si NW arrays have been experimentally found to display exceptional optical properties with very minimal reflectance within the visible range without the aid of antireflective coatings. Several studies have been conducted to show the potential of Si NWs in enhancing optical absorption beyond the Yablonovitch limit. Yu et al. [2.62], observed that optimally designed Si NWs can achieve this exceptional property through the localization of the electromagnetic field. Similarly, Garnett et al. were able to obtain an optical path enhancement factor of about 73 which is almost three times the Yablonovitch limit ($2n^2 \sim 25$) from a well-ordered Si NW array without a back reflector [2.63].

Theoretically, the interaction of well-ordered Si NW arrays and electromagnetic waves have been extensively studied such that the effect of NW diameter, length and filling ratio on the optical absorption of Si NW arrays have been investigated. The results of Hu et al. on this work exhibited a high optical absorption enhancement at higher energies (> 2.8 eV) while showing no enhancement at lower energies (< 2 eV) [2.64] and they attributed this observation to the low extinction coefficient of Si being responsible for the low absorption from Si NWs. They then concluded that this shortfall could be rectified by using longer Si NWs with a back reflector. Furthermore, Li et al [2.65] also investigated the effect of periodicity of a perfectly ordered Si NW array on the light absorption properties of a Si NW array. From their work, it was concluded that optimal light absorption is realized when the periodicity of the array is in the same range as wavelength of the light, ranging from about 250 – 1200 nm and a diameter to periodicity ratio of 0.8. For smaller periodicity`s such as 100 nm, the wavelength of the light is much bigger than the geometrical dimensions of the NW array hence the light will penetrate through with very minimal scattering implying low absorption enhancement. If the geometric dimensions of the NW array are in the same order of magnitude with the light wavelength, light scattering and diffraction becomes apparent which then increases the optical path length and hence improve absorption of the light.

In contrast, other works conducted on the same subject of “light trapping in Si NWs” have presented contradicting views whereby, the periodicity of the Si NW array is found to be of negligible influence with respect to light trapping. Foldyna et al. [2.66-67], were able to demonstrate that the periodicity of a Si NW array has minimal effect on the light scattering capabilities. In their work, they concluded that the observed efficient light trapping observed is a result of efficient integration of the incident light and the internal waveguide resonance modes within each individual Si NW. This

means that each Si NW acts as a wave guide that confines and propagates incident light along their length hence invalidating the effect of periodicity of the array. Furthermore, it was observed that a NW array consisting of different NW diameters was more efficient in coupling light of different wavelengths hence the enhanced light trapping capabilities.

2.3.4 Enhanced electron transport properties

The electron transport properties of MACE Si NWs have not yet been extensively studied. However, considerable work that has been done shows a direct link between morphology, surface to volume ratio, starting-wafer dopant concentration and the electron transport characteristics of these nanostructures [2.68]. Qi et al. was able to demonstrate that a highly doped starting wafer also results in highly doped Si NWs with a larger surface roughness than when compared to lightly doped ones [2.69]. This roughness results in a larger surface-to-volume ratio and a thicker oxide layer which can act as an electron barrier. This shows the direct effect of the NW morphology on its electronic properties.

Similarly, the band gap of Si NWs can be linked to the NW diameter such that at small diameters approaching the Bohr radius, quantum confinement becomes prominent resulting in a widened band gap. The relationship between the bandgap and the Si NW diameter can be expressed using, the effective masse approximation – particle in a box (EMA-PIB) model as shown in eq. (2.4):

$$E_g = E_0 + \frac{C}{d^2} \qquad (2.4)$$

Whereby E_g denotes the Si NW bandgap, E_0 is the Si bandgap, C represents a constant and d is the Si NW diameter

Clearly, it is evident that Si NWs offer the ability to tune the band gap of grown structures via diameter control and this feature plays a crucial role in solar cells by

reducing heat losses. Furthermore, this dependence of the bandgap on the diameter and surface terminations of Si NWs has been studied theoretically and extensively by Nolan et al. [2.70]. Using density functional theory (DFT) calculations, they successfully demonstrated an increase in bandgap with decreasing Si NW diameter and further showed that for diameters less than 1 nm, Si NWs have a direct bandgap unlike bulk Si. Moreover, Sacconi et al. further showed that Si NWs of the same diameter but different surface terminations, exhibited different band gaps and this was evidence of the effect of surface termination on the band gap [2.71]. In support of this statement, H-terminated Si NWs exhibited a wider band gap when compared to the SiO_2 terminated NWs. Such a result was attributed to the less confinement from the SiO_2[2.71].

Generally, the electrical properties of Si NWs fabricated using the top-down approach are like those of the starting parent wafer. However, these properties may vary from the parent bulk Si wafer depending on the size and other surface treatments of the Si NWs. As a result of the high surface-to-volume ratio offered by Si NWs, surface properties have much greater influence on the overall electron transport properties. Surface treatment practices such as post annealing and passivation can result in excellent properties such as enhanced mobility of carriers within the Si NW [2.72].

2.4 Silicon Nanowire Based Solar Cells

In recent years, extensive research has been conducted in order to explore the potential of Si NWs in next generation PV technologies with high PCE and yet low production costs. Si NWs have been considered as ideal candidate materials due to their extraordinary structural, optical, electrical, thermal and mechanical properties [2.73-75]. These highlighted advantages of Si NWs may not necessarily lead to solar

cells with efficiencies higher than the known Shockley-Queisser limit for solar cell efficiency. However, the development of Si NW solar cells can help reduce the production cost of solar cells drastically as a result of reduction in material quantity, purity and quality needed.

As previously indicated, properties of Si NWs enable them to have superior advantages over planar solar cells such as enhanced photo-conversion efficiency, low reflectivity, ideal light-trapping, adjustable bandgap, enhanced charge separation due to architecture, less sensitive to defects on material and enhanced electron transport. Si NW solar cells are one out of a range of materials that can be used to make NW based solar cells such as zinc oxide, zinc sulphide, telluride, selenide, nitride, arsenide, gallium, titanium oxide and indium [2.76-79].

In Si NW based solar cells, there are 3 types of possible p-n junction architectures, and these include the:

- radial p-n junction
- axial p-n junction
- substrate p-n junction

These three (3) p-n junction architectures are designed such that they maximize the exceptional Si NW properties such as enhanced light absorption and antireflective ability. Furthermore, these p-n junctions enhance, exciton formation, charge separation and charge-carrier collection as summarised in figure 2.12.

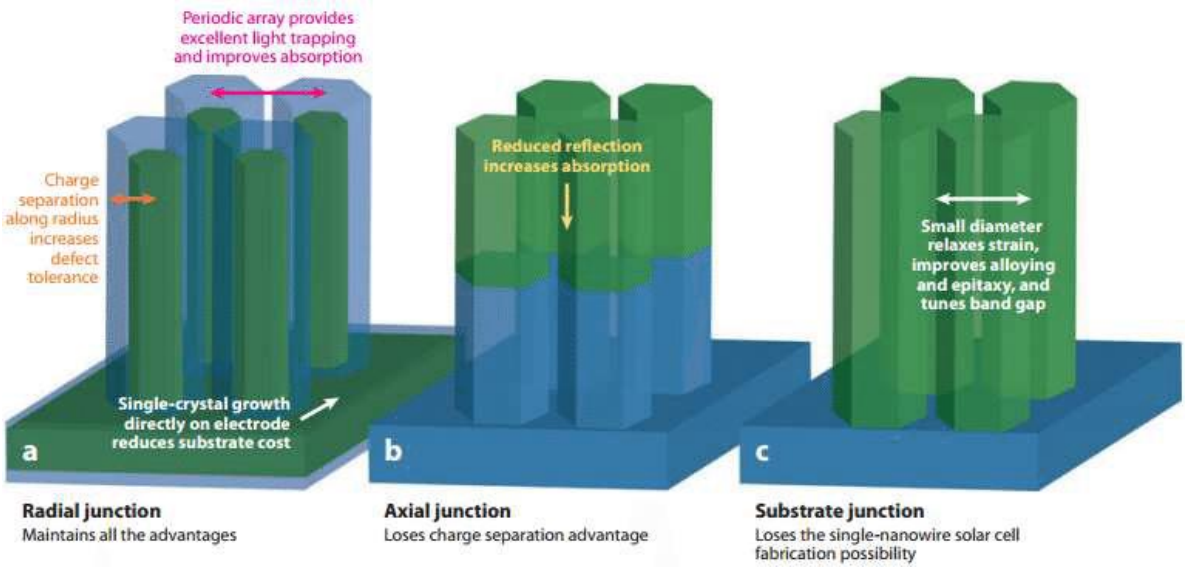

Figure 2.12: The different p-n junction architectures with their advantages and disadvantages [2.58].

From the schematic evidence presented in figure 2.12, it can be observed that only the radial p-n geometry can exhibit most of the Si NW advantages which include low reflectivity, excellent light trapping, enhanced radial charge separation, relaxed interfacial strain and the ability to be removed from substrate and have single NW solar cell. Clearly, the axial and substrate p-n junctions lose the radial charge separation capability and have a p-n junction like planar cells with a longer charge carrier collection distance [2.58]. The substrate junction geometry implies that each individual NW cannot be a solar cell without the substrate, hence they cannot be removed to be individual cells but can be removed for other NW applications.

2.4.1 Junction formation for NW solar cells

In order to have a functional NW solar cell, a junction must be created within the NW so that charge carriers can be separated and collected at different points. The junction can be created along the radial direction (radial separation), along the length (axis separation) and at the substrate and NW interface (substrate separation). The main role of the junction is to create a potential difference within the NW and force

electrons and holes to flow in opposite directions and be collected at the contacts as shown in figure 2.13. To form this junction, extrinsic or intrinsic dopants are introduced into a semiconducting material at different regions of the NW resulting in a chemical potential difference.

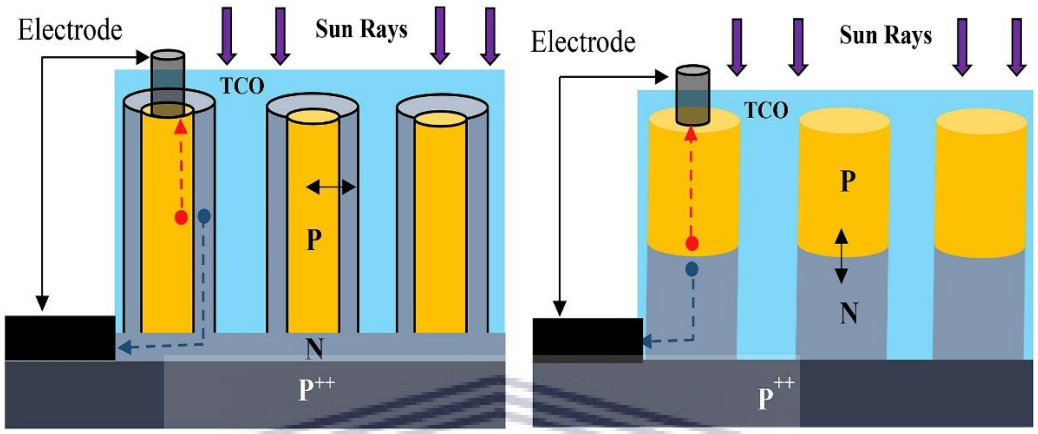

Figure 2.13: Radial and axial solar cells schematic [2.80]

In the case of MACE Si NWs, the introduction of dopants can be achieved using thermal diffusion method or through thin film deposition over the existing single semiconductor NW [2.81-82]. During thermal diffusion, the doping duration and temperature are crucial parameters to ensure that NWs do not become wholly doped resulting in formation of substrate junction which forfeits the radial or axial junction advantages [2.83,2.84]. The formation of a p-n junction using thin film deposition approach requires that the Si NW shell be of a different dopant carrier type to that of the core of the NW.

2.4.2 Contact electrodes

In a Si NW solar cell, the p-n junction is crucial for charge carrier separation. However, after the charger carriers have been separated, contact electrodes are necessary for the extraction of electrons and holes formed in the NW solar cell to an

external circuit. As in planar solar cells, ohmic contacts are necessary in NW solar cells too in order to enhance open-circuit voltage (V_{oc}), short-circuit current density (J_{sc}), the fill-factor (*FF*) and the power conversion efficiency PCE. The fabrication process of these ohmic contacts in NW solar cells is like that of planar solar cells which involves heavy doping and interfacial layers [2.63,2.85,2.86].

There are several methods that can be used to fabricate contacts for single-nanowire solar cells such as e-beam, photolithography and metal evaporation. In complex architectures such as the radial junction solar cell, several lithographic and etching steps are necessary to ensure that the electrons and holes are extracted separately [2.82,2.87]. In the case of a Si NW array setup, contacts can be made like those of planar solar cells and ensuring that the top contact is transparent to enable light penetration into the active material while the bottom contact uses a reflective metal contact. In high aspect-ratio structures such as Si NW solar cells, the realization of uniform continuous and conductive coatings is a big challenge and requires the use of sophisticated deposition techniques like sputtering or electrodeposition [2.63]. During contact deposition, the NW diameters can expand such that they contact each other making the conductive layer more effective [2.88].

2.4.3 Single nanowire p-n junction solar cell

As indicated previously, a NW solar can be made up of a single NW or an array of NWs dependant on the junction geometry (subsection 2.4.1). In single NW devices, fundamental phenomena such charge transfer, surface recombination and the diffusion of minority carriers can be carefully investigated and understood. Furthermore, a single NW device eliminates the influence of averaging effects when investigating other properties such as dopant density, surface states and conductivity of the device. However, single NW devices can therefore not be used to understand

phenomena such as light trapping or absorption since those depend on the array and the results are a collective contribution of a group of NWs.

In as much as single NW devices are useful in studying properties like carrier transport, dopant level, surface states and charge separation, it is useful to understand that extracting this information is a complex process. Unlike in bulk wafer or planar devices, techniques such as hall-effect measurements, X-ray photoelectron spectroscopy (XPS), Auger electron spectroscopy (AES) and secondary ion mass spectroscopy (SIMS) cannot be used at a resolution necessary to produce accurate results [2.75]. This necessitates the use of traditional transport measurement techniques such as the back-gated or top-gated field effect transistor method which is commonly used for carrier concentration and mobility in thin films.

Using capacitance-voltage (C-V) measurements, Garnet et al. [2.85] was able to extract radial carrier concentration profiles and surface state density data from individual Si NWs. His results corresponded very well with diffusion simulation models, planar control samples and other surface state density values found in literature. However, one drawback from the C-V measurements was that from the radial carrier concentration data, dopant distribution could not be directly deduced [2.75].

2.4.4 Heterojunction and homojunction Si NW solar cells

The fabrication of a heterojunction solar cell can be realised combining Si NWs with another inorganic material in order to enhance the overall performance of the solar cell [2.89-91]. The use of high aspect ratio Si NWs in solar cells ensures an increased surface area which however introduces more surface defect states, hence an increased recombination rate. The surface recombination in Si NWs can be controlled by the correct passivation of the Si NWs and this can be achieved by depositing a thin layer of a-Si:H to coat the Si NWs [2.92] as shown in figure 2.14.

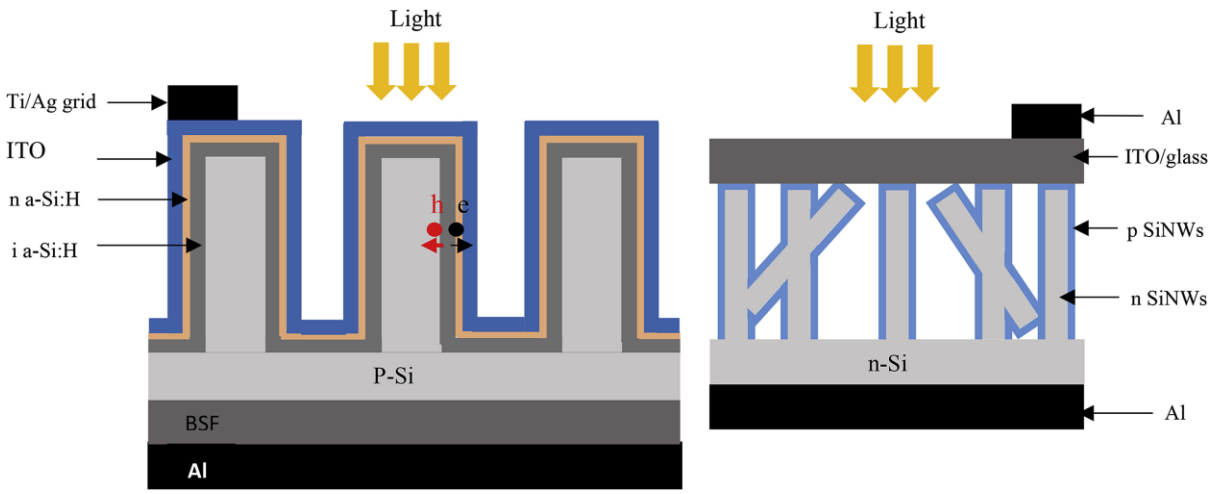

Figure 2.14: Schematics of a Heterojunction and Homojunction NW solar cells [2.80].

The cross-section schematic of a heterojunction and homojunction shown in figure 2.14 shows the difference between the two which lies in how the inorganic material is incorporated in the Si NW solar cell. In comparison, Dong et al. showed that high aspect Si NWs yielded a 16.02% and 14.05% efficiency in a heterojunction and homojunction solar cell respectively [2.93]. In other work, Khan et al. reported on Si NW solar cells with a buried contact (Si NW-BC) whereby the BC ensures that there are minimal losses due to contact resistance in Si NW solar cells [2.94]. It was observed that the BC arrangement results in lower series resistance due to the larger surface area of metal contact and also has a higher shunt resistance due to no contact between Si NWs and front metal contact leading to enhanced V_{oc}, *FF* and the PCE [2.94].

2.4.5 Heterojunction hybrid Organic/Si NW solar cells

Hybrid solar cells are realized through combining organic and inorganic materials whereby, the inorganic material ensures charge carrier transport, high mobility, solution processability, environmental stability, and also act as an electron acceptor for PV applications [2.95-97]. The organic material is commonly used as an absorber

and electron donor in the solar cell [2.98]. The main aim of hybrid solar cells is to combine the unique advantages of both organic and inorganic species such as, light weight, low fabrication cost, low processing temperatures and flexibility from the organic material [2.50]. As a result, a considerable amount of effort has been directed towards the implementation of hybrid systems in photovoltaics in a cost-effective way that also provides mechanical flexibility.

Cheng et al. [2.99] fabricated an organic/inorganic heterojunction structure using p-type poly(9,9-diethylfluorene)/n-Si NWs which exhibited good photovoltaic properties and photosensitivity when illuminated with visible light. This result paved the way for researchers to extensively explore optimum organic/inorganic junctions for efficient charge carrier separation and carrier collection for enhanced power conversion efficiency of hybrid solar cells. In other works, it has been demonstrated that morphology and surface termination of Si NWs are crucial factors in enhancing PCE of a solar cell since they increase interfacial area, exciton separation and enhance the stability of solar cells under atmospheric conditions [2.100-102]. In the case of an array of MACE-Si NWs, one of the main challenges is filling up the interspaces between the dense NWs with conductive conjugated molecules, such as poly(3,4-ethylene dioxythiophene):poly-(styrenesulfonate) (PEDOT:PSS) and poly-(3-hexylthiophene) (P3HT).

Shiu et al. successfully fabricated a polymer/Si NW hybrid solar cell with a heterojunction efficient in charge carrier separation and collection. This arrangement was achieved by coating the Si NWs with PEDOT:PSS which has a highest occupied molecular orbital (HOMO) energy (~5.1 eV) that matches the valence band energy of Si hence the superior carrier separation and collection [2.103]. Furthermore, the enhanced performance of these hybrid solar cells was attributed to the shorter carrier

diffusion path, the low R_s and a larger junction surface area offered by core-shell structures.

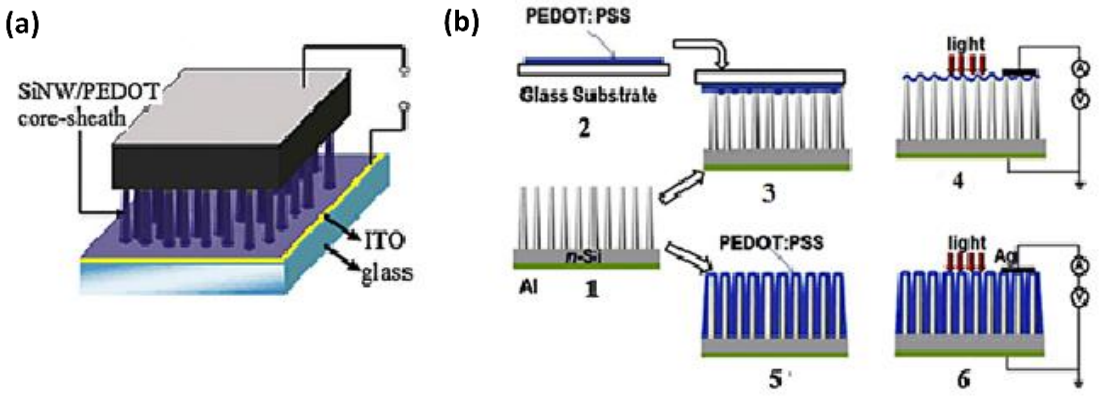

Figure 2.15: Schematic showing (a) the Si NW/PEDOT/ITO heterojunction SC and (b) fabrication process of Si NW/PEDOT:PSS hybrid SC [2.50].

During the incorporation of PEDOT:PSS in Si NW arrays, complete coverage of the Si NWs with the conductive polymer is essential to ensure efficient charge carrier extraction. Shen et al. opted to use a thin layer of spiro-OMeTAD, a smaller conjugated polymer as a substitute for the bulkier PEDOT:PSS in order to ensure complete coverage of the Si NW array [2.104]. The addition of this thin layer was found to drastically reduce charge carrier recombination even though some remnant pinhole regions on the surface could result in charge leakage. However, an additional thin layer of copper (~2 nm) and PEDOT:PSS on the hybrid structure was found to further enhance the charge collection efficiency at the contact leading to a PCE of about 9.70%. On the same subject, Zhang et al. successfully fabricated a Si NW based hybrid solar cell by using P3HT, another bulkier polymer which encountered the NW array penetration challenge [2.105]. To address this problem, the Si NW array was dipped in a PCl_5 solution to reduce the density of the Si NWs and allow complete coating of the NWs by the larger P3HT molecules. In their work, they observed that an

optimal thickness of about 10 nm of the P3HT layer was crucial in obtaining an enhanced PCE of 9.2%.

In other work, Moiz et al. [2.106] succesfully fabricated a unique Si NW/organic hybrid solar cell whereby a conductive PEDOT:PSS layer is stamped on top of the Si NW array as shown in figure 2.15(b). The stamped geometry enhances the solar cell performance in various ways such as enhanced charge carrier transport, reduction in recombination losses, enhanced optical anti-reflectivity and lowered exciton decay. Furthermore, they observed that a thin layer of a few nanometres is crucial in ensuring efficient carrier transport while minimizing interfacial carrier recombination due to the small contact surface area between NW tip and PEDOT:PSS layer. As a result, this leads to enhancement in open circuit and short circuit current over that of bulk hybrid solar cells.

Over the past decade, various organic/Si NW hybrid architectures for solar cell applications have been investigated. As indicated previously, in most cases, the inorganic (Si NWs) counterpart is maintained due to their unique and advantageous properties while the organic species are variated for optimal performance. Chehata et al. [2.98] used poly[2-methoxy-5-(2-ethylhexyloxy)-1-4-phenylenevinylene] (MEH-PPV) as a donor while the Si NWs were used as absorbers and charge carrier transport to fabricate a MEH-PPV: Si NWs hybrid solar cell. In this geometry, the role of Si NWs with their high interfacial surface area is to ensure efficient electron separation from MEH-PPV and consequently reduce recombination while promoting the charge transfer process [2.98]. However, the intrinsic surface defects in Si NWs have been proven to be detrimental to the efficiency of such novel structures, through recombination that occurs in the surface trap states. Chehata et al. [2.107] showed in their work that such shortfalls can be rectified through surface modifications using

different functional organic molecules such as polystyrene which leads to PS functionalized Si NWs (PS-Si NWs). The additional organic layer of PS results in a new homogeneous organic/organic/Si NW interface and modified band structure as shown in figure 2.16 [2.107].

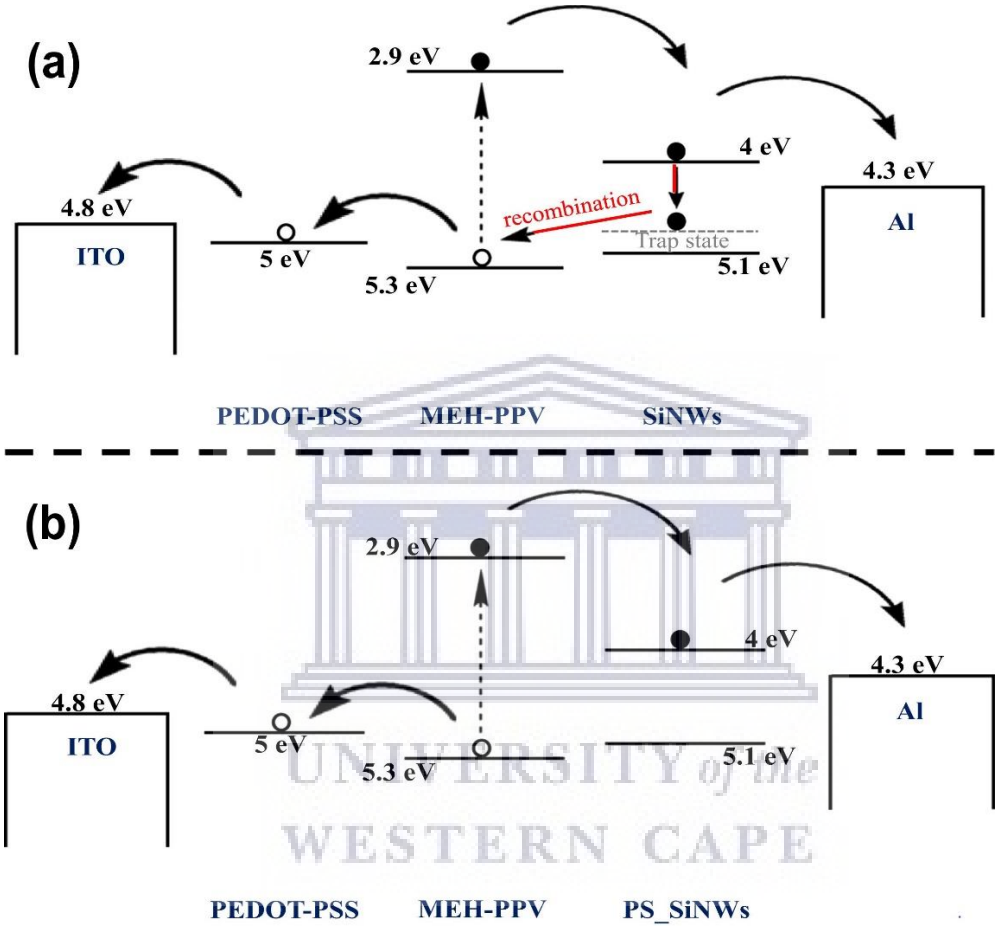

Figure 2.16: Energy level schematic diagrams of hybrid solar cells with (a) as-synthesised Si NWs, (b) PS functionalized Si NWs (PS-Si NWs) [2.98].

The presence of surface trap states in high aspect ratio nanostructured materials like Si NWs has been found to have a negative impact in the overall performance of such materials leading to poor PCE in hybrid solar cells. This can be attributed to the fact that the energy of these trap states can be found within the band gap of Si NWs as depicted in figure 2.16(a). This implies that, some of the electrons form the MEH-PPV donor can be effectively trapped in these sites leading to high R_s for carrier

transport. The existence of an energy barrier between the Si NW trap states and the Al electrode leads to a higher probability of recombination of trapped electrons and holes in the HOMO level of MEH-PPV resulting in low R_{sh}. Figure 2.16 (b) shows that the addition of a PS layer to functionalize the Si NWs ensures an efficient population degeneration of such trap states [2.108]. This leads to a decreased recombination and a low R_s which then leads to a higher J_{sc} and fill-factor. Furthermore, the R_{sh} and V_{oc} become enhanced due to the reduced recombination leading to an enhanced PCE of the hybrid solar cell.

2.5 Organic Semiconductors

Organic materials comprise of organic molecules as building blocks which are fundamentally carbon backbones, hydrogen and other functional groups made up of oxygen, nitrogen, and sulphur. In organic semiconductors, the molecules are π-conjugated in such a way that, the backbone consists of single (σ) and double (σ+π) bonds alternating between carbon atoms.

In an organic molecule, each carbon atom has at least one single and one double bond with its neighbouring atoms hence a molecule can have two equivalent configurations [2.109]. In some cases, this alternating pattern of single and double bonds is broken and leads to defects whereby a carbon atom has single bonds with both of its neighbouring atoms . This occurrence results in the carbon atom having an unpaired, unstable electron that is highly reactive and its removal during oxidation leaves a positively charged carbon atom (carbocation) in the molecule. In contrast, another electron can be brought by to stabilize the lone electron through a reduction reaction which then results in a carbanion (negatively charged carbon atom). These charged defect sites can move along the molecule backbone carrying current and this

leads to conductive organic semiconductors. These carbocations and carbanions are analogous to holes and electrons in inorganic semiconductors respectively [2.109].

In an organic molecule, the carbocation and carbanion creation lead to modifications in the molecular bonding pattern since the length of single and double bonds are different. This distortion of the molecule can induce the coupling of electronic states and atomic positions which then determines the fundamental characteristics of organic semiconductors. The bonding between a carbocation and carbanion pair (exciton) is driven by an electrostatic interaction which further ensures the localization of the pair to reduce distortion of the molecule bonding pattern. The binding energy of these "organic excitons" ranges between $0.1 < E_b < 1$ eV which is much higher than that of "inorganic excitons" that have $E_b < 25$ meV. This characteristic has led to the extensive development of organic light emitting diodes (OLED) since there is a higher chance of radiative exciton recombination under such spatial confinement [2.109]. However, this characteristic of organic semiconductors is a major drawback for solar PV applications.

The energy band structure of organic semiconductors is a result of hybridization of atomic orbitals into molecular orbitals such that the filled π (bonding) and the empty π* (anti-bonding) states are separated by an energy gap. When more atoms or molecules are brought together, the number of the discrete energy levels increases and the gap between them becomes smaller resulting in a continuous energy band as shown in figure 2.17 [2.110].

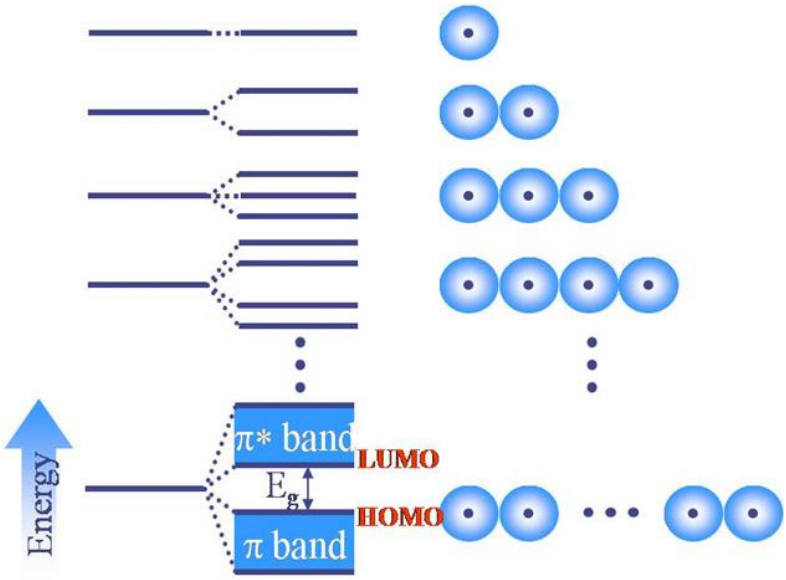

Figure 2.17: Energy band schematic for organic materials as the number of atoms increase to form the HOMO and LUMO energy levels [2.110].

After the formation of the energy band, the highest filled state (π) is known as the highest occupied molecular orbital (HOMO) while the lowest empty state (π*) is known as the lowest unoccupied molecular orbital (LUMO) as shown in figure 2.17. The HOMO and the LUMO levels are analogous to the valence band edge E_v and the conduction band edge E_c of inorganic semiconductors respectively. The energy gap (band gap) between the HOMO and the LUMO is unique and specific to that molecular configuration. Typically, for most polymers (inorganic semiconductors) the band gap ranges between 1.5 to 3 eV [2.111] and can decrease as the number of molecules is increased. As indicated earlier, the analogy between HOMO/LUMO and valence/conduction band is a convenient way of understanding them, however the HOMO and LUMO levels are specific to molecular configuration and not the whole material. This observation implies that, since a molecule has a definite number of atoms, the π and π* bands have no continuum states. Furthermore, optical properties

of the organic material which are dependent on band structure can be influenced by intermolecular interactions such as solution vs thin film form [2.109].

The main advantage of organic materials is the ability to be synthesized over a wide range of molecular configurations resulting in different optical properties that can be tailored for each specific application. On the contrary, the wide range of possible molecular configurations can lead to inconsistencies and lack of definite conclusions when real device applications are concerned.

2.5.1 P3HT and PCBM polymer blend

Regio-regular Poly(3-hexylthiophene) also known as rr-P3HT, is one of the commonly used and extensively investigated conjugated polymer for solar PV applications. Structurally, P3HT consists of a thiophene ring which is made up of four conjugated carbon atoms with one sulphur atom and has a hexyl chain (C_6H_{13}) [2.110].

The main role of alkly (hexyl) sidechains in polythiophenes is to ensure solubility of the thiophenes in organic solvents while the thiophene backbone is responsible for the optical properties and the one-dimensional transport properties of the polymer chain. However, the overall organic material (thin film) properties such as the absorption spectrum and charge carrier mobility have been found to be more dependent on the actual arrangement of the polymer chains relative to each other and the substrate [2.102]. Furthermore, two-dimensional transport properties rely on this relative arrangement of poly chains to ensure charge transfer from one chain to the next. Optimum spacing and parallel arrangement of the thiophene rings from different chains is also crucial in ensuring the overlapping of π orbitals which are responsible for charge transfer [2.112]. This optimized arrangement is referred to as π-stacking.

During π stacking, the positioning of the alkyl side chains on the thiophene ring is very important such that its regularity has a direct influence on the properties of polythiophenes. Regio-regular P3HT has been found to mostly result in crystalline thin films while regio-random P3HT results in amorphous films with different bandgaps of about 1.7 eV and 2.1 eV respectively [2.113]. This has rendered regio-regular P3HT as the most idea candidate owing to the superior optical absorption and charge carrier transport properties of crystalline organic thin films [2.114]. A schematic representation of a highly regio-regular P3HT structure is shown in figure 2.18(a) and it is worth noting that synthesis of such high quality rr-P3HT is very challenging hence it is expensive.

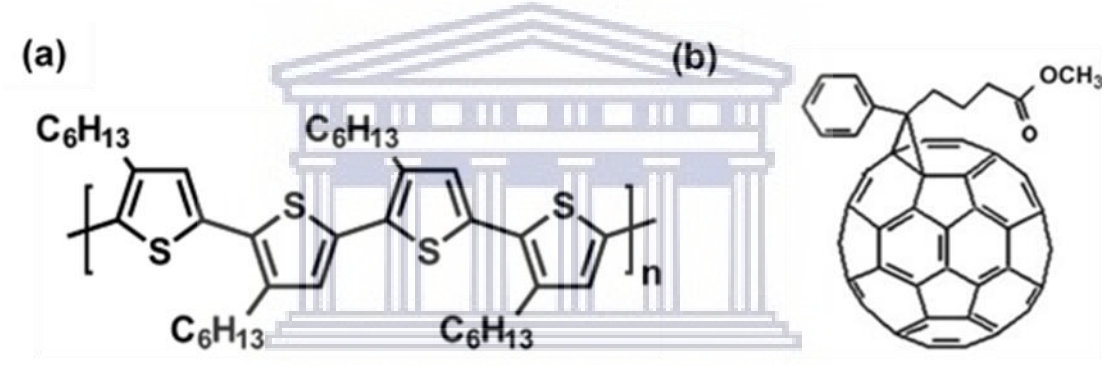

Figure 2.18: Schematics of (a) Regio-regular P3HT and (b) PCBM molecular structures [2.113].

During synthesis of regio-regular P3HT, longer chains and well crystallized thin films are the most ideal for solar PV applications. However, there are several other factors that can affect other P3HT properties like mobility, and these include: molecular weight [2.115], substrate, solvent [2.116], deposition technique [2.117] and post deposition treatments [2.118]. Under optimal conditions, the highest mobility observed from P3HT have been 0.1 cm^2/ V.s for holes and 10^{-4} cm^2/ V.s [2.119].

Figure 2.18 (b) shows the molecular structure of phenyl-C61-butyric acid methyl ester, commonly known as PCBM. PCBM is a fullerene derivative that first realized in 1995 by Hummelen et al. [2.120] and is commonly used in organic solar PV as an

electron acceptor material. The structure of a PCBM molecule consists of a fullerene Buckyball with a functional group attached to it which allows it to be soluble in several solvents such as chlorobenzene [2.121], dichlorobenzene [2.122], chloroform [2.123], toluene [2.124] etc. The UV-Vis absorption peak of PCBM is found at shorter wavelengths below 400 nm and it is for this reason that PCBM cannot be used as a light absorbing material in solar PV applications. However, the positioning of the HOMO and LUMO level range from 3.7 to 3.8 eV and 5.5 to 5.9 eV respectively, has been found to very ideal for exciton dissociation at the P3HT/PCBM interface [2.125-127]

The P3HT:PCBM blend has been one of the commonly used organic blends for the synthesis of active layers in bulk heterojunction organic solar cells. The choice of these materials is highly influenced by their high solubility in most solvents resulting in easier spin coating or doctor blading for thin film fabrication. In an organic solar cell, the performance can be influenced by factors such as type of solvent, the blend ratio, morphology, and thickness of the active layer. In other works, P3HT:PCBM bulk heterojunction solar cells have been found to exhibit PCE`s of about 5% on average [2.124].

2.5.2 PEDOT:PSS

Poly(3,4-ethylenedioxythiophene): poly(styrenesulfonate) also known as PEDOT:PSS is a transparent conductive polymer used as a hole transporting for the anode in solar cell application [2.121,2.121,2.126]. As indicated, this polymer is made up of two parts being PEDOT and PSS. PEDOT is a conjugated polymer made up of polythiophenes and used for hole transportation while PSS consists of sulfonated polystyrene and sulfonyl for electron transport. Figure 2.19 shows the molecular structure of PEDOT:PSS

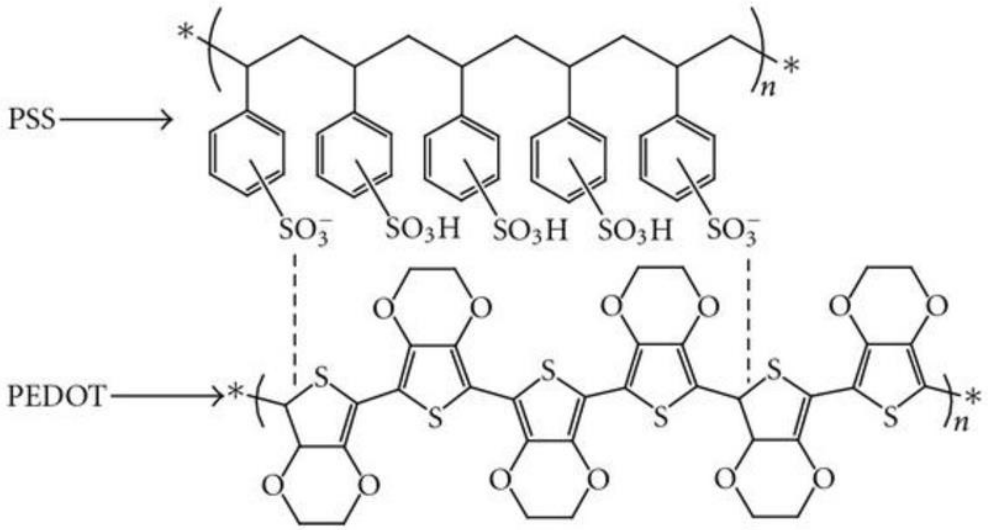

Figure 2.19: The molecular structure of PEDOT:PSS [2.121].

As shown in figure 2.19, the PSS part is a surfactant that enables dispersion and solubility of PEDOT in water and other solvents. Commercially, PEDOT:PSS is available as a dark-blue opaque solution that can form smooth continuous thin films on substrates through different solution deposition techniques such as spin coating and many more. Depending on the deposition technique used, PEDOT forms smooth thin films with roughness below 5 nm and is almost transparent with transmittance (T) of about 90% within the visible range (~550nm).

In as much as PEDOT:PSS has been found to exhibit superior conductivity and high work function, these properties are dependent on additive addition and post deposition treatment. The conductivity of PEDOT:PSS is spread over a wide range from about 10^{-2} to 10^{3} S.cm^{-1} while the work function ranges between 5.0 to 5.2 eV and these properties can lead to spontaneous charge transfer with fast kinetics which is typical of catalytic behaviour [2.127]. Furthermore, PEDOT:PSS has been found to exhibit great photo and electrical stability even when exposed to air. These superior properties have led to the wide application of PEDOT even without the PSS part, in

energy conversion and storage field. These applications include dye-sensitized solar cells, organic solar cells, supercapacitors, fuel cells and thermoelectric devices [2.127].

2.5.3 Organic solar cells

Organic solar cells (OSC`s) can be classified as photovoltaic devices that are made of organic materials such that semiconducting polymers form an integral part of their construction. The active layer of a conventional organic solar cell consists of a conjugated polymer which acts as an electron donor and hole transporter while a fullerene material becomes the electron acceptor material which transports electrons to external electrodes for extraction hence the PV effect.

One of the major and notable contributions in organic PV`s was that of charge separation in polymer/fullerene systems by Saricifitci et al. [2.128], where they displayed ultra-fast electron transfer at a donor/acceptor (D/A) interface. This discovery of the 300 femtoseconds (fs) electron transfer time against a picosecond decay time in a polymer, marked the beginning of organic PV`s. In other work, Aemouts et al. [2.129] were able to demonstrate rapid exciton dissociation using C_{60} derivatives such as PCBM when blended with a polymer whereby he obtained a PCE above 3%. Initially, the donor (polymer) of choice was mostly M-PPV combined with $PC_{60}BM$ but with more developments, P3HT became the substitute for M-PPC since the P3HT/PCBM blend became more efficient and easier to process [2.130]. Further developments in the field have led to even newer efficient combinations like PCPDTBT/$PC_{71}BM$ [2.131].

Despite their lower efficiencies when compared to their inorganic counterparts, OSC`s have displayed numerous novel features making them feasible competitors to

inorganic cells. These features include low-cost processing, their light weight and flexibility which makes the use of flexible substrates possible.

2.5.4 Organic photovoltaic device operation mechanism

The operation mechanism of organic PV devices can be classified into five categories: (i) Photon absorption (ii) Exciton formation and diffusion (iii) Exciton dissociation (iv) Charge transport and (v) Charge collection. Figure 2.20shows a schematic representation involved during current generation in an organic solar cell.

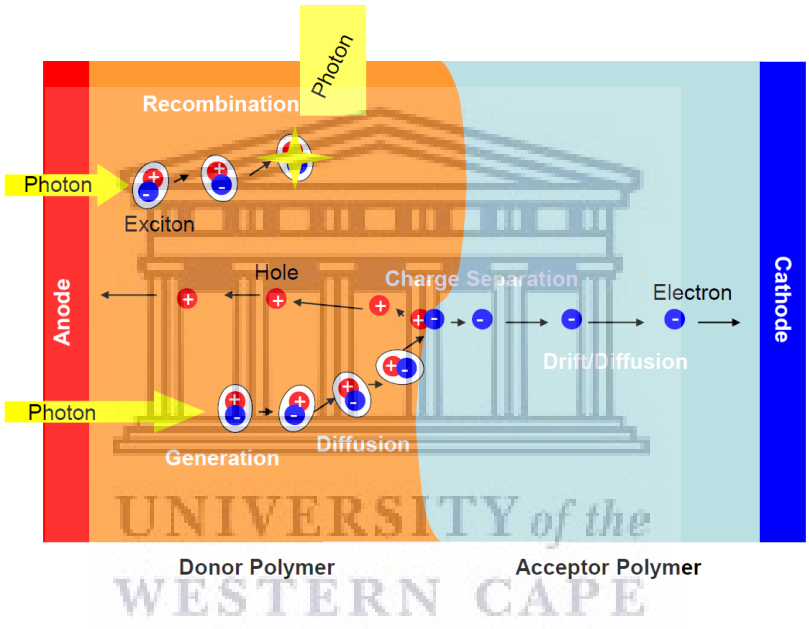

Figure 2.20: Schematic showing the principle of operation of an organic solar cell [2.132].

(i) *Photon absorption*: Upon illumination, the incident photons pass through several interfaces before reaching the active layer of the OSC. The active layer absorbs those photons whose energies are at least within the absorption spectrum of that active layer. Ideally, the band gap of the active layer should be small enough such that it can absorb the maximum range of the solar spectrum, e.g. c-Si with a band gap of 1.12 eV is theoretically capable of absorbing 90% of the solar spectrum while P3HT with its band gap of ~1.88 eV absorbs about ~46% of the solar spectrum [2.132].

(ii) *Exciton formation and diffusion*: the absorption of the photon results in the formation of an exciton which then diffuses within the active layer before it dissociates or recombine (decay). The material characteristics such as structure and dielectric properties determine the exciton lifetime and the diffusion length (LD) which is typically in the range of 5 – 10 nm [2.133]. The generated excitons have a finite lifetime, after which they recombine or dissociate into holes and electrons. The diffusion length becomes a limitation to the active layer thickness since bulk thickness greater than diffusion length will result in exciton decay and low quantum efficiency of the OSC.

(iii) *Exciton dissociation*: This process occurs at the D/A interface as a result of different electron affinities between the donor and acceptor. At the interface, the electron is acquired by the acceptor material which has a higher affinity for electrons while the hole remains in the donor material. After dissociation, the electrons jump to the LUMO level of the acceptor, while holes settle in the HOMO of the donor as shown in figure 2.20. The energy difference between the LUMO and HOMO of the acceptor and donor respectively, is indicative of the maximum open circuit voltage of the OSC.

(iv) *Charge transport*: The free charge carriers emanating from the dissociation process, no can move within the active layer towards electrodes for collection. In organic materials, the movement of free charge carriers depends on the structural ordering of the molecules and overlapping of π-orbitals to encourage charge mobility. Weak bonds and high disorder among molecules are part of the main causes of low mobility of charge carriers in OSC`s than their crystalline counterparts. Post-deposition treatment of OSC`s such as thermal annealing has been found to improve ordering of BHJ devices hence an improvement in PCE of the OSC`s.

(v) *Charge collection*: The free charge carriers that can move and reach the electrodes, are the extracted to the external circuit. The efficiency of the charge collection process is influenced by factors like the energy level mismatch at polymer/metal interface, interfacial defects etc. Interfacial modifications like the addition of intermediate layers like LiF and PEDOT:PSS has been found to enhance the performance of OSC`s [2.134]. Figure 2.21 showing the photon absorption and charge transport process within a P3HT:PCBM organic solar cell.

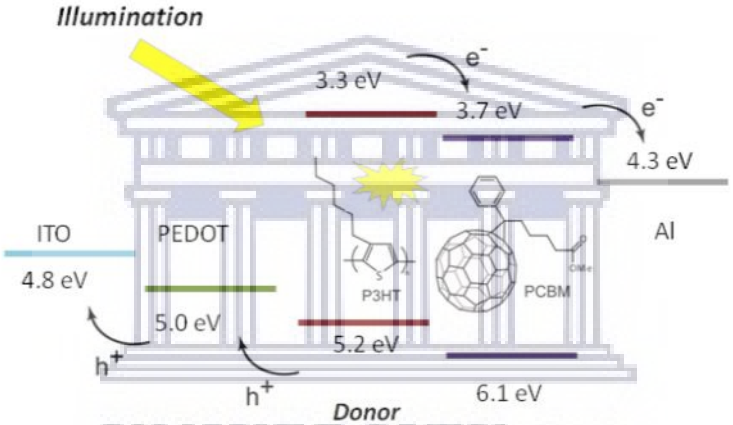

Figure 2.21: a schematic of absorption and charge transport mechanism in organic solar cells [2.134].

2.5.5 Exciton recombination in organic solar cells

In an OSC, the process of exciton formation is followed by diffusion of these excitons within the active layer. As the excitons diffuse towards the D/A interface, the bound charges can either overcome their coulombic interaction and be dissociated as charge carriers or they can decay and recombine with an opposite charge carrier and settle at the ground state. The recombination of charge carriers can either be geminate or non-germinate. The recombination of a pair of charge carriers from the same

exciton is termed as germinate recombination and this process is independent of excitation density and exciton concentration (monomolecular decay). If the recombination of charge carriers occurs between multiple charges from different exciton pairs, then it is non-geminate recombination and it is strongly influenced by the excitation density. The non-geminate recombination reaction can be a bimolecular reaction at a non-dispersive rate if there are no trap sites to influence recombination.

In cases where trap sites are present, the non-geminate recombination does not exhibit bimolecular reaction behaviour. This can be attributed to the non-dispersive recombination rate caused by the disordered and random relaxation of charged carriers in the trap sites [2.135]. The presence of trap sites in a material, results in a disordered potential landscape and this disorder leads to a power-law recombination rate which is linked to dispersive recombination kinematics [2.136].

2.6 Organic Solar Cell Architectures

2.6.1 Single layer structure

A single layer OSC structure consists of a single layer of photosensitive organic material sandwiched between two electrodes such that: transparent electrode/organic semiconductor/electrode as shown in figure 2.22 (a). This setup was demonstrated by Marks et al., whereby they sandwiched a 50 – 320nm PPV layer in-between ITO and a low work function cathode resulting in a low quantum efficiency of 0.1% at low intensity below 0.1 mW/cm^2 intensity [2.137].

This low quantum efficiency exhibited by the single layer OSC was attributed to the low mobility values in organic semiconductors. In comparison, organic semiconductors still lag from their inorganic counterparts with 10^{-3} cm^2/V.s compared to 10^3 cm^2/V.s order of magnitude for inorganic semiconductors. The low mobility

values organic solar cells are detrimental to the overall solar cell performance since they increase the probability of recombination within the SC and longer drift durations for those free charge carriers to be collected at electrodes. In single layer OSC`s, exciton formation can affect the PCE of the SC since, the excitons generated are tightly bound dipole charges which can only be dissociated at the cathode interface in order to become free charge carriers. This challenge led to further developments which resulted in structures with more efficient exciton dissociation and free charge carrier generation.

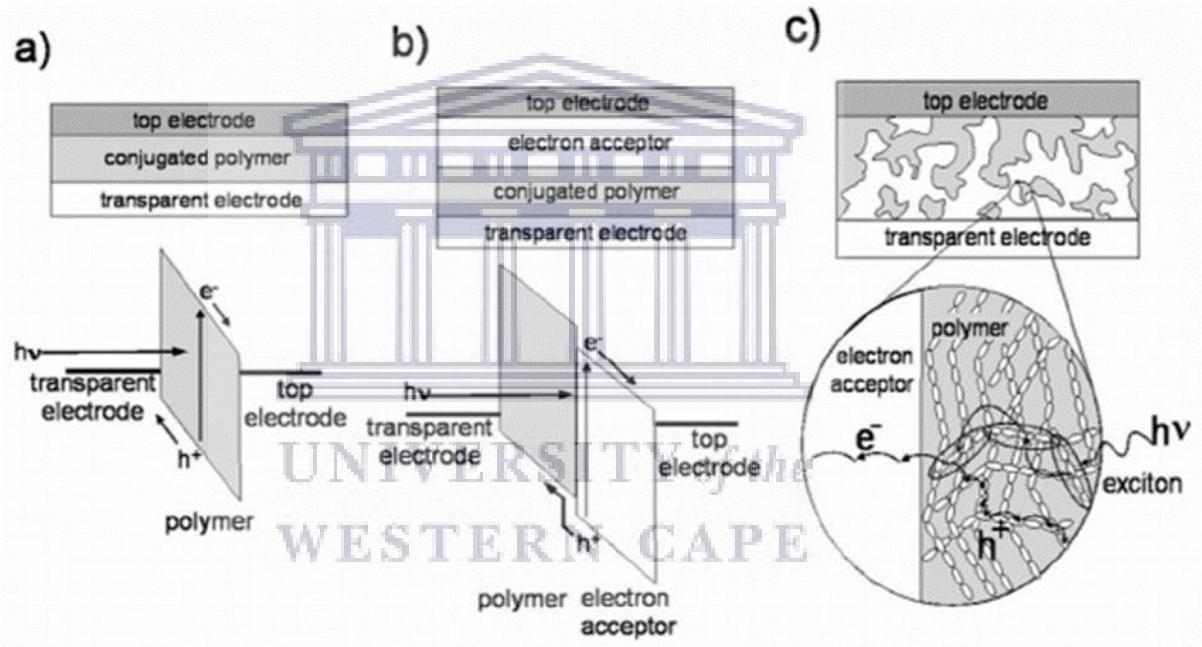

Figure 2.22: Different organic solar cell structures (a) single layer, (b) bi-layer and (c) bulk-heterojunction structure [2.137].

2.6.2 Bi – layer structure

The development of a donor – acceptor heterojunction (HJ) marked a significant improvement in the PCE of organic solar cells [2.138]. In a heterojunction, two materials of different electron affinities and ionization potentials are brought together at a junction such that an electric field can be created across the interface as displayed in figure 2.22 (b). The role of the electric field at the interface is to facilitate exciton

dissociation such that; electrons get accepted into the material with higher affinity for electrons while the remain in the material with a lower ionization potential.

This process can only occur if the difference in ionization potential of the two materials is greater than the binding energy of the exciton. This setup ensures that the planar HJ remains more efficient in free charge carrier generation than the metal-organic interface observed in single layer OSC`s. However, due to the exciton diffusion length, only those excitons generated within a range of about 10 – 20 nm from the interface can be able to reach the interface for dissociation. This occurrence leads to the loss of photons and excitons generated far from the interface which results in lower quantum efficiencies [2.139] and this limits the PCE of a bi-layered structure since the excitons must be dissociated within the 10-20 nm range. The whole processes involved in the photon conversion to current is well articulated in subsection 2.5.4.

2.6.3 Bulk heterojunction structure

The main challenge faced by the bi-layer OSC structure is the inefficient dissociation of generated excitons as a result of the interface position with respect to the position of the excitons. Figure 2.22 (c) shows the concept of a bulk-heterojunction (BHJ) structure which addresses this challenge through an intermixed donor-acceptor (D/A)interface with a larger surface area. The introduction of the BHJ concept by Yu et al. [2.139-140], marked a milestone in the history of OSC`s and has continued to be the core of current solar cell technology. In his work, he observed significant quenching of the photoluminescence and electroluminescence when the polymer donors and acceptor material were intermixed to form a phase-separated polymer composite. His observation was indicative of efficient and fast dissociation of excitons into free electrons in the acceptor and holes in the donor material.

A BHJ can be classified as a D/A blend in a bulk volume with a phase separation in about 1-20 nm length scale and this drastically increases the D/A interface area leading to an improved PCE. As shown in figure 2.22(c), the phase separation length is comparable to the exciton diffusion length which drastically minimizes recombination chances before reaching the nearby interface for dissociation into free charge carriers. This setup ensures that exciton generation and dissociation occur at almost every part of the active layer efficiently. This results in highly enhanced PCE of the organic solar cells subject to the availability of efficient pathways for the free charge carriers at the electrodes for collection.

2.7 Stability of Organic Solar Cells

In recent years, giant strides have been made with respect to the improvement of the PCE of OSC`s. This growth has been a result of extensive research and employment of novel strategies such as the design of highly efficient D/A materials, using ternary and tandem structures resulting in high PCE of about 16 % [2.141,2.142]. However, the relatively low stability of OSC`s has been one of the main bottlenecks that have held back the full commercialization of organic PV technologies to compete with their inorganic counterparts [2.143]. The main cause of the low stability in OSC`s can be attributed to the degradation they experience due to several different factors and this leads to a drastic drop in PCE [2.144]. Long-term stability of OSC`s remains a big challenge and this has attracted huge research interests in recent years [2.145].

In recent years, the degradation mechanism in OSC`s has been extensively studied to understand and develop novel strategies to enhance their stability. The development of new, non-fullerene acceptor materials has seen a great improvement of OSC stability with lifetimes predicted to be about 10 years [2.146]. In real-life operational conditions, there are several factors that influence the degradation and

stability such as inherent stability, irradiation-light instability, thermal instability, air instability and mechanical-stress instability [2.145].

2.7.1 Inherent instability

In OSC`s, a form of built-in instability can be observed even without the presence of external degradation factors. The two known main causes of this kind of instability are natural morphological changes that occur in the active layer and the diffusion of carrier layer and electrode material into the active layer. In a BHJ OSC, the active layer is the most critical and complex nanostructured layer with mixed donor-acceptor phases [2.144,2.147]. To obtain maximum PCE from an OSC, the donor-acceptor phase separation should be at optimum morphology for exciton dissociation, charge transport and limited exciton recombination simultaneously [2.148]. If this optimum morphology is achieved, it is usually not in a steady state and that results in evolution of the morphology over time towards an equilibrium state hence active layer changes are observed [2.149].

Similarly, the stability of the electrode and charge carrier transport layer can undergo internal changes over time even without external factor influence and result in inherent instability of the OSC. Commonly used electrode materials such as: aluminium (Al), indium tin oxide (ITO), have exhibited atomic diffusion into the active and transport layer of the OSC. Similarly, the transport layer such as PEDOT:PSS can also diffuse into the active layer of the OSC [2.145]. This diffusion of electrode and transport layer atoms into the active layer can lead to alterations in the energy band alignment of the active creating trap sites for non-radiative recombination and hence the degradation of the OSC [2.137]. Figure 2.23 shows a schematic that depicts some of the possible degradation mechanisms in OSC`s.

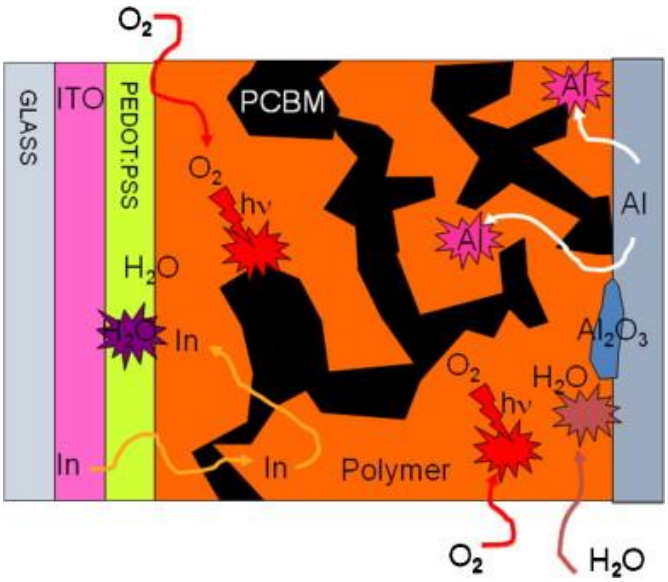

Figure 2.23: a schematic presentation of different degradation mechanisms in an organic solar cell [2.150].

2.7.2 Irradiation-light instability

In OSC`s, one of the most common degradation mechanisms is light-induced or photo degradation mechanism. This degradation mechanism poses an inevitable challenge to the realization of stable OSC`s since they operate under illumination. Light-induced instability can be classified into two classes: photochemical degradation and photophysical degradation [2.144].

During photochemical degradation, the donor and acceptor materials undergo a photo-oxidation process which transforms their chemical structures. The photo-oxidation of the donor (polymer) material results in formation of singlet oxygen and superoxide anions [2.151] while fullerene acceptor molecules can undergo photopolymerization under illumination. Furthermore, Kim et al. showed that non-fullerene acceptor materials can undergo fragmentation and chromophore bleaching [2.152]. This light-induced transformation of structures can lead to the loss of the photovoltaic ability of the donor-acceptor blend resulting in poor light absorption and exciton generation in the active layer [2.143]. Furthermore, photo-induced structural

changes on the active layer, can result in energy levels alignment changes and consequently lead to loss of PCE. The photo-oxidation of the active layer has been found to lead to formation of sub-bandgap states which become electron trap sites hence reduced electron mobility and enhanced non-radiative recombination become prominent.

PCBM, one of the most used fullerene acceptors can undergo photopolymerization after excessive exposure to sunlight [2.154]. Wantz et al. observed that oxidized PCBM species (PCBMox) are more likely to be electron acceptors (traps) which then hinders the efficiency of pure PCBM [2.155]. PCBMox creates even lower LUMO levels than those of pristine PCBM hence creating the electron traps along the PCBM domain [2.156]. A schematic of energy transfer level differences between pristine and a photo degraded P3HT:PCBM blend is shown in figure 2.24.

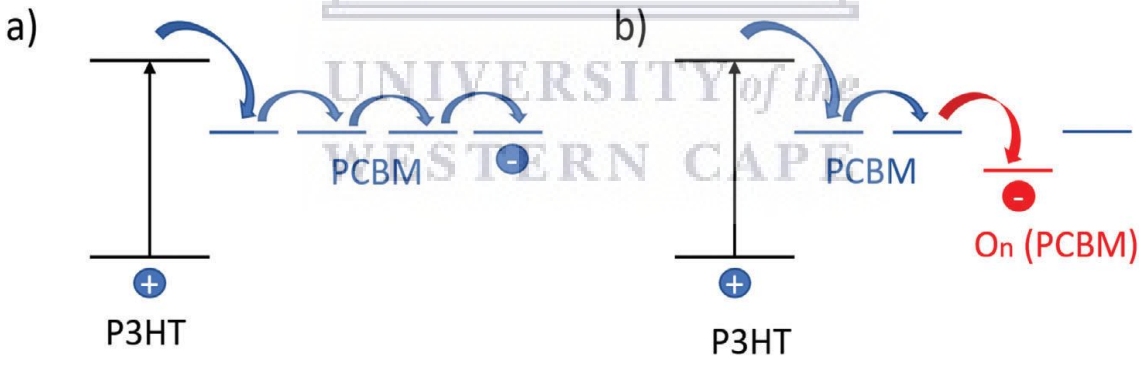

Figure 2.24: a schematic presentation of energy levels in (a) pristine P3HT:PCBM (b) deeper LUMO levels due to presence of $PCBMo_x$ [2.156].

In other works, the photo-degradation of fullerene acceptors has been found to lead to the creation of free radicals that can also decrease the solar cell performance. More recent literature on the instability of organics is discussed in detail by many review articles such as Duan et al. [2.145]. Several measures have been taken to

address this issue of instability of organic polymer blends and these includes incorporation of inorganic nanostructures with more stability and resistance to the factors highlighted in this work.

2.7.3 Thermal instability

Due to operating condition, OSC`s are exposed to higher working temperatures which cannot be avoided because of the continuous illumination of OSC`s by sunlight. Therefore, in a real-world operation scenario, thermally induced instability becomes one of the key OSC degradation causes [2.157,2.158]. Individually, the constituent materials used for OSC fabrication have enough resistance to decomposition at OSC operating temperatures and this shows that thermal instability is more linked to physical degradation.

In an OSC, continuous heating of the active layer can result in morphological evolution that may lead to a shift from optimum condition, hence thermal degradation [2.159]. As indicated under inherent instability, the optimum morphology for OSC performance may not necessarily be at equilibrium resulting in morphological evolution to equilibrium even without external factors. However, the additional thermal energy from extensive heating can also contribute to this evolution through accelerating it at even lower temperatures [2.160]. In polymer donors, it has been observed that heating at temperatures above their glass transition temperature (T_g) can result in improved mobility [2.161] and this is a result of further coarse phase separation that occurs because of the heating. In acceptor materials, the heating can result in more nucleation and crystallization of the polymer blend layer. This was demonstrated by Muller et al. [2.162] , whereby he achieved more aggregation and crystallization of PCBM through heating a TQ1:PCBM blended active layer and further observed a direct relation between crystallization and the applied temperature. At temperatures

higher than T_g of the blend, he observed aggregation of $PC_{61}BM$ which created a depletion zone around it and this depletion zone leads to a reduced D/A interface resulting in poor exciton dissociation and carrier transport [2.163].

Beyond the degradation of the active layer, heating can also cause induce degradation at the contact interface due to active layer morphological changes which can affect adhesion and result in poor electron extraction hence low PCE [2.164]. Uddin et al. demonstrated that fullerene ($PC_{71}BM$) and no-fullerene acceptors can degrade under thermal heating resulting in current leakages and poor charge extraction [2.165]. Furthermore, transport layers such as PEDOT:PSS have also exhibited a drop in electrical conductivity when heated.

2.7.4 Air instability

The exposure of OSC`s to ambient oxygen and water found in air can be damaging to the overall performance of an OSC device. Upon diffusion throughout the device or active layer, oxygen and water can result in the degradation of the active layer, transport layers and the electrodes. Oxidation of metal electrodes such as aluminium (Al) and calcium (Ca) can lead to formation of an oxide layer that is electrically insulating and a barrier to charge transport and extraction [2.166]. At the electrode interface, the formation of defects like pinholes can occur leading to poor PCE.

Carrier transport layers like PEDOT:PSS and molybdenum trioxide (MoO_3) can also absorb the water (H_2O) in ambient air that causes swelling/shrinking and this can eventually lead to delamination of the layer and a drastic drop in photocurrent [2.145]. As indicated previously, the absorption of water and oxygen by the active layer can alter their chemical structures, energy levels, absorption, and charge mobility. This

can also result in oxygen doping of the SC and permeation of oxygen atoms resulting in an increased hole concentration, drop in fill factor and lowered open circuit voltage of the cell.

2.7.5 Mechanical stress instability

Mechanical stress induced instability is one of the inevitable causes of degradation causes in OSC`s since it is built-in and accumulates within the OSC during layer-by-layer fabrication, transportation, and installation of such devices [2.167]. In real-world operation conditions, factors such as wind, rain and hail can also contribute to the mechanical stress of OSC`s. It has been observed that during mechanical stress degradation, tensile stress features more prominently than the vertical compressive stress [2.168].

The effects on mechanical stress in OSC`s can lead to different forms of degradation. Firstly, linear tensile stress can result in morphological changes due to the strained parts of the active layer and eventually lead to poor PCE of the device [2.169]. Secondly, mechanical stress can result in the delamination of the active layer, transport layers and the metal electrodes which then hinders charge transport and extraction due to surface area reduction [2.170]. In other instances, mechanical stress has been found to lead to the formation of cracks and deformations on the device layers, which then promotes the infiltration of oxygen and water hence aggravating the degradation of the device [2.171]. On the other hand, lateral strain can also cause degradation of layers of the OSC device with more prominent effects on the brittle ITO electrode layer and hence lead to drop in device performance [2.172]. However, lateral strain can be minimised by using materials with a higher strain tolerance.

2.8 Si NW / P3HT:PCBM Hybrid solar cells

As mentioned in previous sections, a significant amount of progress has been achieved in BHJ polymer solar cell development. However, several challenges and factors have been identified to be hindering the large-scale rollout of organic solar cells to compete against their matured conventional inorganic counterparts [2.173]. Instead of competition, one of the recent approaches is to combine both the organic and inorganic materials to make an organic-inorganic hybrid solar cell which has more potential for improved PCE [2.174]. The main aim of the hybrid BHJ approach seeks to address and overcome inherent challenges and limitations of organic based solar cells such as: the low charge carrier mobility and higher recombination rates. This is achieved through adding inorganic materials with higher mobility which provides a pathway for charge carriers from the active layer to contact electrodes as shown in figure 2.25.

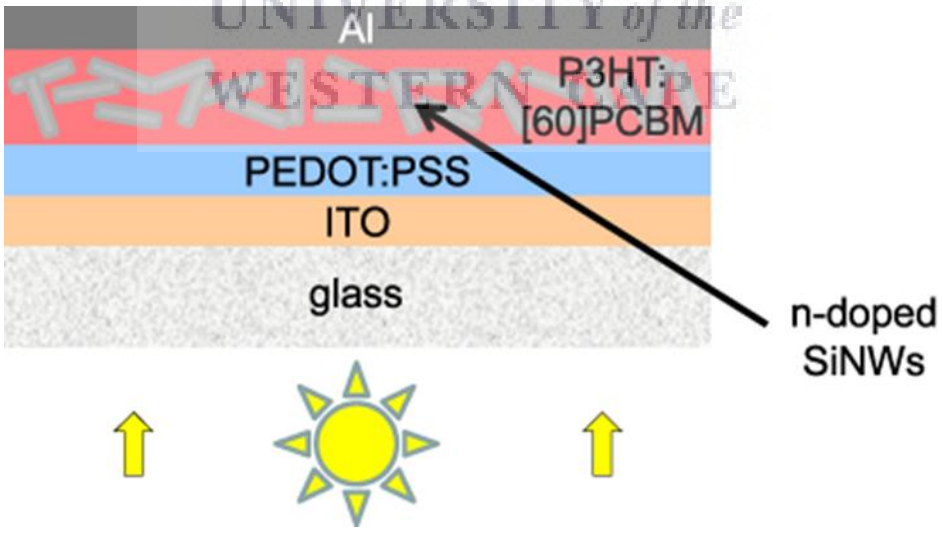

Figure 2.25: schematic of a hybrid SiNW/P3HT:PCBM solar cell [2.175].

The schematic in figure 2.25 shows a bulk heterojunction hybrid solar cell consisting of Si NWs dispersed in a polymer blend consisting of P3HT:PCBM. In other

works, these hybrid structures have been fabricated without the fullerene acceptor which led to a hybrid matrix consisting of Si NWs/P3HT only and this resulted in very low efficiencies. This is enough evidence to show that the incorporation of Si NWs as acceptor material in an organic polymer blend that has a fullerene acceptor results in the formation of a hybrid structure that can further utilise the benefits of 1-dimensional structures such as: rapid charge mobility, larger interfacial surface area for exciton dissociation and also charge carrier extraction at the electrode [2.176]. These act as an enhancement for the already existing fullerene acceptor in the polymer blend. A schematic depicting the energy band alignment in a hybrid solar cell is shown in figure 2.26.

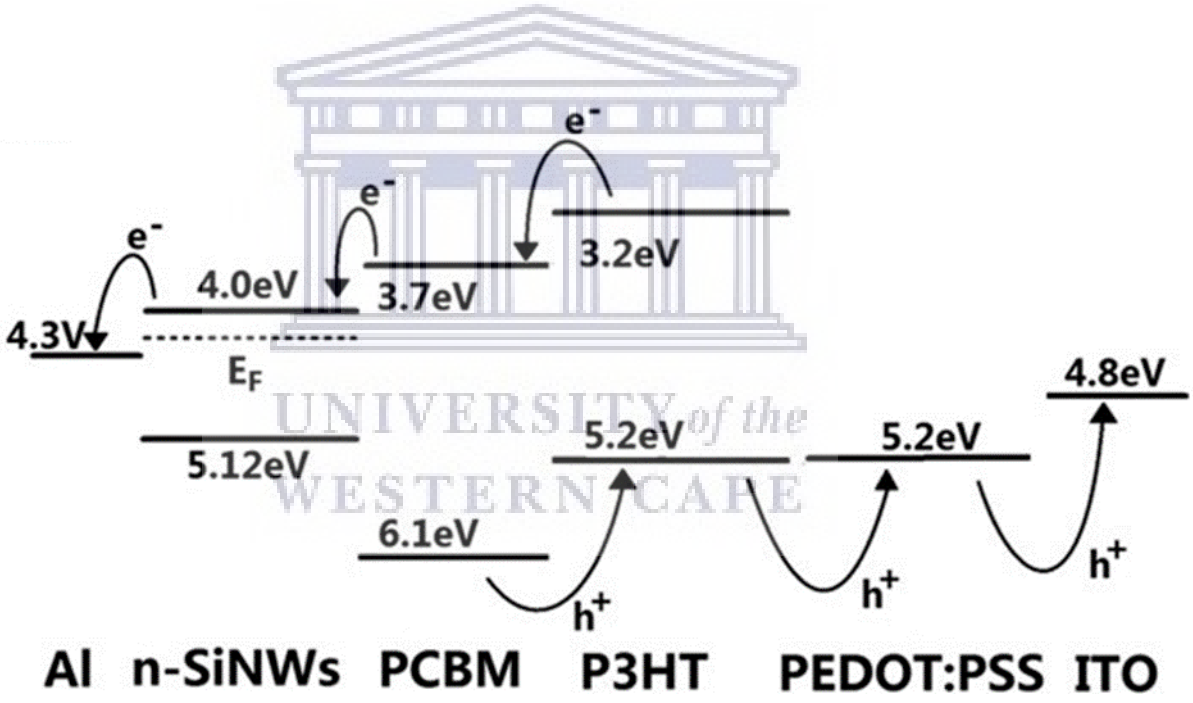

Figure 2.26: schematic of the energy level bands in a Si NW/ P3HT:PCBM blend hybrid solar cell [2.176].

Si NW/organic material hybrid solar cells can be classified into three categories based on the choice of light absorbing material and these categories can be identified as, type 1, type 2, and type 3 hybrid solar cells. In a type 1 hybrid solar cell, Si is utilized as the main light absorbing material while the role of organic counterparts is to create the potential difference within Si and provide medium for charge carrier

transportation. In this architecture, the charge collection efficiency of the Si/polymer interface is very crucial hence the conductivity of the organic material and the Si surface states are very important factors in determining the overall PCE of the hybrid solar cell.

In a type 2 hybrid solar cell, organic semiconducting materials such as P3HT are used as light absorbers to generate excitons while Si nanostructures are used as electron acceptor materials, hence this type can also be referred to as an excitonic SC [2.177]. In order to obtain high PCE, efficient exciton dissociation and charge carrier transportation is necessary. The third type of hybrid solar cells known as type 3 refers to those solar cells whereby both the organic and inorganic materials are utilised for efficient light absorption. This type of solar cell exhibits both type 1 and type 2 characteristics which implies that light absorption, exciton formation and dissociation occurs in both the Si and organic material used.

In most recent works, polymer/Si NW hybrid solar cells have been successfully fabricated resulting in greater PCE and even higher FF than a pure OSC [2.178]. These observed improvements can be solely attributed to the structural self-assembly in the active layer and no other additional solar cell optimization which implies that such improvements may also be realised with using other 1D materials like carbon nanotubes and various semiconductor NWs. Huang et al. [2.179], were able to demonstrate a significant improvement in current density from 7.17 to 11.6 $mA.cm^{-1}$ and an increased PCE from 1.2 to 1.9% through the incorporation of Si NWs in an organic P3HT/PCBM matrix. These low PCE values obtained were attributed to the thicker active layer of about 500 nm and a low open circuit voltage of 400 mV. Irrespective of the final obtained figures for the different parameters, these

enhancement values are a significant percentage increase and further confirm the huge potential of Si NWs in hybrid solar cells.

2.9 Summary and conclusion

This chapter begins with a discussion of the basic solar cell theory and the different measurable parameters. This is then followed by and in-depth discussion of how Si materials have become the materials of choice for photovoltaic applications from a structural to energy bands perspective. Specifically, Si nanostructured materials were discussed with more emphasis and a detailed literature review focusing on Si NWs.

The detailed discussion on Si NWs starts with a focus on the different fabrication approaches (methods) and techniques with more focus on the top-down approach known as metal-assisted chemical etching (MACE). The MACE process is then discussed in detailed covering the nucleation process, etching rate, direction, and porosity of the synthesized Si NWs. Properties of Si NWs such optical and electron transport properties were also discussed in detailed linking them to their morphological properties. The discussion of the MACE forms part of the core of this work on the following chapters.

Si NW based solar cells were also discussed in detail from their different junction geometries, their formation and contact electrodes. This was followed by a discussion of organic semiconductors focusing on their structural make-up and their energy bands. The common organic materials used for organic solar cells were also discussed followed by an in-depth look at operation of an organic solar cell. The different OSC architectures were also covered and an insight into the different instability challenges faced by OSC`s.

In conclusion, we observe that great strides have been achieved in the development of efficient hybrid solar cells. However, in most cases the emphasis is on the enhancement of efficiency alone, which neglects the other crucial challenges such as the costs involved in the development of such hybrid structures. This is evident from the fact that Si NWs used in most of the work done are synthesized using high-tech, costly methods hence the need to investigate quick and cost-effective methods of Si NW synthesis methods.

Furthermore, in most studies there is lack of individual investigation of the actual inorganic and organic species to be used in that particular study in order to clearly trace the transfer of individual properties into the hybrid structure in order to have a better understanding of the interactions involved.

References

2.1. C. Jiang, S.V.A. Moniz, A. Wang, T. Zhang, J. Tang, Chem. Soc. Rev., 46, (2017) 4645-4660.

2.2. A. Abass, PhD Thesis, University of Gent, Netherlands (2014).

2.3. Solar cell operation schematic diagram. Web address: https://www.pveducation.org/pvcdrom/solar-cell-operation/shunt-resistance

2.4. Solar cells: A guide to theory and measurement. Web address: https://www.ossila.com/pages/solar-cells-theory

2.5. L. C. Andreani, A. Bozzola, P. Kowalczewski, M. Liscidini, L. Redorici, Adv. Phys.-X., 4(1), (2018) 1548305.

2.6. M. A. Green, Progr. Photov.: Res. Appl. 17 (2009)183–189.

2.7. S. Mustafa, MSc Thesis, Erbil Polytechnic University, Iraq (2010).

2.8. P-type and N-type semiconductors. Web address: https://pediaa.com/difference-between-p-type-and-n-type-semiconductor/

2.9. F. Zhang, B. Sun, T. Song, X. Zhu, S. Lee, Chem.Mater. 23(8) (2011) 2084-2090.

2.10. C. Y. Kuo, C. Gau, Appl. Phys. Lett. 95(5) (2009) 053302-3.

2.11. K. Golap, A. Sudip, A. R. Hare, A. Rakesh, S. Tetsuo, S. Maheshwar, K. Wakita, U. Masayoshi, J. Phys. D Appl. Phys. 42(11) (2009) 115104.

2.12. L. He, C. Jiang, Rusli, D. Lai, H. Wang, Appl. Phys. Lett. 99(2) (2011) 021104.

2.13. W. U. Huynh, J. J. Dittmer, A. P. Alivisatos, Science. 295(5564) (2002) 2425-2427.

2.14. C. Y. Liu, Z. C. Holman, U. R. Kortshagen, Adv. Funct. Mater. 20(13) (2010) 2157-2164.

2.15. H. S. Nalwa, J. NanoSci. Nanotechnol., 11(12) (2011) 1-10.

2.16. H. Han, Z. Huang, W. Lee, Nano Today., 9(3) (2014) 271-304.

2.17. E. Garnett, P. Yang, Nano Lett. 10(3) (2010) 1082-1087.

2.18. K. J. Morton, G. Nieberg, S. Bai, S. Y.Chou, Nanotechnology. 19 (2008) 345301.

2.19. X. Li, P. W. Bohn, Appl. Phys. Lett. 77(16) (2000) 2572.

2.20. Y. Wu, Y. Cui, L. Huynh, C. J. Barrelet, D. C. Bell, C. M. Lieber, Nano Lett. 4 (2004) 433-436.

2.21. A. I. Hochbaum, R. Fan, R. He, P. Yang, Nano Lett. 5(3) (2005) 457-460.

2.22. J. V. Wittemann, W. Munchegesang, S. Senz, V. Schmidt, J. Appl. Phys., 107(9) (2010) 096105.

2.23. P. J. Alet, L. Yu, G. Patriarche, S. Palacin, P. Roca i Cabarrocas, J. Mater, Chem., 18 (2008) 5187.

2.24. L. Yu, B. O'Donnell, P. J. Alet, S. Conesa-Boj, . Peiro, J. Arbiol, Nanotechnology., 20 (2009) 225604.

2.25. S. Z. Khanyile, MSc Thesis, University of Western Cape (2015).

2.26. A. I. Hochbaum, R. Fan, R. He, P. Yang, Nano Letters, 5(3), (2005) 457-460.

2.27. C. S. Kong, MSc Thesis, University of Malaya, Kuala Lumpur (2012).

2.28. G. Cao, in 'Nanostructures & nanomaterials: synthesis, properties & applications', Imperial College Press publishers. (2004).

2.29. E. Comini, C. Baratto, G. Faglia, M. Ferroni, A. Vomiero, G. Sberveglieri, Prog. Mater. Sci., 54(1) (2009) 1-67.

2.30. D. D. D. Ma, C. S. Lee, F. C. K. Au, S. Y. Tong, S. T. Lee, Science, 299(5614), (2003) 1874-1877.

2.31. C. M. Hsu, S. T. Connor, M. X. Tang, Y. Cui, Appl. Phys. Lett., 93 (2008) 133109.

2.32. K. J. Morton, G. Nieberg, S. Bai, S. Y.Chou, Nanotechnology. 19 (2008) 345301.

2.33. X. Li, P. W. Bohn, Appl. Phys. Lett. 77(16) (2000) 2572.

2.34. S. Mitsugi, F. Koyama, A. Matsutani, Opt. Rev., 6(4) (1999) 378-379.

2.35. Y. Wang, T. Wang, P. Da, M. Xu, H. Wu and G. Zheng, Adv. Mater., 25 (2013) 5177.

2.36. Z. Huang, N. Geyer, P. Werner, J. de Boor and U. Gosele, Adv. Mater., 23 (2010) 285.

2.37. K. Q. Peng, J. J. Hu, Y. J. Yan, Y. Wu, H. Fang, Y. Xu, S. T. Lee, J. Zhu, Adv. Funct. Mater., 16 (2006) 387-394.

2.38. K. Peng, Y. Wu, H. Fang, X. Zhong, Y. Xu, J. Zhu, Angew. Chem. Int. Ed., 44 (18) (2005) 2737-2742.

2.39. S. K. Srivastava, D. Kumar, P. K. Singh, M. Kar, V. Kumar, M. Husain, Sol. Energy. Mater. Sol. Cells., 94(9) (2010) 1506-1511.

2.40. B. Hoffmann, V. Sivakov, S. W. Schmitt, M. Y. Bashouti, M. Latzel, J. Dluhos, J. Jiruse, S. Christiansen, Nanowires - Recent Advances, Xihong Peng, Intech., (2012) 211-230.

2.41. V. Sivakov, F. Vogit, B. Hoffmann,V. Gerliz, S. Christiansen, Nanowires - Fundamental Research. Intech., (2011) 45-80.

2.42. S. L. Cheng, C. H. Chung, H. C. Lee, J. Electrochem. Soc., 155 (2008).

2.43. K. Rykaczewski, O. J. Hildreth, C. P. Wong, A. G. Fedorov, J. H. J. Scott, Nano Lett., 11(2836) (2011).

2.44. K. Q. Peng , M. L. Zhang , A. J. Lu , N. B. Wong , R. Q. Zhang, S. T. Lee, Appl. Phys. Lett., 90(16) (2007).

2.45. X. G. Zhang, in 'Electrochemistry of Silicon and Its Oxide', Kluwer Academic/ Plenum Publisher, New York (2001).

2.46. H. Morinaga, M. Suyama, T. Ohmi, J. Electrochem. Soc. 141(1994) 2834-2841

2.47. W. Chern, K. Hsu, I. Chun, B. P. de Azeredo, N. Ahmed, K. H. Kim, Nano Lett., 10(15) (2010).

2.48. P. M. M. C. Bressers , J. J. Kelly , J. G. E. Gardeniers, M. Elwenspoek, J. Phys. Chem C., 143(5) (1996).

2.49. Z.P. Huang, T. Shimizu, S. Senz, Z. Zhang, N. Geyer, U. Gösele,J. Phys. Chem. C 114 (2010) 10683—10690.

2.50. H. Han, Z. Huang, W. Lee, Nano Today., 9 (2014) 271-304.

2.51. W. Chern, K. Hsu, I. S. Chun, B. P. de Azeredo, N. Ahmed, K. H. Kim, J. M. Zuo, N. Fang, P. Ferreira, X. Li, Nano Lett., 10 (2010) 1582-1588.

2.52. A. I. Hochbaum, D. Gargas, Y. J. Hwang, P. Yang, Nano Lett., 9 (2009) 3550-3554.

2.53. N. Geyer, B. Fuhrmann, H. S. Leipner, P. Werner, ACS Appl. Mater. Interfaces., 5(10) (2013) 4302-4308.

2.54. Y. Qu, L. Liao, Y. Li, H. Zhang, Y. Huang, X. Duan, Nano Lett., 9(12) (2009) 4539-4543.

2.55. X. Zhong, Y. Qu, Y.-C. Lin, L. Liao, D. Xiangfeng, ACS Appl. Mater. Interfaces., 3(2) (2011) 261-270.

2.56. K. Q. Peng, S. T. Lee, Adv. Mater., 23 (2011) 198-215.

2.57. J. Zhu, Z. Yu, G. F. Burkhard, C. M. Hsu, S. T. Connor, Y. Xu, Q. Wang, M. McGehee, 9(1) (2009) 279-282.

2.58. E. C. Garnett, M. L. Brongersma, Y. Cui, M. D. McGehee, Annu. Rev. Mater. Res., 41(1) (2011) 269-295.

2.59. V. Sivakov, G. Andrä, A. Gawlik, A. Berger, J. Plentz, F. Falk, S. H. Christiansen, Nano Lett., 9(4) (2009).

2.60. D. M. Callahan, J. N. Munday , H. A. Atwater, Nano Lett., 12(1) (2012) 214-218.

2.61. E. Yablonovitch, G. D. Cody, IEEE Trans. Electron Devices., 29(2) (1982) 300-305.

2.62. Z. Yu, A. Raman, S. Fan, Proc. Natl. Acad. Sci. USA., 107(41), (2010) 17491-17496.

2.63. E. Garnett, P. Yang, Nano Lett., 10(3) (2010) 1082-1087.

2.64. L. Hu, G. Chen, Nano Lett., 7(11) (2007) 3249-3252.

2.65. J. Li, H. Yu, S. M. Wong, X. Li, G. Zhang, P. G. Q. Lo, D. L. Kwong, Appl. Phys. Lett., 95(24) (2009).

2.66. M. Foldyna, L. Yu, P. Roca i Cabarrocas, Sol. Energy Mater. Sol. Cells., 117 (2013) 645-651.

2.67. M. Foldyna, L. Yu, S. Misra, P. Roca i Cabarrocas, Proc. SPIE. 8824, (2013).

2.68. S. N. Mohammad, J. Appl. Phys., 108, 034311 (2007).

2.69. Y. Qi, Z. Wang, M. Zhang, X. Wang, A. Ji, F. Yang, AIP Advances., 4, 031307 (2014).

2.70. M. Nolan, S. O' Callaghan, G. Fagas, J. C. Greer, T. Frauenheim, Nano Lett., 7(1) (2007) 34-38.

2.71. F. Sacconi, M. P. Persson, M. Povolotskyi, L. Latessa, A. Pecchia, A. Gagliardi, A. Balint, T. Fraunheim, A. D. Carlo, J. Comp. Electron., 6(1) (2007) 329-333.

2.72. Y. Cui, Z. Zhong, D. Wang, W. U. Wang, C. M. Lieber, Nano Lett., 3(2) (2003) 149-152.

2.73. K. Q. Peng, S. T. Lee, Adv. Mater., 23 (2011) 198-215.

2.74. B. K. Teo, X. H. Sun, Chem. Rev., 107 (2007) 1454-1532.

2.75. Y. Kobayashi, S. Adachi, Jpn. J. Appl. Phys., 49 (2010) 075002.

2.76. H. N. Cong, M. Dieng, C. Sene, P. Chartier, Sol. Energy Mater. Sol. Cells., 63(1) (2000) 23-35.

2.77. L. B. Roberson, M. A. Poggi, J. Kowalik, G. P. Smestad, L. A. Bottomley, L. M. Tolbert, Coord. Chem. Rev., 248(13) (2004) 1491-1499.

2.78. C. Lévy-Clément, R. Tena-Zaera, M. A. Ryan, A. Katty , G. Hodes, Adv. Mater., 17(12) (2005) 1512-1515.

2.79. K. Wang, J. J. Chen, Z. M. Zeng, J. Tarr, W. L. Zhou, Y. Zhang, Y. F. Yan, C. S. Jiang, J. Pern, A. Mascarenhas, Appl. Phys. Lett., 96(12) (2010).

2.80. M. K. Sahoo, P. Kale, J. Materiomics. 5 (2019) 34-48.

2.81. E. C. Garnett, P. Yang, J. Am. Chem. Soc., 130(29) (2008).

2.82. B. Tian, X. Zheng, T. J. Kempa, Y. Fang, N. Yu, Nature., 449(7164) (2007) 885-889.

2.83. V. Sivakov, G. Andra, A. Gawlik, A. Berger, J. Plentz, Nano Lett, 9(4) (2009) 1549-1554.

2.84. H. Fang, X. Li, S. Song, Y. Xu, J. Zhu, Nanotechnology., 19(25) (2008).

2.85. E. C. Garnett, Y. Tseng, D. R. Khanal, J. Wu, J. Bokor, P. Yang, Nat. Nanotechnol., 4(5) (2009) 311-314.

2.86. J. C. Ho, R. Yeshuralmi, Z. A. Jacobson, Z. Fan, R. L. F. Alley, A. Javey, Nature Mater., 7(1) (2008) 62-67.

2.87. A. L. Briseno, T. W. Combe, A. I. Boukai, E. C. Garnett, S. W. Shelton, Nano. Lett., 10(1) (2010) 334-340.

2.88. Z. Fan, H. Razavi, J. Do, A. Moriwaki, O. Ergen, Nature Mater., 8(8) (2009).

2.89. X. Wang, H. Shen, S. M. Eichefield, T. S. Mayer, J. M. Redwing, IEEE J. Photovolt., 6(6) (2016) 1446-1450.

2.90. Q. Shu, J. Wei, K. Wang, H. Zhu, Z. Li, Y. Jia, Nano Lett., 9 (2009) 4338-4442.

2.91. G. Jia, A. Galwik, J. Bergman, B. Eisenhawer, S. Schonherr, G. Andra, IEEE J. Photovolt., 4 (2014) 28-32.

2.92. B. Eisenhawer, I. Sill, F. Falk, Phys. Status Solidi Appl Mater Sci., 210(4) (2013) 695-700.

2.93. G. Dong, Y. Zhou, RSC Adv., 7 (2017) 45101-45106.

2.94. F. Khan, S. H. Baek, J. H. Kim, 137 (2016) 122-128.

2.95. M. Sharma, P. R. Pudasaini, F. Ruiz-Zepeda, D. Elam, A. A. Ayon, ACS Appl. Mater. Interfaces., 6(6) (2014) 4356-4363.

2.96. H. J. Syu, S. C. Shiu, C. F. Lin, Conf Rec IEEE Photovolt. Spec. Conf., (2011).

2.97. Z. Ge, L. Xu, Y. Cao, T. Wu, H. Song, Z. Ma, Nanoscale Res. Lett., 10 (2015) 1-8.

2.98. N. Chehata, A. Ltaief, B. Ilahi, B. Salam, A. Bouazizi, H. Mareef, Synth. Met., 191 (2014) 6-11.

2.99. Y. Cheng, G. Fang, C. Li, L. Yuan, L. Ai, B. Chen, X. Zhao, Z.Chen, W. Bai, C. Zhan, J. Appl. Phys., 102 (2007) 083516.

2.100. W. Lu, C. Wang, W. Yue, L. Chen, Nanoscale., 3 (2011) 3631-3634.

2.101. S. H. Tsai, H. C. Chang, H. H. Wang, S. Y. Chen, C. A. Lin, S. A. Chen, Y. L. Chueh, J. H. He, ACS Nano., 5 (2011) 9501-9510.

2.102. M. M. Adachi, M. P. Anantram, K. S. Karim, Sci. Rep., 3 (2012)1546.

2.103. S. C. Shiu, J. J. Chao, S. C. Hung, C. L. Yeh, C. F. Lin, Chem. Mater., 22 (2010) 3108-3113.

2.104. X. Shen, B. Sun, D. Liu, S. T. Lee, J. Am. Chem. Soc., 133 (2011) 19408-19415.

2.105. F. Zhang, X. Han, S. T. Lee, B. Sun, J. Mater. Chem., 22 (2012)5362-5368.

2.106. S. A. Moiz, A. M. Nahhas, H. D. Um, S. W. Jee, H. K. Cho, S. W. Kim, J. H. Lee, Nanotechnology., 23 (2012) 145401.

2.107. N. Chehata, A. Ltaief, E. Beyou, B. Ilah, B. Salem, T. Baron, J. Lumin., 168 (2015) 315-324.

2.108. S. Shao, K. Zheng, K. Zidek, P. Chabera, T. Pullerits, F. Zhang, Sol. Energy Mater. Sol. Cells., 118 (2013) 43-47.

2.109. P. -J. Alet, PhD Thesis, Ecole Polytechique, France (2009)

2.110. T. Jeon, PhD Thesis, Ecole Polytechnique, France (2013)

2.111. M. Pope, C. E. Swenberg, in 'Electronic Processes In Organic Crystals and Polymers', Oxford University Press (2009).

2.112. H. Sirringhaus, P. J. Brown, R. H. Friend, M. M. Nielsen, K. Bechgaard, B. M. W. Langeveld-Voss et al., Nature., 401, (1999) 685-688.

2.113. T. A. Chen, X. M. Wu, R. D. Rieke, J. Am. Chem. Soc., 117(1), (1995) 233-244.

2.114. Y. Kim, Nat. Mater., 5(3), (2006) 197.

2.115. J. -M. Verilhac, G. LeBlevennec, D. Djurado, F. Rieutord, M. Chouiki, J. -P. Travers, A. Pron, Synth Met., 156, (2006) 815-823.

2.116. J. F. Chang, B. Sun, D. W. Breiby, M. M. Nielsen, T. I. Solling, M. Giles et al., Chem. Mater., 16(23), (2004)

2.117. M. Surin, Ph. Leclere, R. Lazzaroni, J. Appl. Phys., 100(3), (2006).

2.118. S. Cho, K. Lee, J. Appl. Phys., 100(11), (2006).

2.119. Y. Kim, Nat. Mater., 5(3), (2006) 197.

2.120. Y. Kim, D. D. C. Bradley, Curr. Appl. Phys., 5(3), (2005).

2.121. Y. Kim, A. Ballatyne, J. Nelson, D. Bradley, Org. Electron., 10(1), (2009) 205-209.

2.122. T. Jeon, B. Geffroy, D. Tondelier, L. Yu, et al., Sol. Energy Mater. Sol. Cells., 117, (2013) 632-637.

2.123. M. M. Wienk, M. Turbiez, J. Gilot, A. J. Jansen, Adv. Mater., 20(13), (2008) 2556-2560.

2.124. M. T. Dang, , L. Hirsch, G. Wantz, Adv. Mater., 23(11), (2011) 3579-3602

2.125. T. Ikenoue, H. Nishonaka, S. Fujita, Thin Solid Films., 520(6), (2012) 1978-1981.

2.126. S. R. Hammond, et al., J. Mater. Chem., 22(7), (2012) 3249-3254.

2.127. S. Hou, X. Cai, H. Wu, Z. Lv, D. Wang, Y. Fu, D. Zou, J. Power Sour., 215, (2012) 164–169.

2.128. N.S. Sariciftci, L. Smilowitz, A.J. Heeger, F. Wudl, Science., 258 (1992) 1474.

2.129. T. Aernouts, W. Geens, J. Poortmans, P. Heremans, S. Borghs, R. Mertens. Thin Solid Films., 297, (2002) 403-404.

2.130. G. Dennler, M. C. Scharber, and C. Brabec, Adv. Mater., 21(13), (2009) 1323-1338.

2.131. G. Namkoong, P. Boland, K. Lee, and J. Dean, J. Appl. Phys., 107(12), (2010) 124515.

2.132. C. Soci, I.-W. Hwang, D. Moses, Z. Zhu, D. Waller, R. Guadiana, C. J. Brabec, A. J. Heeger, Adv. Funct. Mater., 17, (2007) 632.

2.133. C.J. Brabec, A. Cravino, D. Meissner, N.S. Sariciftci, T. Fromherz, M.T. Rispens, L. Sanchez, J.C. Hummelen, Adv. Funct. Mater., 11, (2001) 374.

2.134. L. Hung, C. Tang, and M. Mason, Appl. Phys. Lett., 70(2), (1997) 152-154.

2.135. H. Bässler, Physica Status Solidi B: Basic Research., 175 (1993) 15.

2.136. I. Montanari, A. F. Nogueira, J. Nelson, J. R. Durrant, C. Winder, M. A. Loi, N. S. Sariciftci, C. Brabec, App. Phys. Lett. 81 (2002) 3001.

2.137. R. N. Marks et al., J. Phys.: Condens. Matter., 6, (1994) 1379.

2.138. C. W. Tang, Appl. Phys. Lett., 48 (1986) 183.

2.139. C. J. Brabec, G. Zerza, G. Cerullo, S. De Silvestri, S. Luzzati, J. C. Hummelen, S. Sariciftci, Chem. Phys. Lett., 340, (2001) 232.

2.140. J.J.M. Halls, C.A. Walsh, N.C. Greenham, E.A. Marseglia, R.H. Friend, S.C. Moratti, A.B. Holmes, Nature., 376, (1995) 498.

2.141. B. Fan, D. Zhang, M. Li, W. Zhong, Z. Zeng, L. Ying, F. Huang, Y. Cao, Sci. China: Chem., 62, (2019) 746.

2.142. Y. Lin, B. Adilbekova, Y. Firdaus, E. Yengel, H. Faber, M. Sajjad, X. Zheng, E. Yarali, A. Seitkhan, O. M. Bakr, A. El-Labban, U. Schwingenschlögl, V. Tung, I. McCulloch, F. Laquai, T. D. Anthopoulos, Adv. Mater., 31, (2019) 1902965.

2.143. H. Kang, G. Kim, J. Kim, S. Kwon, H. Kim, K. Lee, Adv. Mater., 28, (2016) 7821.

2.144. P. Cheng, X. Zhan, Chem. Soc. Rev.,45, (2016) 2544.

2.145. L. Duan, A. Uddin, Adv. Sci., 7, (2020) 1903259.

2.146. X. Du, T. Heumueller, W. Gruber, A. Classen, T. Unruh, N. Li, C. J. Brabec, Joule., 3, (2019) 215.

2.147. S. Rafique, S. M. Abdullah, K. Sulaiman, M. Iwamoto, Renewable Sustainable Energy Rev., 84, (2018) 43.

2.148. M. C. Heiber, C. Baumbach, V. Dyakonov, C. Deibel, Phys. Rev. Lett., 114, (2015) 136602.

2.149. B. Conings, S. Bertho, K. Vandewal, A. Senes, J. D'Haen, J. Manca, R. A. J. Janssen, Appl. Phys. Lett., 96, (2010) 163301.

2.150. M. Jørgensen, K. Norrman, F. C. Krebs, Sol. Energy Mater. Sol. Cells., 92, (2008) 686.

2.151. S. T. Lee, Z. Q. Gao, L. S. Hung, Appl. Phys. Lett., 75, (1999) 1404.

2.152. J. Luke, E. M. Speller, A. Wadsworth, M. F. Wyatt, S. Dimitrov, H. K. H. Lee, Z. Li, W. C. Tsoi, I. McCulloch, D. Bagnis, J. R. Durrant, J.-S. Kim, Adv. Energy Mater., 9, (2019) 1803755.

2.153. F. Deschler, A. De Sio, E. von Hauff, P. Kutka, T. Sauermann, H.-J. Egelhaaf, J. Hauch, E. Da Como, Adv. Funct. Mater., 22, (2012) 1461.

2.154. S. Pont, F. Foglia, A.M. Higgins, J. R. Durrant, J. T. Cabral, Adv. Funct. Mater., 28, (2018) 1802520.

2.155. A. Perthue, T. Gorisse, H. S. Silva, C. Lombard, D. Begue, P. Hudhomme, B. Pepin-Donat, A. Rivaton, G. Wantz, J. Mater. Res., 33, (2018) 1868.

2.156. M. O. Reese, A. M. Nardes, B. L. Rupert, R. E. Larsen, D. C. Olson, M. T. Lloyd, S. E. Shaheen, D. S. Ginley, G. Rumbles, N. Kopidakis, Adv. Funct. Mater., 20, (2010) 3476.

2.157. A. Agresti, S. Pescetelli, Y. Busby, T. Aernouts, IEEE Trans. Electron Devices., 66, (2019) 678.

2.158. N. Chander, S. Singh, S. S. K. Iyer, Sol. Energy Mater. Sol. Cells., 161, (2017) 407.

2.159. C. J. Schaffer, C.M. Palumbiny, M. A. Niedermeier, C. Jendrzejewski, G. Santoro, S. V. Roth, P. Müller-Buschbaum, Adv. Mater., 25, (2013) 6760.

2.160. I. F. Domínguez, A. Distler, L. Lüer, Adv. Energy Mater., 7, (2017) 1601320.

2.161. G. A. Brehm, V. A. Bloomfield, Macromolecules., 8, (1975) 663.

2.162. C. Lindqvist, A. Sanz-Velasco, E. Wang, O. Bäcke, S. Gustafsson, E. Olsson, M. R. Andersson, C. Müller, J. Mater. Chem. A., 1, (2013) 7174.

2.163. H. Cao, W. He, Y. Mao, X. Lin, K. Ishikawa, J. H. Dickerson, W. P. Hess, J. Power Sources., 264, (2014) 168.

2.164. I. T. Sachs-Quintana, T. Heumüller, W. R. Mateker, D. E. Orozco, R. Cheacharoen, S. Sweetnam, C. J. Brabec, M. D. McGehee, Adv. Funct. Mater., 24, (2014) 3978.

2.165. L. Duan, H. Yi, Y. Zhang, F. Haque, C. Xu, A. Uddin, Sustainable Energy Fuels., 3, (2019) 723.

2.166. M. Glatthaar, M. Riede, N. Keegan, K. Sylvester-Hvid, B. Zimmer-mann, M. Niggemann, A. Hinsch, A. Gombert, Sol. Energy Mater. Sol. Cells., 91, (2007) 390.

2.167. P. Sommer-Larsen, M. Jørgensen, R. R. Søndergaard, M. Hösel, F. C. Krebs, Energy Technol., 1, (2013) 15.

2.168. X. Xu, K. Fukuda, A. Karki, S. Park,H. Kimura, H. Jinno,N.Watanabe, S. Yamamoto, S. Shimomura, D. Kitazawa, T. Yokota, S. Umezu, T.- Q. Nguyen, T. Someya, Proc.Natl. Acad. Sci. U. S. A., 115, (2018) 4589.

2.169. V. Balcaen, N. Rolston, S. R. Dupont, E. Voroshazi, R. H. Dauskardt, Sol. Energy Mater. Sol. Cells., 143, (2015) 418.

2.170. N. R. Tummala, C. Bruner, C. Risko, J.-L. Brédas, R. H. Dauskardt, ACS Appl. Mater. Interfaces., 7, (2015) 9957.

2.171. S. Juillard, E. Planes, M. Matheron, L. Perrin, S. Berson, L. Flandin, ACS Appl. Mater. Interfaces., 10, (2018) 29805.

2.172. S.-I. Na, S.-S. Kim, J. Jo, D.-Y. Kim, Adv. Mater., 20, (2008) 4061.

2.173. M.A. Green, K. Emery, Y. Hishikawa, W. Warta, E.D. Dunlop, Prog. Photovolt.: Res. Appl., 22, (2014) 701.

2.174. A.L. Briseno, T.W. Holcombe, A.I. Boukai, E.C. Garnett, S.W. Shelton, J.J. M. Fréchet, P. Yang, Nano Lett. 10, (2010) 334.

2.175. B. Eisenhawer, S. Senfuss, V. Sivakov, M. Pietsch, G. Andra, F. Falk, Nanotechnology, 22, (2011) 31401.

2.176. K. Liu, S. Qu, X. Zhang, F. Tan, Z. Wang, Nanoscale Res. Lett., 8, (2013) 88.

2.177. B. A. Gregg, J. Phys. Chem. B., 107(20), (2003) 4688-4698.

2.178. N. Chehata, A. Ltaief, B. Ilahi, B. Salem, A. Bouazizi, H. Maaref, E. Beyou, T. Baron, P. Gentile, Synth. Met., 191, (2014) 6.

2.179. J. Huang, C. Hsiao, S. Syu, J. Chao, C. Lin, Sol. Energy Mater. Sol. Cells., 93, (2009) 621-624.

Chapter 3

Fabrication and Characterization of Defects in Doped Silicon Nanowires Produced by MACE

Abstract

In this chapter, we report on the successful fabrication of silicon nanowires using the metal assisted chemical etching method for different etching durations and the doping of these intrinsic Si NWs with $POCl_3$. Scanning electron microscopy revealed the correlation between the etching time and the morphological properties such as length of the as-grown Si NWs. The Si NWs were found to have diameters ranging from about 80 nm to 200 nm and their lengths ranging from about 1 μm to 4 μm. Low energy EDS analysis performed in a SEM showed a uniform distribution of phosphorus within the doped Si NWs. High resolution transmission electron microscopy HRTEM confirms the phosphorus incorporation and further revealed that the Si NWs had a crystalline core and amorphous silicon oxide shell structure with some Si nanocrystals embedded in it. The doped Si NWs exhibited strong photoluminescence emission bands, which were linked to structural defects such as Si nanocrystals embedded in a defective SiO_2 matrix and porosity. The Si NWs displayed enhanced anti-reflective properties with reflection values dropping below 2 %. Hall-effect measurements also showed improved conductivity of the doped Si NWs compared to the intrinsic Si NWs. XPS surface analysis of the doped samples exhibited a coexistence of Si n and p type bonds confirming a successful doping process of the Si NWs.

3.1. Introduction

Nanostructured silicon (Si) materials have attracted widespread research interests in various fields and applications due to their unique morphological, structural, optical, and electrical properties when compared to their bulk counterparts [3.1]. Nanostructured Si materials such as Si nanowires (Si NWs) have been investigated for photovoltaic and energy storage applications [3.2] due to their superior optical and electrical properties which are crucial for solar cell and battery development [3.3]. Favourably, for solar cell applications, vertical Si NW arrays have been found to display drastic antireflective (AR) properties because of their wide optical absorption band and multiple internal scattering effects, which lead to enhanced trapping of incident light and subsequently enhanced absorption [3.4,3.5]. Furthermore, the one-dimensional nature of Si NWs renders them as ideal candidates for incorporation in organic photovoltaic cells as charge carriers and even electron accepting materials [3.6].

In recent times, the MACE method has become one of the widely used techniques for rapid synthesis of well aligned array of Si NWs [3.7,3.8]. Furthermore, MACE provides an ability to control crucial Si NW parameters such as cross-sectional shape, diameter, length, orientation, doping type, and dopant levels [3.7]. These factors have led to an increase in MACE Si NW growth for solar cell applications [3.3] including hybrid organic/inorganic PVs due to their high yield and easy harvesting [3.6]. MACE grown Si NWs have been known to exhibit a broad range of diameters with walls which can be decorated by Si or metal nanocrystals (NCs) varying in size and this combination of factors yields a broad optical absorption band and also enhanced photoluminescence (PL) even in the near infra-red region at room temperature [3.8-10].

Generally, the aspect ratio and large surface area of MACE Si NWs is crucial in enhancing dopant thermal diffusion for high doping levels due to the larger surface area hence improved electron transport. Furthermore, p-type and heavily doped Si NWs have been found to be ideal for forming ohmic contacts which shows the importance of understanding their electronic properties since they can be greatly influenced by dimensions, dopant level and other material characteristics [3.11]. The doping of Si NWs is crucial in the understanding of fundamental issues associated with electron transport in a 1-dimensional structure [3.12].

Several works have been done on the properties of MACE Si NWs [3.1,3.13], however it is still critical to interrogate the intricate relationship between the unique morphological, structural, optical, and electronic properties to explore potential applications. Si nanostructured materials such as Si NWs, Si NCs and porous Si have always been known to emit light (PL) of different wavelengths depending on their size, doping levels and surface features even though bulk Si is an indirect band gap material [3.8]. Several proposals [3.8,3.9,3.14] have been made to explain the origin of the observed PL without full agreement hence there is still a need to establish the origin of the observed PL and its effects on the various applications of MACE Si NWs. This work presents a unique correlation between a wide range of advanced characterisation techniques to explore the structural defects and their effects in Si NW properties and applications.

3.2. Experimental Details

The growth of Si NW arrays was achieved by using p-type (boron doped) Si (100) wafers with a resistivity of about 1-10 Ω.cm, cut to 1 x 1 cm^2 and 2 x 2 cm^2 substrates. Substrate cleaning was done by a 3-step ultra-sonication process in acetone, ethanol, and isopropanol for 5 minutes, respectively and then air dried. The final cleaning step involved dipping the samples in 5% hydrofluoric acid (HF) solution for 3 minutes followed by rinsing in deionized water and then allowed to air dry in preparation for metal catalyst deposition.

The MACE of the Si wafers was achieved using a two-step process. Firstly, a thin layer of Ag nanoparticles (AgNPs) was deposited on all the clean substrates by dipping them in a solution that was a mixture of 5 M HF acid and 0.02 M silver nitrate ($AgNO_3$) solution for 60 s followed by rinsing in deionized water. A mixture containing 0.5 M hydrogen peroxide (H_2O_2) and 5 M HF acid was used as an etchant solution whereby the different AgNPs coated substrate were immersed in for different durations ranging from 5, 10, 20 and 30 minutes. The etched samples were then dipped in a nitric acid (HNO_3) solution and rinsed with deionized water to remove any remnant AgNPs.

Doping of some of the as grown Si NWs was achieved by spin coating a phosphor oxychloride ($POCl_3$) solution onto the samples in two stages being 500 and 2000 rpm for 9 and 20 s, respectively. These samples were then annealed in a tube furnace under argon (Ar) ambient for 20 minutes at 900 °C and atmospheric pressure. Afterwards, some of the doped samples were further treated by dipping them in dilute HF acid for 1 minute in order to remove the phosphosilicate glass (PSG) layer formed during annealing.

The structural properties of the grown Si NWs were investigated using a Zeiss Leo 1525 field emission scanning electron microscope (FESEM) operated at low voltages of about 5 kV. Advanced low kV windowless SEM EDS analysis was conducted using an OXFORD X-Max Extreme Zeiss Merlin operated at 3kV, 130 pA and a working distance of 4.8 mm. To probe the internal structure and crystallographic information of the samples, a Tecnai F20 high resolution transmission electron microscope equipped with an energy dispersive x-ray (EDX) spectrometer operated at an acceleration voltage of 200 kV. A PANalytical empyrean series 2 x-ray diffractometer operated at 45 kV and 40 mA was used to conduct XRD analysis at a grazing incidence of 0.3°.

The photoluminescence (PL) properties were investigated using a NanoLog® Horiba spectrofluorometer and a 325 nm Xenon laser. UV- Vis analysis was conducted using a Semicon Soft M probe thin film measuring spectrophotometer using halogen and deuterium lamps as the visible and ultraviolet light sources, respectively. Electronic properties of the grown samples were investigated using an ECOPIA HMS-300 Hall Measurement System using the Van der Pauw method, at room temperature with a magnetic field of about 0.55 T and operated at varying current of 0.1, 0.25, 0.5, 0.75 and 1 µA. The chemical bonding analysis of the Si NWs was performed using a Thermo-ESCAlab 250Xi equipped with a monochromatic Al kα x- ray beam.

3.3. Results and Discussion

3.3.1. Si NW morphology

3.3.1.1. Intrinsic Si NWs

The morphological properties of the: Ag-coated Si substrate, as-grown and doped Si NW arrays were investigated using scanning electron microscopy. Figure 3.1(a) shows the SEM aerial micrograph of the Ag coated Si substrate; where an interlinked, dense network of Ag agglomerates are evident with a wide diameter range from ~200 nm to 1 µm of the individual Ag nanoparticles (AgNPs), which are expected to act as etching sites during the MACE of Si NW arrays. It is anticipated that the distribution and morphology of the AgNPs determines the diameter, morphology, distribution and aspect ratio of the resultant SiNWs [3.15].

A well-defined, vertically aligned Si NW array is evident after etching in the HF/H_2O_2 solution for 5 minutes, as seen in the cross-sectional SEM micrograph in figure 3.1(b). The Si NW length is uniform at ~1 µm with the etching in the <100> direction. The etching solution in this study has been intended such that the HF/H_2O_2 molar ratio is sufficiently low to ensure preferential removal/etching of the low number of Si atoms in the (100) plane, thereby resulting in the <100> etching direction [15]. An increase in the acid to oxidant molar ratio results in alternative etching directions that contain more Si atoms [7].

The dense, interconnected Ag network observed in figure 3.1(a) also limits the lateral movement of the Ag nanoparticles, thereby promoting preferential etching in vertical <100> direction. The SiNW diameter ranges from 80 – 200 nm, which is attributed to the non-uniform AgNP distribution as indicated in [3.15], while the minimal bending is due to the rigidity of the shorter structures.

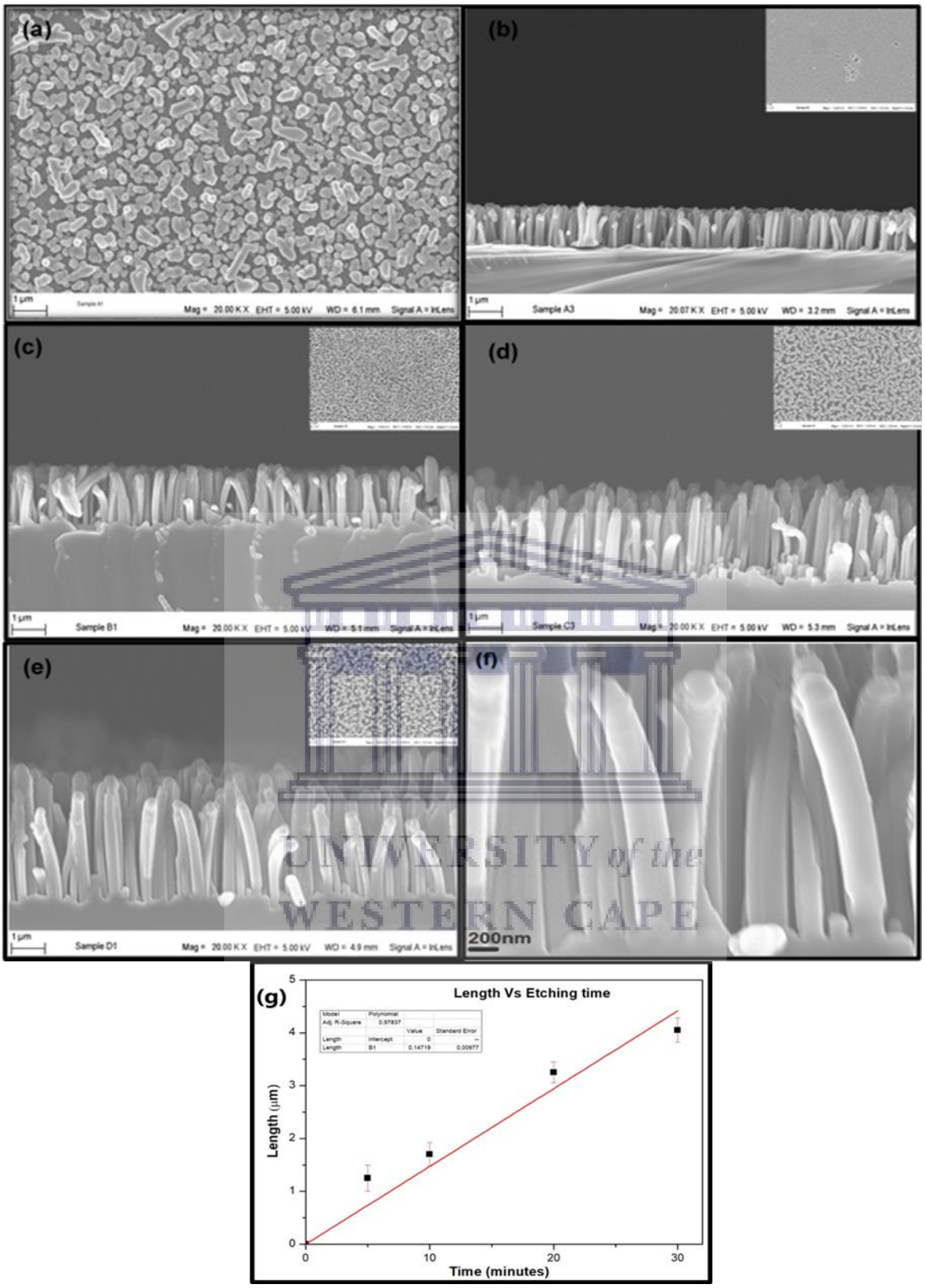

Figure 3.1: Top-view images of (a) Ag NPs (b) intrinsic Si NWs and the Si NW array cross-section of samples etched for (c) 5 (d) 10 (e) 20 and (f) 30 minutes while (g) shows the etching.

Figure 3.1(c-e) shows the evolution of the Si NW with prolonged etching time. A linear increase in the Si NW length is observed with etching time, resulting in an average vertical etching rate of about 0.147 µm per minute (Figure 3.1g). The Si NW/Si substrate interface is more irregular (not well-defined) as the etching time is increased, which results in a reduction in the uniformity of the Si NW length. We ascribe this to non-uniform AgNPs size and increased exposure to the H_2 gas (as a reaction product) during the etching process. The H_2 gas further promotes the delamination of AgNPs from the Si surface, thereby obstructing the required intimate contact between the Ag and Si substrate resulting in the breakdown of the MACE process. Remnant Ag particles from the synthesized NWs are removed by dipping the samples in HNO_3 to ensure a pristine Si NW array.

From the insets it is evident that the bundling of the Si NWs at the tips increases with aspect ratio (or etching time), which is ascribed to the surface tension forces exerted on the Si NWs during drying. The Si NW diameter distribution is fixed with etching time, while the roughness/porosity of the Si NWs increases, specifically at the tips. This is demonstrated in the high-magnification SEM micrograph in figure 3.1(f) and this porosification is associated with the secondary MACE process on the sidewalls of the Si NWs due to remnant Ag ions upon extended etching times.

During the overall etching process the dissolution of Ag nanoparticles by H_2O_2 at the etching front can result in the subsequent nucleation of the Ag^+ ions at defective sites (dopant atoms) on the Si NW sidewall [3.5,3.6]. It should be reiterated that the original Si substrate is slightly p-doped and this results in the formation of smaller Ag particles on the Si NW walls, which create random lateral etching pathways resulting in a porous structure. The enhanced roughness at the tip is due to the increase in the Ag^+ concentration at the top leading to an increased Si oxidation. Bundling of the Si

NW-tips with etching time can also been attributed to the reduced rigidity and increased strain caused by the porosification process [3.1,3.7,3.15].

3.3.1.2. Doped Si NWs

The intrinsic Si NWs were then n-doped by spin coating a $POCl_3$ solution followed by annealing at 900 °C for 20 minutes. Figure 3.2 (a) shows an aerial view of a sample etched for 30 minutes and n-doped while (b) shows a similar sample that has been further treated by dipping in dilute HF acid for cleaning. The cross-sectional images of both samples are shown in figure 3.2 (c) and (d), respectively.

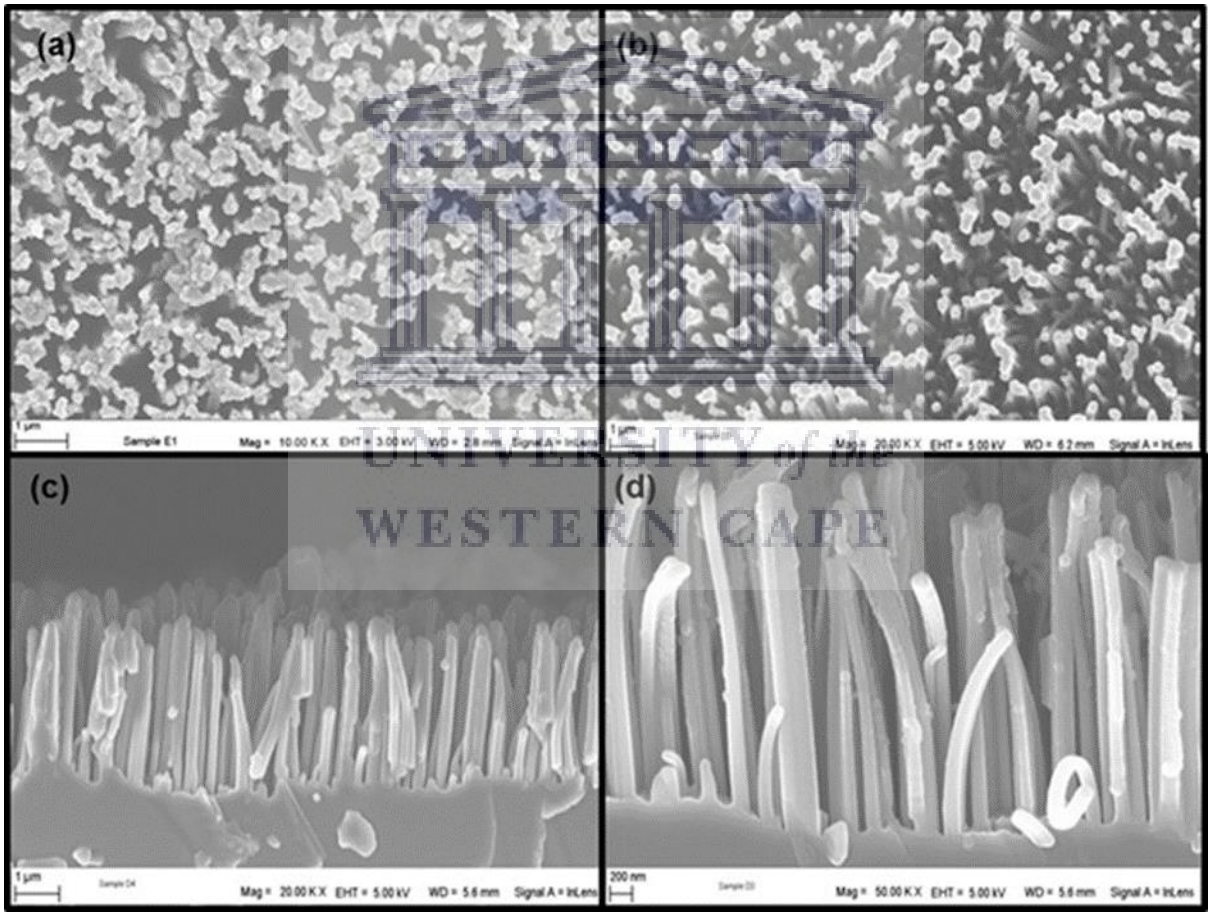

Figure 3.2: Top-view images of samples etched for 30 minutes (a) n-doped (b) n-doped and cleaned in dilute HF acid and their corresponding cross-sectional images in(c) and (d) respectively.

The SEM analysis revealed that the doped/uncleaned sample is characterised by several dense bundles of non-uniform Si NWs. From the top view, it can be clearly observed that individual NWs are indistinguishable from one another due to this bundling effect that is caused by the thin $POCl_3$ layer spin coated on the samples during the n-doping process. On the other hand, the SEM aerial view of the doped/cleaned sample displays minimal bundling effects and individual NWs can be clearly distinguished which shows that the HF acid treatment improves the morphology of the grown Si NWs.

Such an observation clearly shows that the removal of the residual $POCl_3$ is indeed a necessary step to improve the overall morphology of the Si NWs. Chen et al. [3.16], demonstrated in their work that using $POCl_3$ during doping results in the formation of P_2O_5 which comes into contact with the native SiO_2 layer on the as grown Si NWs and react at elevated temperatures to form a phosphosilicate glass (PSG) layer on the surface of the Si NWs [3.16]. Removal of this PSG layer requires simple etching of the sample in dilute HF acid as evident in the difference between figure 3.2 (a) and (b). The presence of the PSG layer on the uncleaned sample (figure 3.2(c)) is exhibited by the bundling of the NWs and the smooth surface of the grown NWs. In comparison, the HF treated sample (figure 3.2(d)) with the PSG layer removed yields well defined Si NWs with minimal bundling and rougher surface due to the etching effect. Furthermore, the bending of NWs observed on samples can also be attributed to the etching effect of the samples yielding less rigid Si NWs that can be easily sonicated and isolated from the substrate for further chemical analysis with specialized techniques as individual NWs.

3.3.2. Advanced elemental characterization of Si NWs

To ascertain the individual chemical composition of the grown Si NWs, advanced characterization techniques such as the low kV window-less EDS analysis in the SEM was conducted. This technique allows ultra-high resolution EDS X-ray mapping at a low 3 kV which reduces: sample degradation, charging during analysis and the electron beam-sample interaction volume. These result in, higher spatial resolution elemental images within a SEM compared to traditional X-ray mapping at higher kVs.

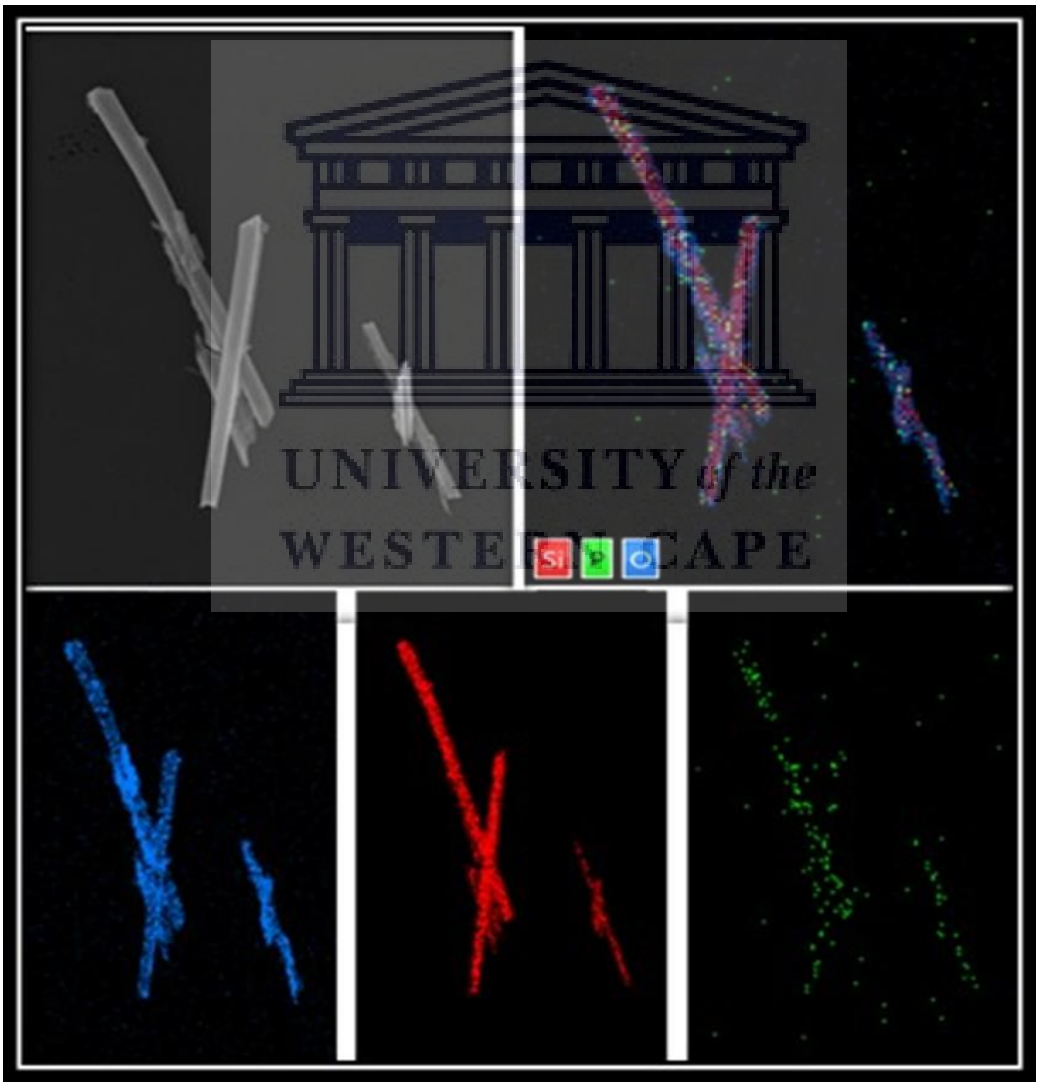

Figure 3.3: Low kV windowless EDS maps of Si, P and O on a Si NW.

In figure 3.3, X-ray maps of the doped Si NWs are presented showing an approximate distribution of the various constituent elements on the grown NWs. The SEM micrograph in figure 3.3 shows the morphology of the Si NW that was surveyed to generate the Si (red), P (green) and the O (blue) elemental map. Clearly the Si map does confirm that the Si NW has a Si core encapsulated by an oxidised SiO_2 shell due to rapid oxidation nature of non-passivated Si when exposed to air. Interestingly, the high sensitivity nature of this technique does exhibit low dose traces of phosphorous which may be one indicator of successful doping. A complementary technique such EFTEM is necessary to confirm the observations made from this analysis.

Complementary to the positive doping results observed from low kV windowless EDS, energy filtered transmission electron microscopy (EFTEM) was conducted in order to map the distribution of the constituent chemical elements on the actual Si NW sample independent of the substrate to prove the success of the n doping process of Si NWs using P. EFTEM images showing maps of the different elements being O, P and Si are presented in figure 3.4.

The elemental maps shown in figure 3.4 present an overview TEM image of a highly porous Si NW followed by a semi-uniform oxygen (blue) distribution over the NW structure and surrounding areas which is indicative of surface oxidation which can be indicative of a porous surface. The phosphorous map (green) shows a contrast between the Si NW and the surroundings indicating high phosphorous (P) concentration and is a positive indicator for successful P-doping. Similarly, the Si map also displayed contrast indicative of high concentration of Si within the Si NW structure.

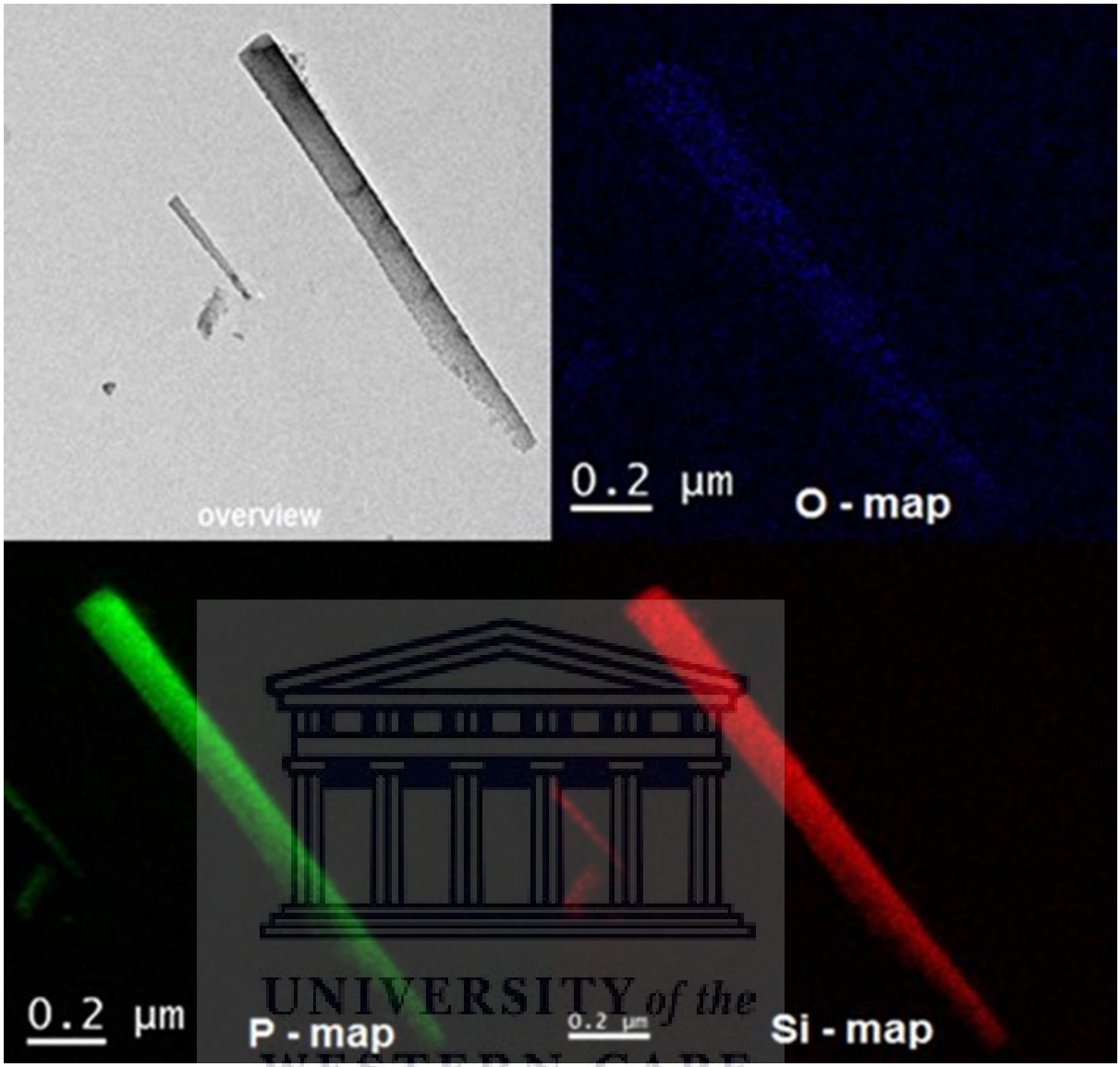

Figure 3.4: EFTEM images showing elemental maps for O, P and Si.

3.3.3. Internal and structural properties

High-resolution transmission electron microscopy (HRTEM) is a very crucial technique for conducting an in-depth analysis of the internal structure, crystallographic information and the chemical composition of the grown Si NWs. Extensive HRTEM analysis was conducted on both the intrinsic (undoped) and the phosphorous doped Si NW samples etched for 30 mins.

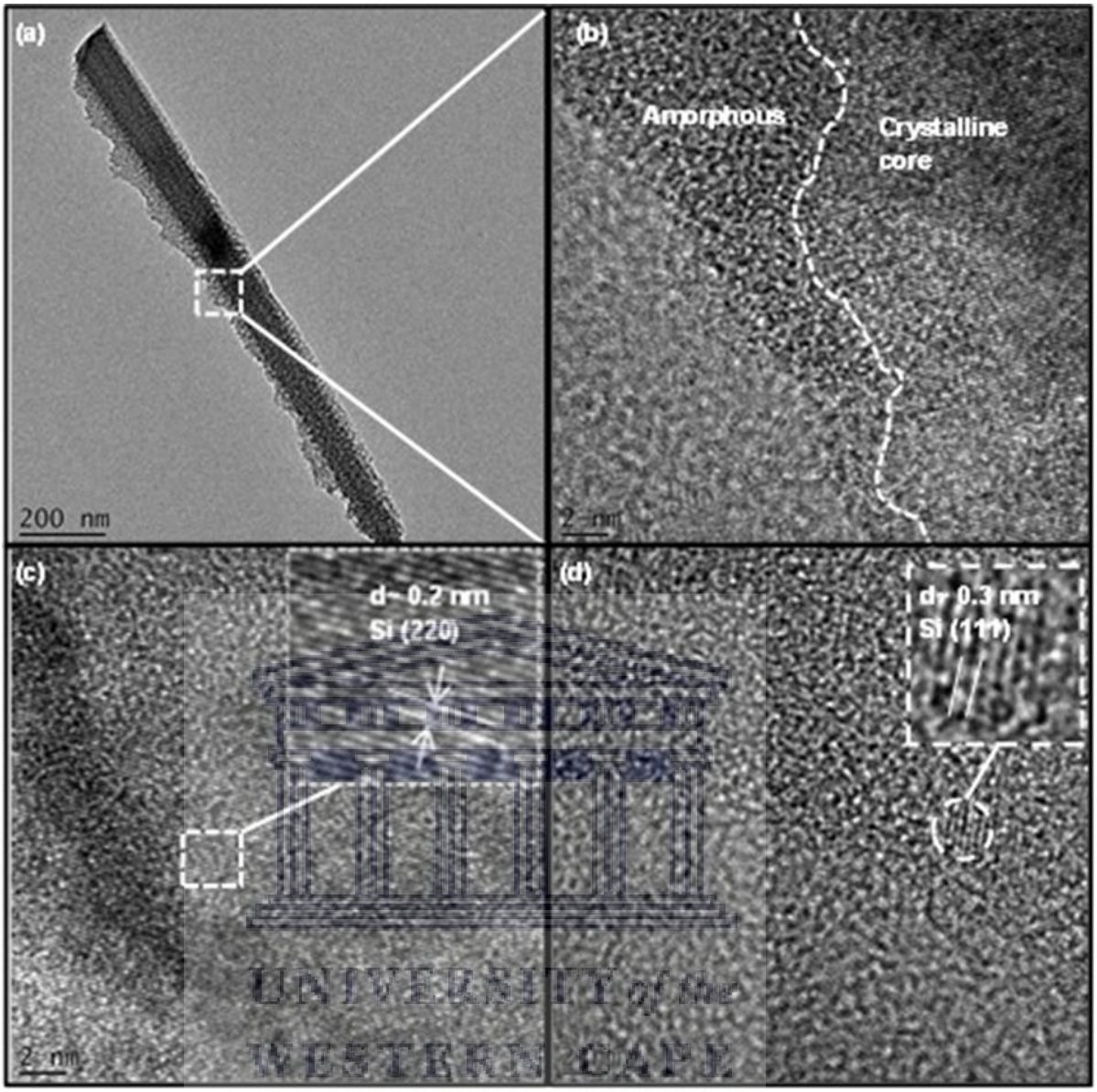

Figure 3.5: (a) Overview bright field (BF) TEM image, (b) Si NW core-shell interface, (c) Si NW crystalline core and (d) Si nano crystallite.

3.3.3.1. Intrinsic Si NWs

Figure 3.5 presents TEM and HRTEM images of an intrinsic (undoped) Si NW etched for 30 mins. In figure 3.5 (a), an overview image of a porous Si NW of about 120 nm in diameter is presented with a roughened surface and a semi-rounded tip which correlates to the observations made from SEM images (figure 3.1). A closer inspection of the image reveals that the Si NW has a core-shell structure with the core being the darker uniform region along the length of the wire encapsulated by the non-

uniform rough shell. The roughness of the surface of the Si NW can be directly linked to the morphology of the AgNPs and their minimal random lateral movements during the vertical etching process into the Si substrate [3.17].

The high-resolution (HR) TEM image presented in figure 3.5 (b) further confirms the core- shell structure of the Si NW as proposed previously in (a) with a poorly defined interfacial region marked with the dashed line. Both ordered (crystalline) and disordered (amorphous) regions make up the interfacial region which separates the crystalline core from the amorphous shell.

The observed highly crystalline core of the Si NW emanates from the crystallinity of the starting wafer while the amorphous shell is due to the incorporation of oxygen atoms in the Si lattice during surface oxidation that occurs during and post – synthesis [3.18]. The HRTEM image presented in figure 3.5 (c) shows the highly crystalline Si NW core as depicted by the well-defined lattice planes and an image inset showing a zoom in on the lattice planes with a d-spacing of about 0.2 nm which represents a Si (220) crystal orientation.

Figure 3.5 (d) presents a HRTEM image that shows an arbitrarily shaped Si nanocrystal of about 3 nm in diameter and is embedded in an amorphous matrix. Further analysis of the crystalline region shows that the lattice spacing is about 0.29 nm and corresponds to a Si (111) lattice structure under compressive strain. The formation of such strained Si NCs can be attributed to the formation of small pores around crystalline regions during the anisotropic etching of the Si NW walls. The process of pore formation in Si NWs has been discussed extensively by Hochbaum et al. [3.19], whereby the crystal defects and impurities such as dopants on the Si NW wall become the nucleation sites for the pores. Furthermore, in the case of higher

H_2O_2 concentrations during etching, some of the Ag^+ (ions) cannot be recovered back into the initial Ag particles leaving them to attack the nucleation sites after which they can diffuse out through the sidewalls of the Si NWs, hence the formation of arbitrarily shaped Si NCs on the shell of the NW [3.20].

As indicated earlier, HRTEM is one of the techniques that are used to probe internal and crystallographic properties of Si NWs, however one of the limitations of this technique is confinement into small parts of the sample. Grazing incidence x-ray diffraction was then further used to confirm the bulk crystalline properties of the as grown Si NWs as presented in figure 3.6. The XRD pattern shown in figure 3.6 confirms the presence of multi crystalline undoped Si NWs whereby the first peak at about 28.4° indicates the presence of Si (111) oriented planes while the second peak at 47° emanates from the Si (220) crystal planes, as established from the HRTEM imaging (ICDD 04-006-2527). The peaks at 56° and 76° can be attributed to the Si (311) and (331) orientations, respectively [3.21]. These XRD measurements were conducted at grazing incidence to minimise the substrate influence on the results hence the absence of the Si (400) peak at 69°. The formation of polycrystalline Si NWs as evidenced by the multiple peaks on the XRD profile is a direct result of porosity which leads to formation of Si NCs of different orientations as confirmed by HRTEM results in figure 3.5.

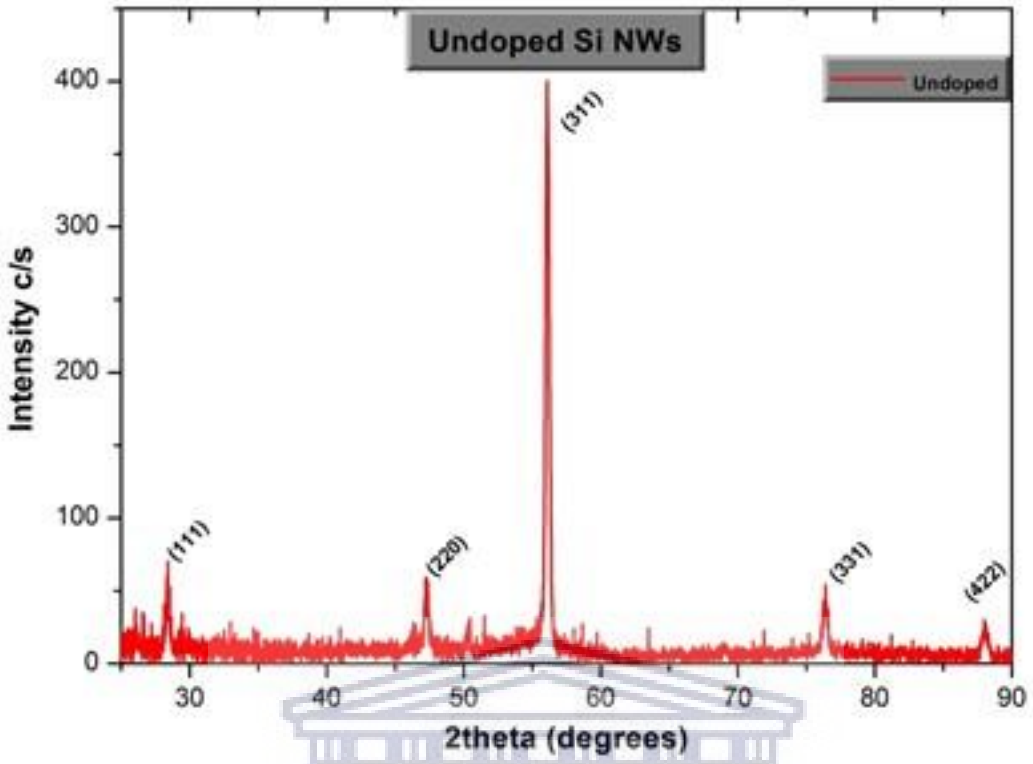

Figure 3.6: XRD pattern of undoped MACE Si NWs.

3.3.3.2. Doped Si NWs

The HRTEM analysis of the doping effects on the grown Si NWs was conducted on the sample etched for 30 mins which was further doped by spin coating $POCl_3$ and annealing at 900 ◦C for 20 minutes and lastly treated in HF acid to remove remnant phosphorous on the surface.

Figure 3.7 (a) presents an overview image of a straight and doped Si NW with a diameter of about 100 nm and highly porous tapered tip. The straight morphology of the Si NW correlates with observations made during SEM analysis as shown in figure 3.2. As indicated earlier, the straightness of the Si NW results from the preferred etching direction of the Si (100) wafer being along the <100> direction normal to the surface of the Si wafer and the suppression of lateral movement of the interlinked thin film of Ag NPs [3.7] as shown in figure 3.2 (a). Furthermore, the insert in figure 3.7 (a)

shows a highly porous Si NW tip that has been etched off to result in a slightly tapered tip and this effect is due to the extended durations of lateral etching by redeposited Ag nuclei on the Si NW tip.

Further morphological analysis shows that the doped Si NW consists of a thin, rough shell covering the core of the Si NW and random dark spots (circled in white) on the surface representing different structural features to that of the shell as shown in figure 3.7 (b). The roughening of the surface of MACE Si NWs is not a property unique to the doped sample since it was also observed for the intrinsic sample (figure 3.5 (a)) hence it can be treated as an artefact of the MACE growth mechanism of Si NWs. The roughness of the Si NWs can therefore be a direct consequence of Ag+ nucleation [3.7] on the walls of existing NWs resulting in minute lateral etching leaving the walls with a rough, uneven surface.

HRTEM of the doped sample was used to confirm that the random dark spots on the surface of the Si NW (figure 3.7 (b)) are small, confined regions of crystallinity embedded in the disordered outer shell amorphous matrix encapsulating the crystalline core of the Si NW as observed in figure 3.7 (c). The inset image in figure 3.7 (c) shows a zoomed in image of the crystalline core with lattice spacing of about 0.19 nm corresponding to Si (220) and an arbitrarily shaped Si nanocrystal (NC) with a diameter of about 2 nm. The formation of such Si nanocrystals can be linked to the porous nature of MACE Si NWs whereby pore formation leads to the formation of smaller islands of crystalline regions. When the Ag^{+} induce hole (h^{+}) injections on the surface of the NW wall into lattice defects and dopant sites, lateral etching on the NW surface occurs and the formed pores give rise to the formation of Si NCs [3.22].

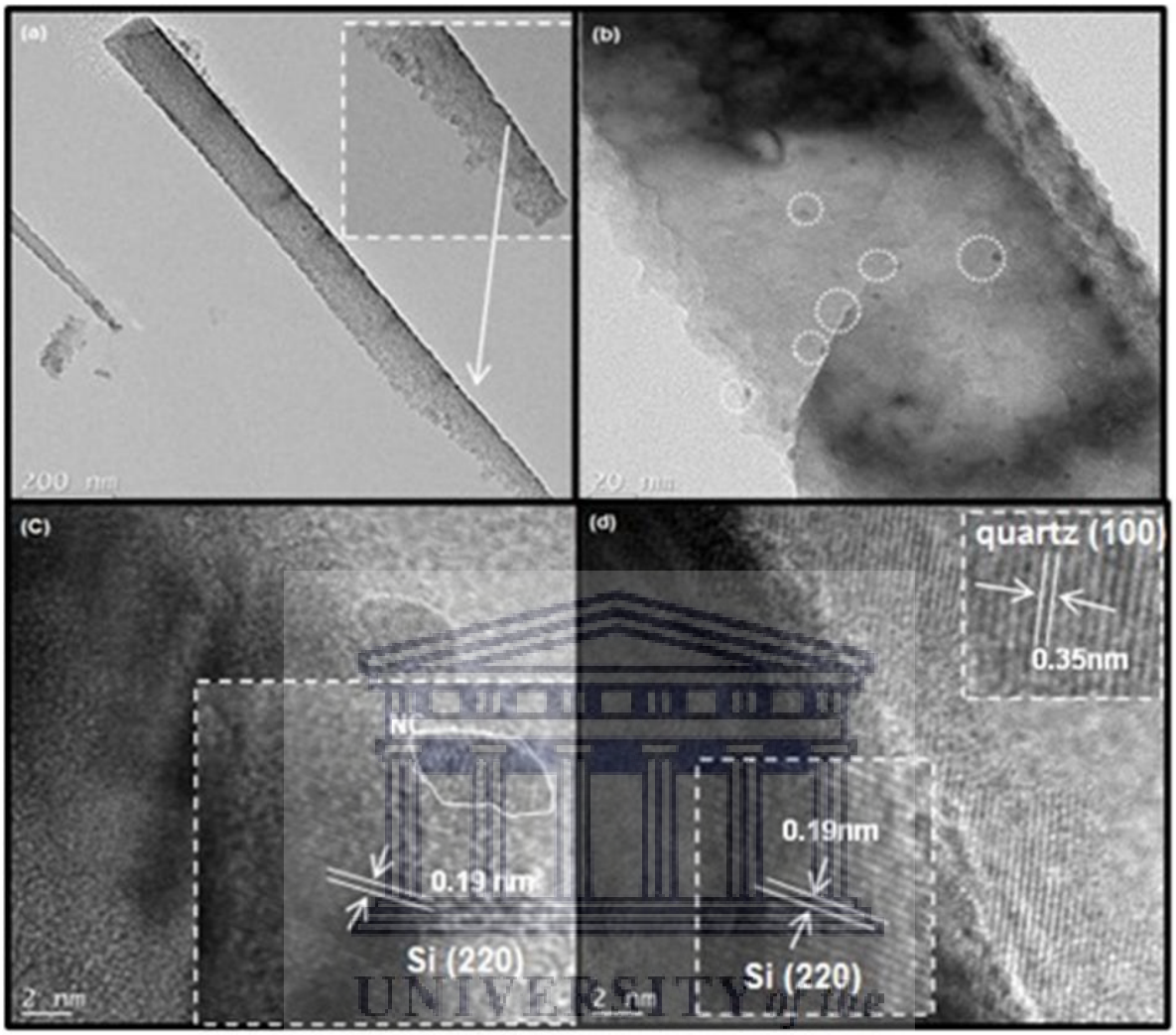

Figure 3.7: TEM images of a doped Si NW whereby (a) overview of Si NW (b) morphology of walls (c) core and shell structure with nanocrystals (d) mixed crystallinity of core and shell.

In figure 3.7 (d), an HRTEM image showing different regions of mixed crystallinity between the inner core and the outer shell of the Si NW. The inserts in figure 3.7 (d) show that the lattice spacing for the crystalline core and shell was 0.19 nm and 0.35 nm which correspond to Si (220) and c-SiO_2 (quartz (100)) respectively. The crystallographic evolution of the core of the Si NW from the starting Si (100) can be influenced by the MACE etching process and etchant concentration effect as highlighted in section 2.3.1. Furthermore, the formation of the outer crystalline SiO_2

layer can be a result of thermal induced crystallization of the oxidized Si (SiO_x) shell during doping [3.23], whereby the sample was annealed at higher temperatures of about 900℃ for 20 minutes. Closer inspection of the crystalline core showed a gradual increase in lattice spacing when measuring from the centre towards the crystallized outer regions which further confirms the mixed crystallinity and is a result of crystal defects caused by porosity and tensile stress.

XRD analysis of the doped Si NWs was employed to further confirm the crystallographic observations made in HRTEM. The XRD pattern presented in figure 3.8 shows the dominant Si (111) peak at about 28.4°, Si (220) peak at about 47°, Si (311) at about 56.2°, a weak Si (400) peak at 69° and a Si (422) peak at 88° [3.21].

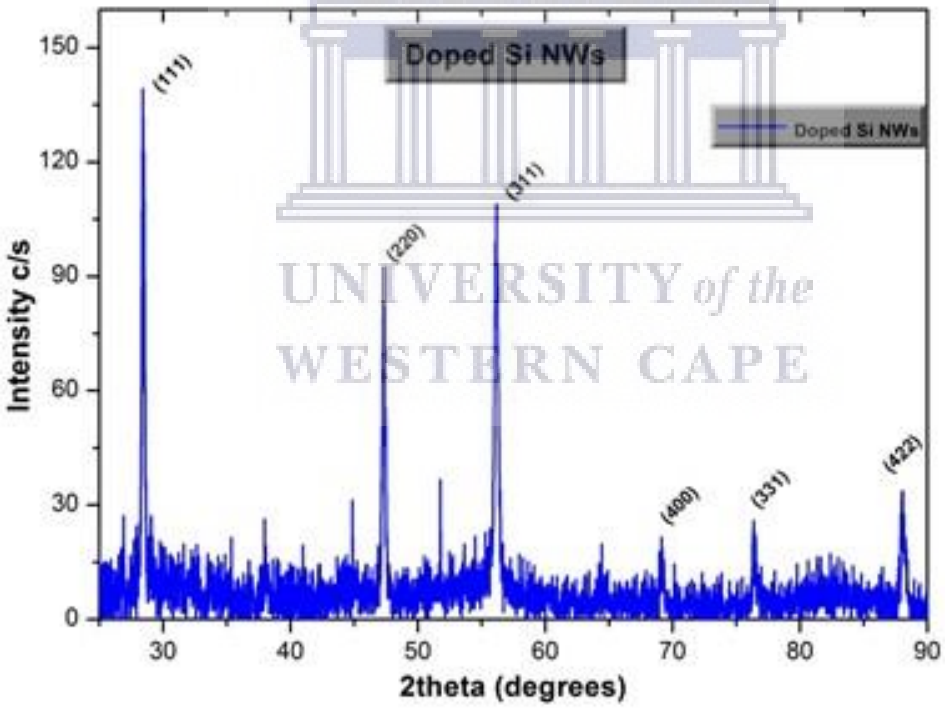

Figure 3.8: XRD pattern of doped Si NWs showing the multi-crystalline nature of etched Si NWs.

From the XRD results presented in figure 3.8, the poly-crystallinity of the etched and thermally doped Si NWs can be confirmed. In comparison to undoped Si NWs, no peak-shift is observed from the common peaks except that, the XRD profile of the

doped Si NWs shows a weak Si (400) peak at 69º. These results give an average crystalline composition of the whole sample unlike the HRTEM results based on an individual NW. The different XRD profiles observed between the doped and undoped Si NWs can be a result of solid-state recrystallization induced by the thermal treatment of Si which provides energy for the rearrangement and ordering of Si grains to form new crystallites. Furthermore, the presence of impurities such as phosphorous (P) during thermal doping has also been found to enhance the thermal crystallization of amorphous Si.

The investigation of structural properties has revealed the presence of structural artefacts within the Si NWs such as pores, Si NCs and multi layered core-shell structure. These artefacts have been found to have an influence on other Si NW properties such as the optical response of the NWs which deviate from the known bulk properties due to the size range of these observed features.

3.3.4. Optical properties of MACE Si NWs

3.3.4.1. Photoluminescence in Si NWs

Despite the indirect bandgap of bulk Si, several morphologies of Si nanostructures such as Si NWs, Si NCs and p-Si have been found to exhibit astounding light emitting properties at room temperature. The peak position, intensity, decay-time are highly dependent on surface factors such as the doping level, porosity and dangling bonds. HRTEM analysis of the Si NWs in figure 3.5 showed that the as-grown Si NWs constitute of a crystalline core with defects and a porous, amorphous SiO_x shell that has NCs embedded in it, these features have been found to have a strong influence on the PL character of MACE Si NWs [3.24].

The photoluminescence spectra shown in Figure 3.9 (a) represents the PL emission obtained from undoped, intrinsic Si NWs etched for the different times (5, 10, 20 and 30 min) whereby normalized intensity is plotted against the wavelength to prevent attenuation of signals with lower intensity. These PL spectra are characterised by one broad symmetric emission band stretching from about 550 to 800 nm. This broad peak is composed of two intense overlapping peaks centred at about 650 and 690 nm. The origin of these two peaks can be attributed to a combination of both quantum confinement in Si NCs and the surface oxidation interfacial states [3.25] while the broadness of the emission peaks is indicative of the crystallite size variation responsible for the emission at different wavelengths. Closer inspection of the different spectra reveals a slight shift of peaks towards lower wavelength as the etching time (length of Si NWs) increases. This observed shift can be attributed to the increased porosity of the NWs etched for a longer time which in-turn leads to the size reduction of Si NCs embedded in the amorphous matrix hence the shift in emission band.

The PL spectra presented in figure 3.9 (b) show the emission characteristics of doped Si NWs within the 400-800 nm wavelength range. These spectra are characterised by two main features being a strong emission band at about 400-500 nm and a weaker emission band between 700-750 nm. The 400-500 nm emission band is composed of two adjacent, overlapping peaks centred at about 419 and 441 nm with the latter having higher PL intensity and an asymmetric tail towards higher wavelengths.

Similarly, the 700-750 nm emission band consists of two overlapping asymmetric peaks centred at about 720 and 731 nm. In correlation with SEM observations made in figure 3.1, it can be observed that the PL peak position has no link with the length of the Si NWs nor their diameter since the peak maximum are at about the same

wavelength. These observations further strengthen the proposition that the origin of this visible PL may not be due to recombination within the Si NWs due to their indirect bandgap and diameters being larger than the exciton Bohr diameter in Si hence the quantum confinement (QC) effects [3.24] observed can be originating from other structural artefacts like Si NCs as observed in HRTEM.

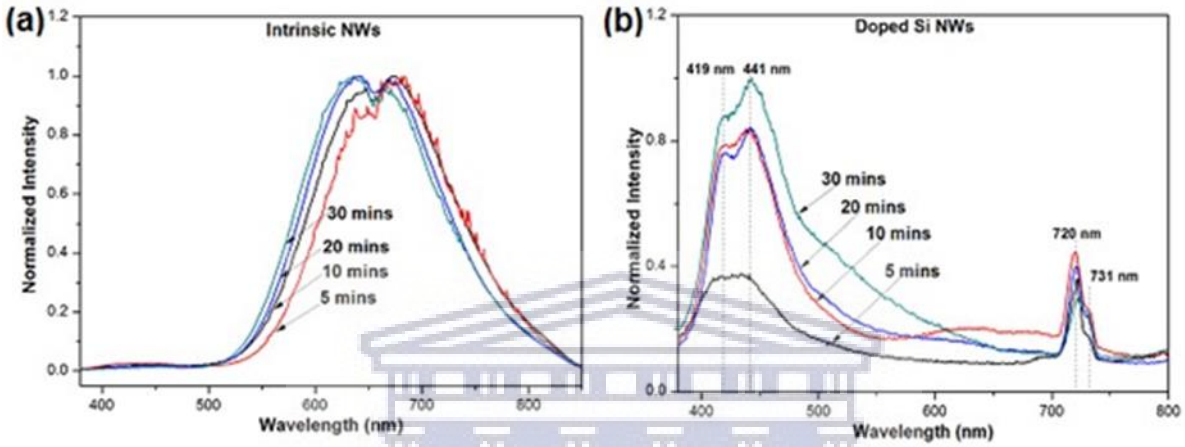

Figure 3.9: PL spectra of (a) intrinsic/undoped Si NWs and (b) doped Si NWs etched for 5, 10, 20 and 30 minutes.

Figure 3.10 (a) shows the deconvolution of the emission band of the 30 minutes etch and doped sample, revealing a small peak A at about 419 nm followed by a more intense peak B at 441 nm and a broad peak C at about 492 nm which is responsible for the asymmetric shape of the emission the band. Deconvolution of the 700-750 nm emission in figure 3.10 (b) results in a broad weak peak D at about 721 nm and peak E at about 732 nm.

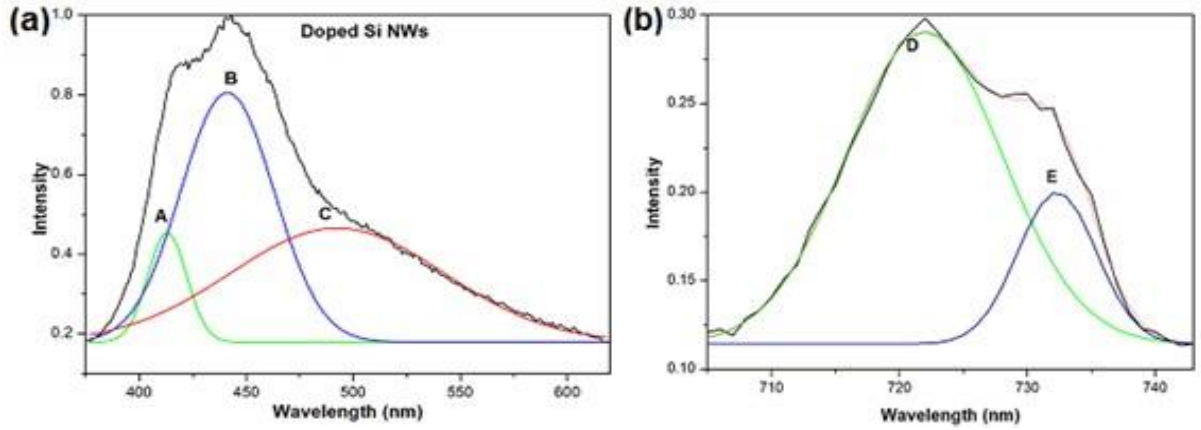

Figure 3.10: Deconvolution of the PL spectrum for doped Si NWs (a) 400-500 nm (b) 700-745 nm emission bands.

The origin of peak A can be directly linked to the presence of smaller heavily doped Si NCs as observed in the HRTEM analysis in figure 3.5 (c) with NC sizes of about 2 nm. The doping of Si NCs results in further transformation of the NC bandgap through introduction of defect states and thermal treatment. Based on the quantum confinement model [3.23], a decrease in crystallite size results in a lower wavelength-shift of the peak maximum and increased probability of electron-hole recombination due to exciton confinement. However, as observed in peak A, this high recombination probability does not translate to enhanced PL intensity due to the reduced absorption cross-section and crystal density as seen in HRTEM figure 3.7.

The higher intensity emission peak B (441 nm) can be ascribed to the neutral oxygen defect states or vacancies (=Si-Si=) found in the crystallized SiO_2 NCs and acting as electron-hole pair recombination centres [3.26]. The broad band observed at about 492 nm (peak C) can be attributed to the growth of an interfacial SiO_x layer on the surface surrounding or coating the Si NWs or Si NCs [3.27]. Figure 3.10 (b) shows the red-orange PL emission band characterised by peak D and peak E at 721 nm and 732 nm respectively. In most cases, this observed emission can be linked with the surface morphology of the Si NWs [3.24] whereby the rough, NC-coated and p-Si

NW consists of a two-phase oxide coating as revealed by HRTEM analysis with a thin amorphous SiO_x interfacial layer and amorphous SiO_2 outer layer. These two layers then act as radiative recombination centres for excitons with the SiO_x corresponding to peak D and the silicon hydrides (SiH_x) from the HF terminated surface resulting in the emission at 732 nm (peak E) [3.28]. In other works, the luminescence of porous Si has been attributed to localization of carriers at surface states and extrinsic centres leading to formation of recombination centres or the quantum confinement of excitons in the Si nano crystallites as observed in these samples. The observed reduction in PL intensity can be associated with the reduction of the thickness of the amorphous SiO_x shell during the HF treatment of Si NWs as observed in HRTEM.

3.3.4.2. UV-Vis optical reflectivity of Si NWs

In order to understand the optical response of Si NWs, optical reflectivity properties of the grown Si NWs were investigated using UV-Vis specular reflection. Generally, it has been demonstrated that vertical Si NW arrays produced during MACE can be used as antireflective coatings to enhance the light absorption and performance of solar cells [3.29, 3.30]. The UV-Vis spectra showing the enhanced anti-reflectivity of MACE etched Si NWs are shown in figure 3.11.

The bare Si wafer reflectivity spectra shown in figure 3.11 shows high reflectivity in the UV region between 60-80% which later decreases to about 40% in the visible region while the Si NWs show very low reflectivity below 2%. The two characteristic peaks observed at about 274 and 368 nm, typical of c-Si can be attributed to optical transitions near the band gap of Si [3.31].

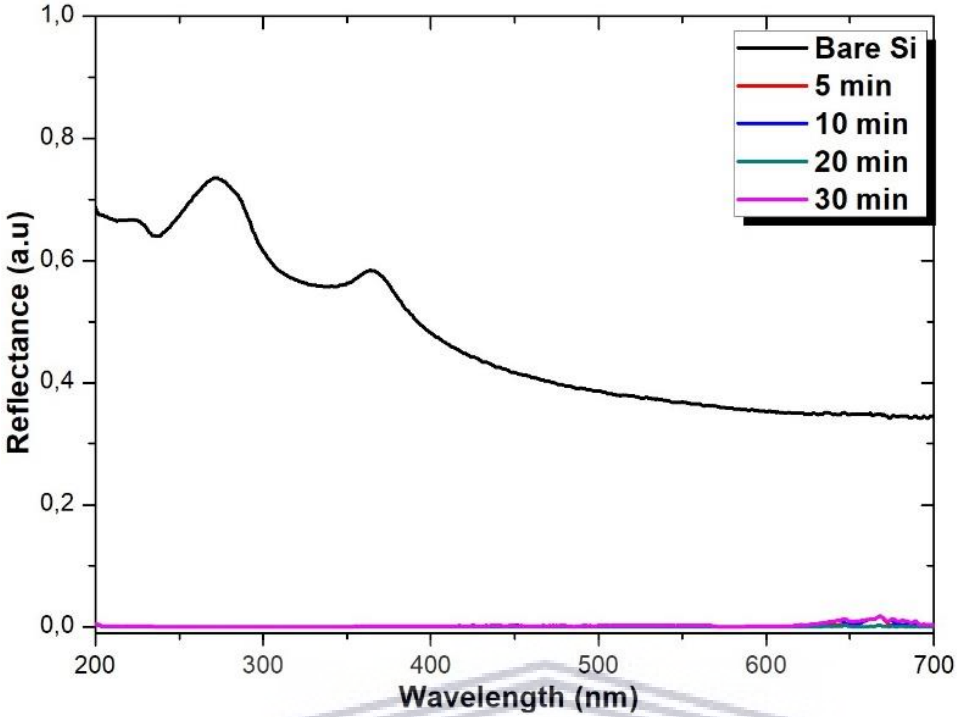

Figure 3.11: Reflectivity spectra of (a) Si wafer vs Si NWs.

Furthermore, figure 3.11 shows that the Si NWs of different lengths and etching times exhibit very low reflectance percentage below 1% in the UV region and slightly increases to about 2% at higher wavelengths.

In comparison to bare Si wafers, vertical Si NW arrays can achieve drastically attenuated optical reflectivity in two ways. Firstly, enhanced optical trapping is observed when incident light gets trapped between closely packed vertical Si NWs hence reducing the reflected light drastically [3.32]. Secondly, the porosity of Si NWs ensures that the mismatch between the refraction index of the Si NWs and air is greatly reduced compared to that of bare Si wafer [3.29]. HRTEM investigations conducted previously show that the synthesized Si NWs have a highly porous tip with a semi-tapered structure which is ideal for antireflective coatings since it reduces the amount of Si interacting with air. The high porosity of the Si NWs can result to a decrease in the refractive index and enhance roughness of Si NWs which promotes scattering of

light hence the reduced reflectivity below 1% [3.29]. From these results it can be established that even the shortest Si NWs (5 minutes) exhibit very good UV-Vis absorption.

3.3.5. Electron transport in Si NWs

HRTEM and EFTEM investigations conducted on the doped Si NWs have confirmed the presence of phosphorous (n-dopant) on the grown structures. However, these measurement techniques lack the sufficient sensitivity to distinguish whether its surface phosphorous atoms on the NWs or phosphorous embedded in the NW structure as n-dopant. Furthermore, these techniques lacked the ability to quantify the dopant levels of such dopants on the different Si NW samples hence the need to employ hall-effect measurements on the samples. Van der Pauw Hall-effect measurements were conducted to establish the overall I-V and other electronic transport properties of the samples.

In these measurements, current was applied to the sample and resultant voltage was measured and used to obtain other parameters such as the mobility, conductivity, resistivity and dopant levels of the different samples. Table 3.1 presents a summary of the electronic properties of the different samples.

Table 3.1 Electronic properties of n-doped Si NWs from different etching times

Etching time [min]	Bulk Conc. x10^{17} [cm^{-3}]	Mobility [cm^2/Vs]	Resistivity x10^{-2} [Ω.cm]	Conductivity [Ω.cm]$^{-1}$	Sheet Conc. x10^{14} [cm^{-2}]
5	-64.85	51.29	1.88	53.28	-6.44
10	-15.96	61.14	6.40	15.63	-2.87
20	-10.79	41.11	4.08	7.10	-2.69
30	-48.68	34.88	3.68	27.20	-18.5

From the summary of electronic properties shown in table 3.1, it is evident that the shortest (5 min) Si NW sample had the highest doping level followed by the longest (30 min) NW sample while the 10 minutes sample had the third highest bulk concentration and the 20 min Si NW sample having the lowest dopant levels. This observation shows that there was no direct relation between the length of the Si NW and the dopant variation between the samples. The electron mobility was found to decrease with increasing Si NW length and not dependent on bulk concentration as observed in bulk Si. This observed anomaly can also be attributed to other morphological artefacts of the samples such as; the varying Si NW diameters, the high porosity and varying defect densities which create electron traps and enhance scattering thus reducing mobility [3.12], [3.33], as observed from HRTEM.

The resistivity of the samples exhibited an inverse relation to the dopant concentration with resistivity increasing from 0.0188 to 0.0408 Ω.cm while conductivity displayed a direct relation to concentration. These relatively high resistivity values can be attributed to the highly porous nature of MACE Si NWs as shown by HRTEM investigations. The porous structure can result in the narrowing of the electron transport channel, trapping and scattering of electrons from the pores [3.33]. Furthermore, it can be established that the higher resistivity's are a result of lower dopant levels in some of the samples which can in turn result in higher contact and intrinsic resistances of the Si NWs [3.33].

3.3.6. Chemical surface analysis of MACE Si NWs

The growth and doping of MACE Si NWs were successfully achieved as depicted by hall-effect measurements which prove the success of the n type doping electronically. However, detailed and quantitative chemical analysis of the samples is crucial to enhance the understanding of the bonding configurations in doped Si

nanostructures and this was achieved by using X-ray photoelectron spectroscopy with depth profiling. To generate the data, high-resolution scans on the Si 2p bond were conducted to reveal the constituent Si types and further ascertain doping success is graphically shown in figure 3.12 with the summary of the peak information is presented in table 3.2.

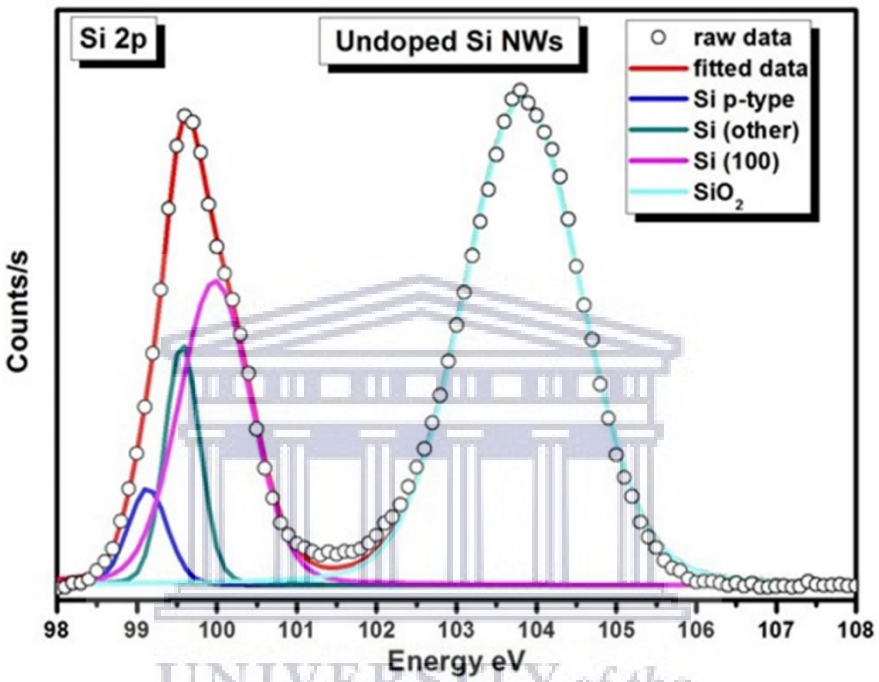

Figure 3.12: Si 2p bond information showing the Si p-type, Si (100) and Si (other) peaks.

From the as-grown and undoped Si NW spectra presented in figure 3.12, it can be confirmed that the Si (100) substrate used for the MACE is indeed lightly p doped by the presence of the Si (p type) peak centroid at about 99.15 eV. The second peak centred at about 99.57 eV can be attributed to other types of Si configurations present in the grown Si NWs [3.34]. This observation complements the HRTEM and GIXRD results which confirmed the multi-crystalline nature of these nanostructured Si materials. The Si (100) peak observed at 99.7 eV [3.34] does confirm the nature and configuration of the Si substrate used for etching. The surface oxidation as observed

in HRTEM can be further substantiated by the presence of the SiO_2 large peak at about 103.8 eV as evidenced by the large peak area %.

Table 3.2: XPS bond Peak summary for undoped Si NWs

Bond Type	Peak BE (eV)	FWHM (eV)	Peak Area %
Si (p-type)	99.15	0.58	4.22
Si (other)	99.57	0.51	9.28
Si (100)	99.75	1.06	24.10
SiO_2	103.82	1.73	62.39

The n doped Si NW spectra shown in figure 3.13 demonstrates that the doping process was a success as indicated by the presence of the Si p type and n type 2p peaks at around 99.25 and 100.2 eV, respectively.

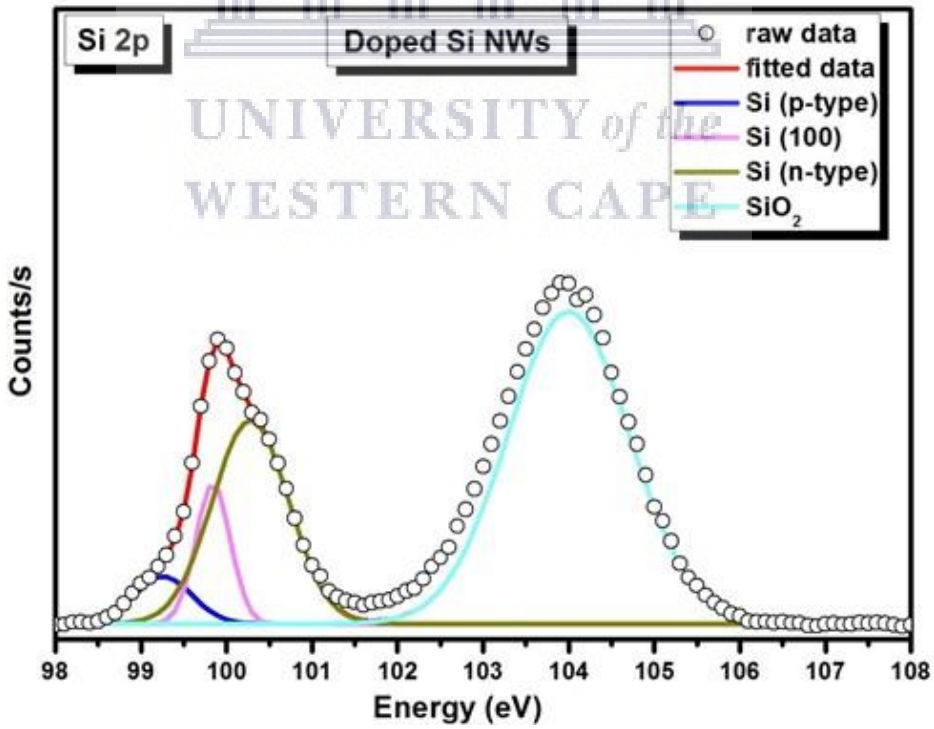

Figure 3.13: Si 2p bond information of doped Si NWs showing the Si p type, Si (100) and Si n type peaks.

Furthermore, as shown in table 3.3, the higher peak % area of the n type bond compared to the p type bond does indicate higher phosphorous dopant concentrations at the surface of the samples which are evidence of the p and n type Si species observed in hall-effect measurements.

Table 3.3: Peak information summary for n-doped Si NWs.

Bond Type	Peak BE (eV)	FWHM (eV)	Peak Area %
Si (p-type)	99.26	0.79	4.44
Si (100)	99.84	0.47	7.90
Si (n-type)	100.27	1.05	25.42
SiO_2	103.99	1.67	64.14

Based on these XPS measurements conducted on undoped and doped Si NWs, it can be confidently concluded that the MACE Si NWs were successfully n doped as supported by other techniques and the higher integrated area of the n type peak in comparison to the p type peak at the sample surface and shallow depths. The peak broadening observed can be attributed to bond variation and changes due to thermal doping and other structural defects as observed in HRTEM.

3.4. Conclusion

Si NWs were successfully prepared using the MACE method at different etching durations which resulted in Si NWs with lengths ranging from about 1 – 4 μm and a diameter range of about 80 – 200 nm. SEM analysis showed that longer etching times resulted in longer, rougher and less rigid Si NWs characterised by slight bending at the tips. HRTEM investigations of the internal structure of the Si NWs revealed a core-shell structure of the fabricated Si NWs whereby the core is crystalline encapsulated

by a highly porous amorphous shell. Further analysis revealed small islands of Si NCs embedded in the amorphous matrix and these structures consequently resulted in the PL emission observed from the Si NWs. The grown Si NWs were found to display high UV-Vis antireflective properties making them ideal for solar cell applications. Hall-effect measurements confirmed a successful n doping process of the Si NWs with no direct relation between the NW length and dopant level. Higher electron mobility was observed from Si NWs with low dopant levels as per the behaviour of bulk Si. However, the slight discrepancies observed in other samples was attributed to morphological properties such as high porosity of the structures resulting in electron traps. XPS surface analysis of doped Si NWs showed the presence of Si n type bonds which confirmed successful doping of Si NWs.

References

[3.1] S. Li, W. Ma, Y. Zhou, X. Chen, Y. Xiao, M. Ma, W. Zhu. F. Wei, Nanoscale Res. Lett. 9(1), (2014) 196.

[3.2] M. Ramesh, H. S. Nagaraja, Mater. Charact. 129, (2017) 24 – 30.

[3.3] Z. G. Huang, X. X. Lin, Y. Zeng, S. H. Zhong, X. M. Song, C. Liu, X. Yuan, W. Z. Shen, Sol. Energy Mater Sol. Cells. 143, (2015) 302 – 310.

[3.4] S. K. Srivastava, D. Kumar, P. K. Singh, M. Kar, V. Kumar, M. Husain, Sol. Energy Mater Sol. Cells. 94, (2010) 1506 – 1511.

[3.5] Y. Hung, S. Leee, K. Wu, Y. Tai, Y. Pan, J. Opt. Soc. Am. 19(17), (2011).

[3.6] J. Davenas, S. B. Dkhil, D. Cornu, A. Rybak, Energy Procedia. 31, (2012) 136 - 143.

[3.7] Z. Huang, N. Geyer, P. Werner, J. de Boor, U. Gösele, Adv. Mater. 23, (2011) 285 – 308.

[3.8] R. Ghosh, P. K. Giri, K. Imakita, M. Fujii, Nanotechnology. 25, (2014) 045703.

[3.9] L. A. Osminkina, K. A. Gonchar, V. S. Marshov, K. V. Bunkov, D. V. Petrov, L. A. Golovan, F. Talkenberg, V. A. Sivakov, V. Y. Timonsheko, Nanoscale Res. Lett. 7(524), (2012).

[3.10] K. A. Gonchar, A. A. Zubairova, A. Schleusener, L. A. Osminkina, V. Sivakov, Nanoscale Res. Lett. 11(357), (2016).

[3.11] Y. Qi, Z. Wang, M. Zhang, X. Wang, A. Ji, F. Yang, AIP Adv. 4(031307), (2014).

[3.12] Y. Cui, X. Duan, J. Hu, C. M. Lieber, J. Phys. Chem. B. 104(22), (2000).

[3.13] M. Li, Y. Li, W. Liu, L. Yue, R. Li, Y. Luo, M. Trevor, B. Jiang, F. Bai, P. Fu, Y. Zhao, C. Shen, J. Mbengue, Mater. Res. Bull. 76, (2016) 436 – 449.

[3.14] C. Zhang, C. Li, Z. Liu, J. Zheng, C. Xue, Y. Zuo, B. Cheng, Q. Wang, Nanoscale Res. Lett. 8(277), (2013).

[3.15] X. Li, Curr. Opin. Solid State Mater. Sci. (2012).

[3.16] R. Chen, H. Wagner, A. Dastgheib-Shirazi, M. Kessler, Z. Zhu, V. Shutthanandan, P. Altermatt, S. Dunham, J. Appl. Phys. 112(124912), (2012)

[3.17] A. K. Buin, A. Verma, A. Svizhenko, M. P. Anantram, Nano Lett. 8(760), (2008)

[3.18] Y. Nakamine, T. Kodera, K. Uchida, S. Oda, Jpn. J. Appl. Phys. 50(115002), (2011).

[3.19] A. I. Houchbaum, D. Gargas, Y. J. Hwang, P. Yang. Nano Lett. 9, (2009) 3550 – 355.

[3.20] Y. Qu, H. Zhoua, X. Duan, Nanoscale. 3, (2011) 4060 – 4068.

[3.21] M.C. Steele, F.D. Rosi, , J. Appl. Phys 29 (11), (1958).

[3.22] N. Bachtouli, S. Aouida, B. Bessais, Microporous Mesoporous Mater. 187, (2014) 82 – 85

[3.23] M. Zacharias, J. Heitman, R. Scholz, U. Kahler, M. Schmidt, J. Blasing, Appl. Phys. Lett. 80(4), (2002).

[3.24] W. Chern, K. Hsu, I.S. Chun, B.P.D. Azeredo, N. Ahmed, K.H. Kim, J.M. Zuo, N. Fang, P. Ferreira, X. Li, Non-lithographic patterning

[3.25] T.Suzuki, L. Skuja, K. Kajihara, K. Hirano, T. Kamiya, H. Hosono, Phys. Rev. Lett. 90(186404), (2003).

[3.26] M. S. Dhlamini, J. J. Terblans, R. E. Kroon, O. M. Ntwaeborwa, J. M. Ngaruiya, J. R. Botha, H. C. Swart, S. Afr. J. Sci. 104, (2008).

[3.27] L. Tsybeskov, J. V Vandyshev, P. M. Fauchet, Phys. Rev. B. 49, (1994).

[3.28] P. Kumar, ISRN. ISRN. Nanotechnol. Article ID 163168, (2011).

[3.29] Z. Huang, J. Liu, JSM. Nanotechnol. Nanomed. 3(1), (2015).

[3.30] R. Benabderrahmane Zaghouani, S. Aouida, N. Bachtouli, B. Bessais, Chem. J. 1(2), (2015) 10 – 14.

[3.31] V. Y. Timosheko, K. A. Gonchar, I. V. Mirgorodosky, N. E. Maslova, V. E. Nikulin, G. K. Mussabek, Y. T. Taurbaev, E. S. Svanbayev, T. I. Taurbaev, Nanoscale Res. Lett., 6, (2011) 349

[3.32] W. K. To, J. Fu, X. Yang, V. A. Roy, Z. Huang,

[3.33] B.M. Curtin, E.A. Codecido, S.E. Kramer, J.E. Bowers, Field-effect modulation of thermoelectric

[3.34] P. S. K. J.F. Moulder, W.F. Stickle, Handbook of x-ray photoelectron spectroscopy, reissue Edition.

Chapter 4

Investigating the Effect of Silicon Nanowire Load Ratio on The P3HT:$PC_{71}BM$/Silicon Nanowire Hybrid Matrix and the Effect of Different Silicon Nanowire Dopant Levels.

Abstract

This chapter reports on the successful fabrication of photoactive inorganic/organic hybrid thin films and hybrid solar cell devices realised by incorporating n-doped Si NWs in a P3HT:PCBM matrix. The incorporation of inorganic nanostructures in organic structured materials has been found to enhance the structural and opto-electronic properties of unstable organic materials. However, investigating the impact of varying the load ratio of the inorganic species is crucial for realizing optimal performance from such hybrid structures. Furthermore, since the Si NWs are doped, it is also necessary to assess the role of different dopant levels in the performance of the hybrid structures and devices.

Upon investigating the impact of varying the amount of Si NWs in the organic matrix, surface morphology analysis using scanning electron microscopy (SEM) exhibited a nonhomogeneous thin film with evenly distributed Si NWs which form random clusters. Furthermore, high resolution transmission microscopy was employed to investigate the interfacial interaction between the Si NWs and the polymer/fullerene blend. Structural information obtained from the grazing incidence XRD (GIXRD) showed minimal peak shifting with varying Si NW ratios indicative of strain on the hybrid thin film. Chemical analysis from X-ray photoelectron spectroscopy did not show the presence of Si due to sensitivity limitations however broadening of the polymer peaks was observed. UV-Vis absorption of the hybrid thin films was found to improve with the addition of Si NWs while the photoluminescence quenching also increased due to the addition of doped Si NWs. Hall-effect measurements on the samples showed improved mobility and conductivity of the hybrid thin films.

As indicated, the impact of different dopant levels of Si NWs was investigated using a series of techniques. Morphological results show a uniform nanowire

distribution in all samples while optoelectronic measurements show an increase in PL emission with increasing dopant level and enhanced UV-Vis on the highly doped sample. Hall-effect measurements showed significant increase in conductivity with increasing dopant concentration while there was a less significant drop in carrier mobility as the dopant concentration increased. These observations correlated very well with the J-V characteristics whereby the highly doped sample yielded the highest PCE with a significant gain of over 100% compared to sample without Si NWs.

4.1 Introduction

In recent years, polymer-fullerene (organic) based solar cells have received a lot of interest from researchers resulting in tremendous growth and consequently leading to record high efficiencies of up to ~14% [4.1-3]. Furthermore, these organic based solar cells can be realised using light, low-cost, environmentally friendly and flexible materials making it possible to use a wide variety and shapes of substrates [4.4]. In organic solar cells, the photovoltaic mechanism is realised at a bulk heterojunction (BHJ) formed by the p- and n-type species whereby high exciton dissociation occurs followed by conduction of holes and electrons to electrodes [4.5].

Despite the increased efficiencies reported in other works, some of the challenges to the upscaling and commercialization organic solar cells include solar cell instability due to physical or chemical degradation resulting in a short life span [4.6]. Furthermore, the low mobility in organic thin films imposes an active layer thickness limit of a few hundred nanometres leading to non-optimal light absorption, narrow absorption bandwidth and enhances series resistance leading to reduced solar cell efficiency [4.4]. Generally, organic solar cells exhibit low short circuit current density (J_{sc}) than their inorganic counterparts due to limited conductivity of the polymer-fullerene matrix resulting in poor charge carrier transport [4.1].

Several approaches to address the challenges associated with organic solar cells have been explored such as the incorporation of various inorganic architectures to form hybrid inorganic-organic solar cells. Nanostructured materials such as silicon (Si), zinc oxide (ZnO), cadmium selenide (CdSe) and other metal oxides have been found to enhance the efficiencies up to ~11% due to the novel properties exhibited by such nanostructured materials [4.1]. Some advantages of these nanostructures include, large surface to volume ratio for enhanced exciton dissociation, direct charge

pathways and superior charge conducting properties [4.1,4.7]. Efficient charge carrier generation can be directly linked to the interfacial charge transfer rate being higher than the bound exciton recombination rate within all the possible hybrid configurations. Moreover, charge separation is highly dependent on energy band alignment at the inorganic – organic interface, while photocurrent relies mostly on the active-layer – electrode energy level alignment [4.8].

Different architectures and morphologies of metallic oxides such as ZnO nanorods (NRs), nanowires (NWs) and nano-ridges have been used successfully in hybrid solar cells as electron accepting and transporting materials. Some of the advantages of nanostructured ZnO include the high conductivity and low temperature processing which results in optimal electron pathways and easy production of ZnO nanostructures respectively. However, the surface characteristics of hydrophilic ZnO NRs can result in a distorted interfacial morphology between the ZnO and hydrophobic polymers resulting in poor conversion efficiencies [4.9].

In other works, CdSe based hybrid solar cells have also been found to display high electron mobility which results in efficient charge transport and exciton separation which supresses charge recombination hence increasing solar cell efficiency. Despite all the promising properties, nanostructured CdSe (rods, nanoparticles) is a wider band gap material which results in inefficient absorption in the visible region. Furthermore, the Cd is a toxic heavy metal while the Se can also be toxic in higher quantities [4.10,4.11] which poses as an environmental challenge and health risk for humans.

On the contrary, nanostructured Si architectures such as Si NWs and NRs have been successfully incorporated in hybrid solar cells resulting in enhanced solar cell properties and conversion efficiencies [4.4]. The tunability of Si NWs renders them as

most ideal materials for enhanced light trapping and a broader solar cell absorption spectrum from UV to NIR unlike the optically transparent ZnO NWs [4.12]. Furthermore, doped Si NWs have been demonstrated to exhibit very high conductivities approaching the metallic limit depending on their dopant levels [4.13]. The larger surface to volume ratio of Si NWs results in enhanced charge separation due the increased surface area of the BHJ. The robust and stable 1-dimensional structure of Si NWs implies a stable solar cell that has a longer life span with enhanced mobility and conductivity resulting in higher efficiencies.

Inorganic nanostructures such as Si NWs have been found to possess extraordinary optical and electronic properties [4.14] which may be effectively transferred into the hybrid matrix resulting in even more stable hybrid solar cells [4.15]. However, in the process of mixing these different types of materials, it is very crucial to be conscious of the thresholds necessary for maintaining optimal performance of such hybrid architectures. Therefore, in this work a study to investigate the impact of different amounts of Si NWs loaded to form a hybrid structure is investigated. Furthermore, Si NWs of different; morphology, composition, dopant concentrations exhibit different optical and electronic properties which in turn offers a wider tuning scope when integrated in a hybrid matrix. More specifically, varying dopant concentrations in Si NWs influences the charge carrier concentration which has a direct impact in the performance of hybrid SC`s [4.16-18] hence the need to investigate the impact of different dopant levels.

4.2 Experimental Setup

4.2.1 Sample preparation

N doped Si NWs produced using the MACE method (detailed in chapter 3) and suspended in a dichlorobenzene mixture were used in this work. The polymer blend was prepared by mixing commercial P3HT (Sigma Aldrich) and $PC_{71}BM$ at the ratio of 1:0.6 wt% and dissolving the mixture in DCB and stirring for 24 hours at room temperature to form a smooth and homogeneous blend. The uniformly doped Si NW and DCB suspension was achieved through a series of ultrasonication processes. To investigate the load ratio effect, different mixtures were then prepared by mixing Blend to Si NWs at different volume ratios of 1:0, 1:0.5, 1:1, 1:2 and stirring them for 2 hours to mix evenly.

Similarly, to investigate the impact of different Si NW dopant levels on hybrid thin films, as-grown Si NWs were post-doped for 20 minutes at different temperatures of 700, 800 and 900℃ referred to as being low, mildly and highly doped respectively. These doped Si NWs were also ultra-sonicated and suspended in a dichlorobenzene (DCB) in preparation for mixing with polymer blend. As indicated previously, the polymer blend was prepared by mixing commercial P3HT (Sigma Aldrich) and $PC_{71}BM$ at the ratio of 1:0.6 wt% and dissolving the mixture in DCB and stirring for 24 hours at room temperature. The different mixtures were then prepared by mixing Blend:Si NWs at the same volume ratio of 1:1 which was found to be ideal ratio for high performance and stirring them for 2 hours to mix evenly.

Cleaning of the indium tin oxide (ITO) substrates was conducted through a two-step sonication process in helmanex and isopropyl alcohol for 15 minutes in each solution and a double rinse in deionized water after each cleaning step. The cleaned substrates were then dried using inert gas. To prepare the thin films, PEDOT: PSS

(Sigma-Aldrich) was spin coated on the ITO at 5000 rpm for 30 s and dried on a top pan heater for 5 minutes. The active layer was then spin coated at 900 rpm for 90 s and then heated at about 150℃ for 15 minutes.

4.2.2 Sample characterization

SEM was conducted using a Zeiss Leo 1525 field emission scanning electron microscope (FESEM) operated at low voltages of about 5 kV. Advanced low kV windowless SEM EDS analysis was con- ducted using an OXFORD X-Max Extreme Zeiss Merlin operated at 3kV, 130 pA and a working distance of 4.8 mm. To probe the internal structure and crystallographic information of the samples, a Tecnai F20 high resolution transmission electron microscope equipped with energy dispersive x-ray (EDX) spectrometer operated at an acceleration voltage of 200 kV was used. A PANalytical empyrean series 2 x-ray diffractometer operated at 45 kV and 40 mA was used to conduct XRD analysis at a grazing incidence of 0.3°.

The photoluminescence (PL) properties were investigated using a NanoLog®Horiba spectrofluorometer and a 325 nm Xenon laser. UV- Vis analysis was conducted using a Semicon Soft M probe thin film measuring spectrophotometer using halogen and deuterium lamps as the visible and ultraviolet light sources, respectively. Electronic properties of the grown samples were investigated using an ECOPIA HMS-300 Hall Measurement System using the Van der Pauw method at room temperature with a magnetic field of about 0.55 T and operated at varying current of 0.1, 0.25, 0.5, 0.75 and 1 μA. The chemical bonding analysis of the Si NWs was performed using a ThermoESCAlab 250Xi equipped with a monochromatic Al k_α x-ray beam. The solar device properties were investigated using Keithley 2420 to obtain I-V properties and a 100mW/cm^2

solar simulator.

4.3 Results and Discussion

4.3.1 Morphological and structural properties

4.3.1.1 Scanning electron microscopy analysis (SEM)

Figure 4.1 presents a comparison of the morphology of a P3HT/C_{71} thin film (blend only) and the subsequent Si NW distribution within the hybrid thin films.

Figure 4.1: SESI-SEM micrographs of thin films showing an overview of polymer blend:Si NW mixtures at (a) 1:0, (b) 1:0.5, (c) 1:1 and (d) 1:2 ratios.

Figure 4.1 (a) represents an overview image of a smooth P3HT/C_{71} blend thin film with no traces of Si nanostructures on it (as expected). From the SEM

micrographs, the density of the Si nanostructures increased proportionally with the NW ratio in the blend as shown in figure 4.1 (b-d). Furthermore, it can be observed that the Si nanostructures have non-uniform length and diameters as evidenced by the random clusters observed on each sample and these observations can be directly attributed to the MACE growth mechanism of these Si NWs. These observations confirm that the Si NWs were successfully harvested and incorporated into a hybrid polymer/Si NW architecture. Having ascertained the presence and distribution of Si rods within the polymer blend thin film, the need to probe deeper into the morphology of Si NWs and how they affect the morphology of the polymer blend was requisite; hence the employment of HRSEM at higher magnification as shown in figure 4.2.

Figure 4.2 (a) presents HRSEM micrograph images showing a rough surface of the as-purchased indium tin oxide (ITO) substrate without a polymer thin film. A closer inspection of figure 4.2 (b) shows a P3HT only thin film coating also with a coarse texture throughout the thin film surface and shows that the substrate morphology (ITO) has a direct influence on the morphology of thin layers deposited over it. Clearly, this observation combined with other artefacts associated with the spin coating technique can influence properties of such thin films [4.19], such as the morphology and thickness.

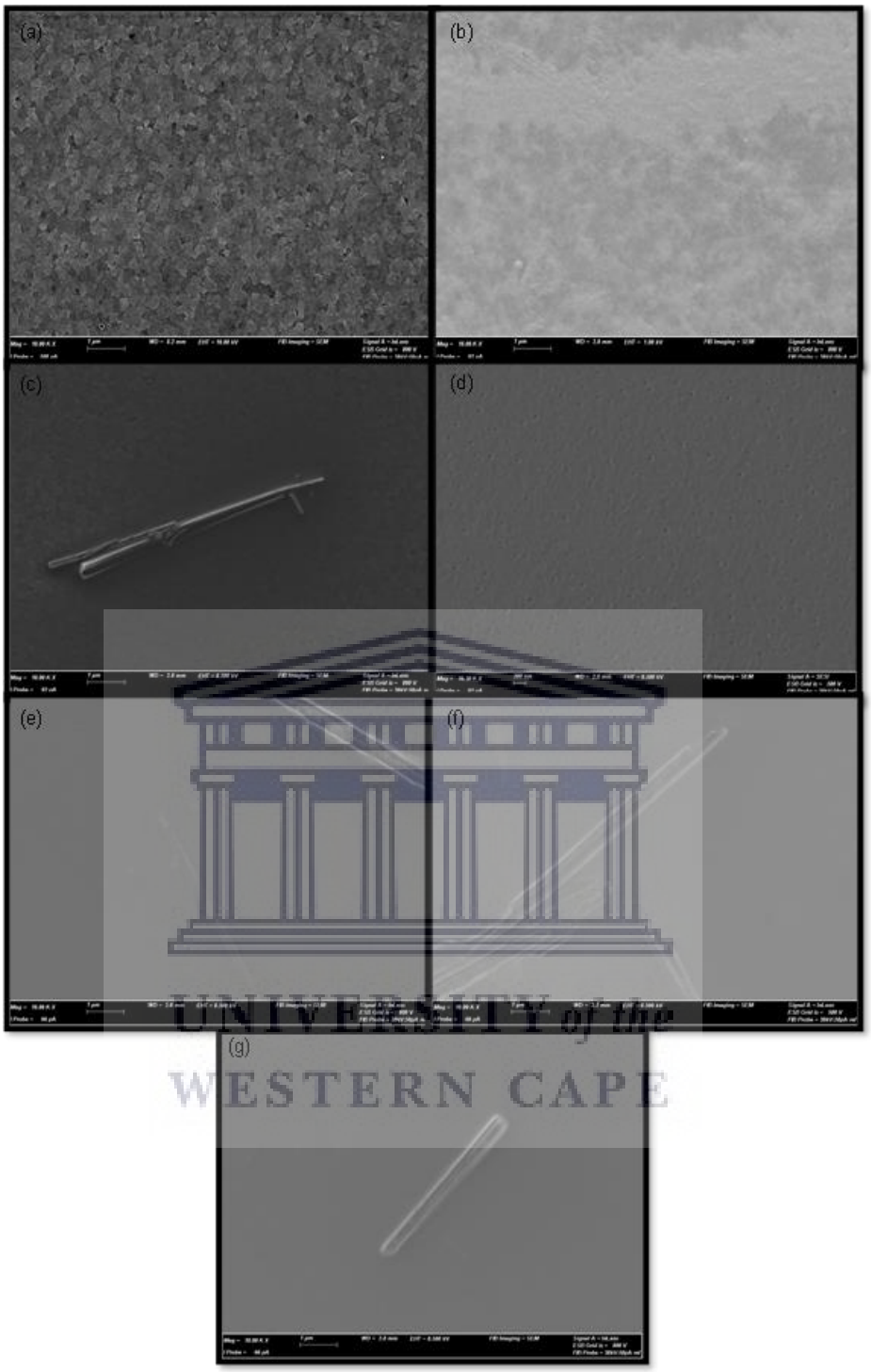

Figure 4.2: Shows HR-SEM thin film images of (a) plain ITO, (b) P3HT, (c) P3HT+ Si NWs, (d) P3HT+PCBM and blend:Si NW mixtures at (e) 1:0.5, (f) 1:1 and (g) 1:2 ratios.

In figure 4.2 (c) a thin film of P3HT + Si NWs is shown with non-uniform morphology whereby the ITO layer morphology starts appearing at the surface on selected parts of the sample similar to the one shown in figure 4.2 (a) and this can be

attributed to the uneven spin coating effect. Implications of this observation mean that a clustered sample can eventually have a different morphology than a lower load ratio sample which can influence other properties of the hybrid film.

Figure 4.2 (d) shows that the surface morphology of P3HT:C_{71} blend without Si NWs consists of pores or perforations distributed evenly on the surface of the thin films. In figure 4.2 (e, f, g), the surface morphology of the blended thin film with Si NWs confirms the non-uniform diameter and length of the Si NWs whereby these features can have a direct influence in the electron transport properties of the Si NWs and the thin film (hybrid film). Clearly, from this investigation, it can be established that the morphology of NWs depends on the MACE process while that of the hybrid film depend on the spin-coating technique and NW distribution. From this analysis a fixed ratio of 1:1 was identified as the optimal ratio to investigate the effect of different Si NW dopant levels in hybrid thin films because it displayed an improved dispersion of Si NWs.

Figure 4.3 presents SEM micrographs of the different hybrid thin films of polymer blend mixed with Si NWs doped at 700, 800 and 900℃ and mixed with a (1:1) ratio. The SEM micrographs presented in figure 4.3 show the morphology of a pure polymer blend in comparison to the blend mixed with Si NWs that were n-doped before mixing at 700, 800, 900℃. From figure 4.3 (a) it can be observed that the polymer blend forms a high-quality uniform thin film with minimal roughness and no perforations which demonstrates the thorough mixing and dissolution of the polymer into the solvent. The corresponding SEM micrographs of the blend mixed with Si NWs (figure 4.3 (b-d)) show a non-uniform distribution of Si NWs in all the three-different samples. Ideally,

no morphological variations can be attributed to the different dopant levels except the randomness of the spin-coating technique.

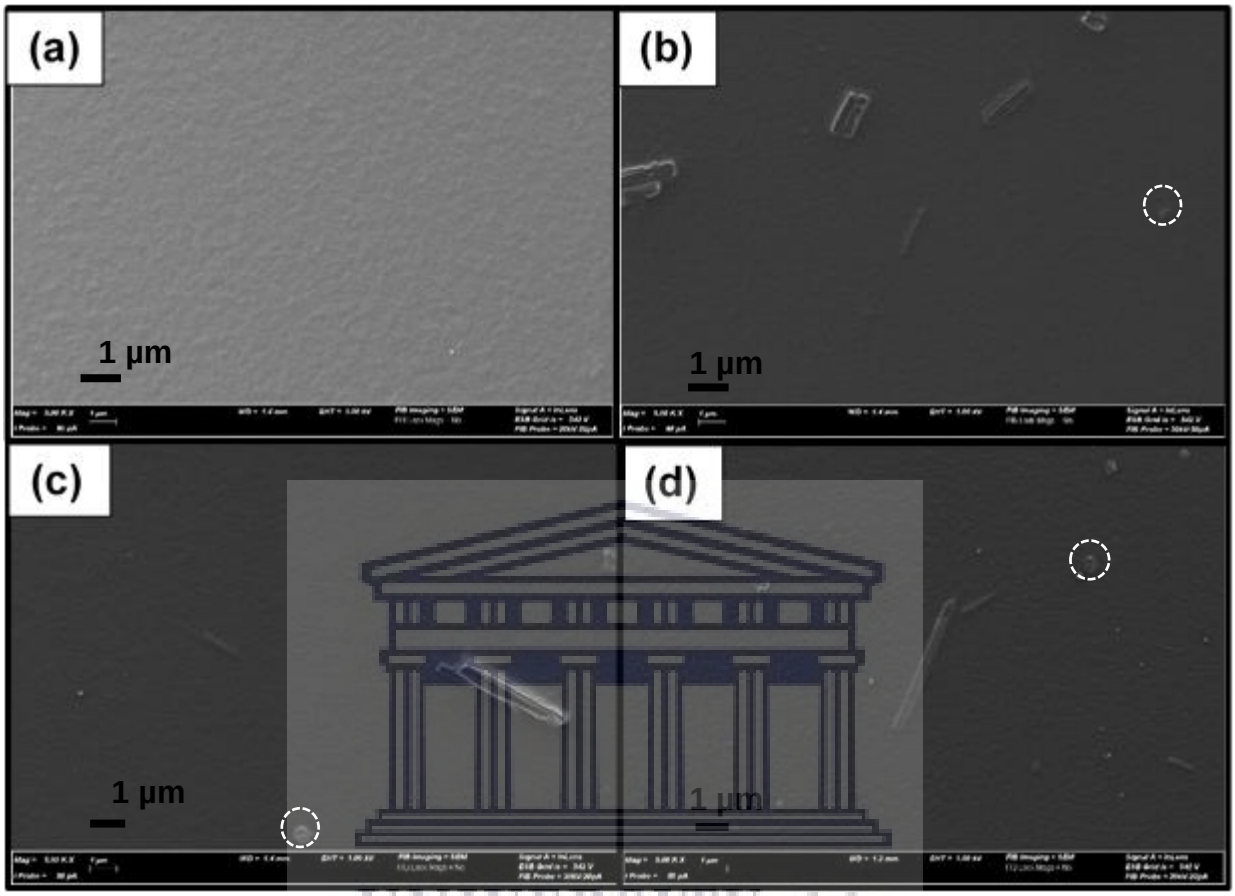

Figure 4.3: SEM micrograph of polymer blend (a) without Si NWs and hybrid thin films with Si NWs doped at different temperatures (b) 700 (c) 800 and (d) 900 ℃.

These micrographs show sparsely distributed Si NWs of different thickness and length with no aggregation as previously observed in figure 4.2. Detailed information on the Si NW morphology, thickness and length is covered in Chapter 3. The minute irregularly shaped particles (dashed circles) observed on the film can be linked to the Si wafer particles dislodged during Si NW array sonication in solvent. These observations confirm that Si NWs were successfully incorporated to form a hybrid thin film and different dopant levels cannot be linked to any variations of the morphology of hybrid thin films. Having ascertained the morphological properties of these

organic/inorganic hybrid thin films, the employment of high-resolution transmission electron microscopy technique was apparent for probing deeper and understand the internal structure of these thin films.

4.3.1.2 Transmission electron microscopy analysis

The morphological and chemical interfacial interaction between the Si NWs and the polymer blend is very crucial in understanding the effects of Si NWs in the electron transport and charge transfer between the Si NWs and the polymer blend thin film. To that end, high resolution transmission electron microscopy (HRTEM) was used to probe the organic/inorganic interface morphology and elemental profiles.

Figure 4.4 (a)-(c) shows Bright-Field (BF) TEM images of a Si NW coated by the P3HT/C_{71}: PCBM blend. At higher magnification in (b) and (c) we can see that the blend forms a coating over the thin shell of the Si NW. Typically, MACE Si NWs have an oxygen-rich Si shell that is amorphous, semi-porous and can act as an electron barrier due to the high defect and porosity density which become charge trap sites resulting in poor electron transport [4.19].

A more in-depth and detailed investigation of the interfacial properties is revealed by the STEM-HAADF micrographs in figure 4.4 (d)-(f), whereby a clear radial Z contrast between Si NWs and the polymer blend is shown to indicate that the polymer blend resides only on the outer shell of the Si NW. Furthermore, the EDS elemental mapping technique was employed to probe the approximate location of the different tracker elements of the constituent materials. These EDS elemental maps in figure 4.4 show a strong C and S contrast on the outer shell of the Si NW with Si exhibiting a strong contrast along the core of the NW while the non-even distribution of P throughout the NW length reveals that the NW is doped with P to make it n-type.

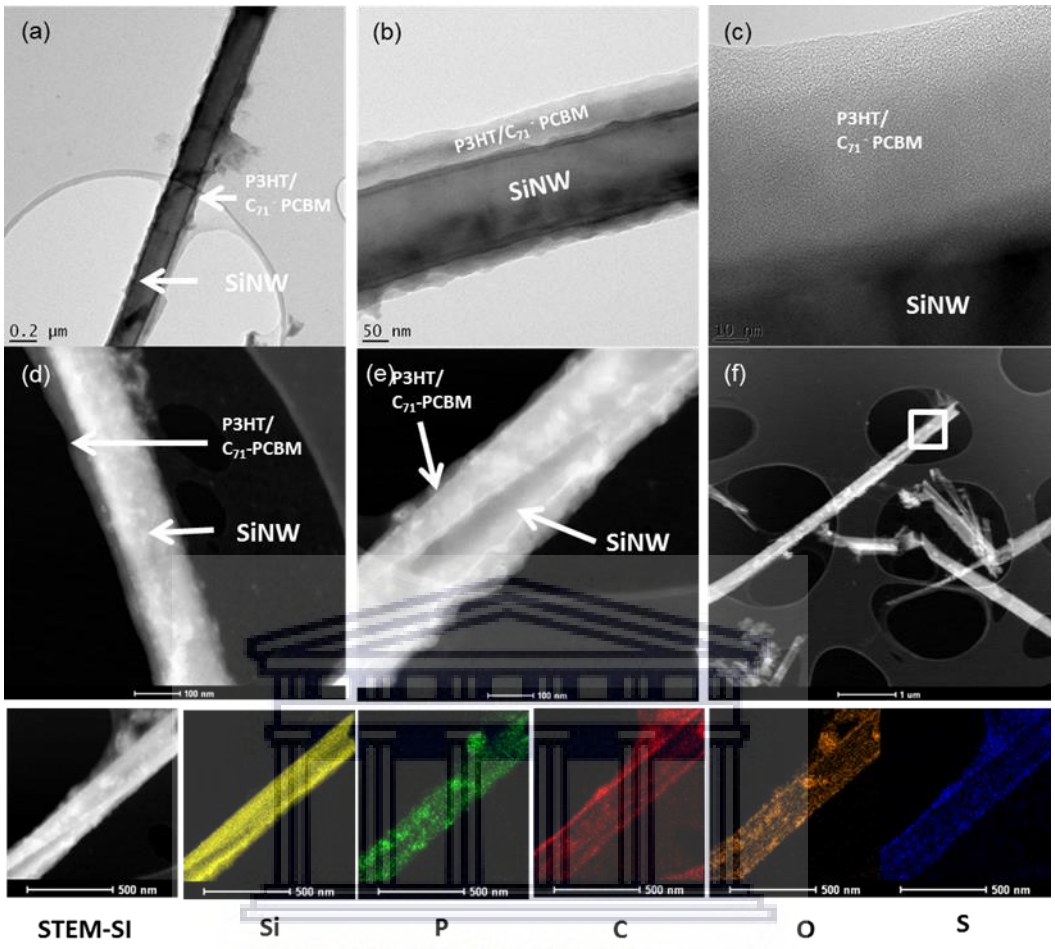

Figure 4.4: TEM Bright-Field images of a Si NW coated with P3HT/C_{71}: PCBM blend from (a)-(c) while the STEM-HAADF images are shown from (d)-(f) and the EDS elemental maps of the constituent elements shown on the bottom row.

The EDS maps shown in figure 4.4 show an average spatial distribution of the various constituent elements on the overall Si NW without definite and sharp boundaries on the locality of each element. This shortfall of the technique necessitates the employment of the EDS line-scan technique as shown in figure 4.5.

In figure 4.5, a STEM-HAADF micrograph shows the area on which the lines-can was conducted across the Si NW and shows the overlaid elemental map of the Si NW.

Corresponding elemental profiles of the various constituent elements across the length of the NW are also presented in figure 4.5 (a)-(d).

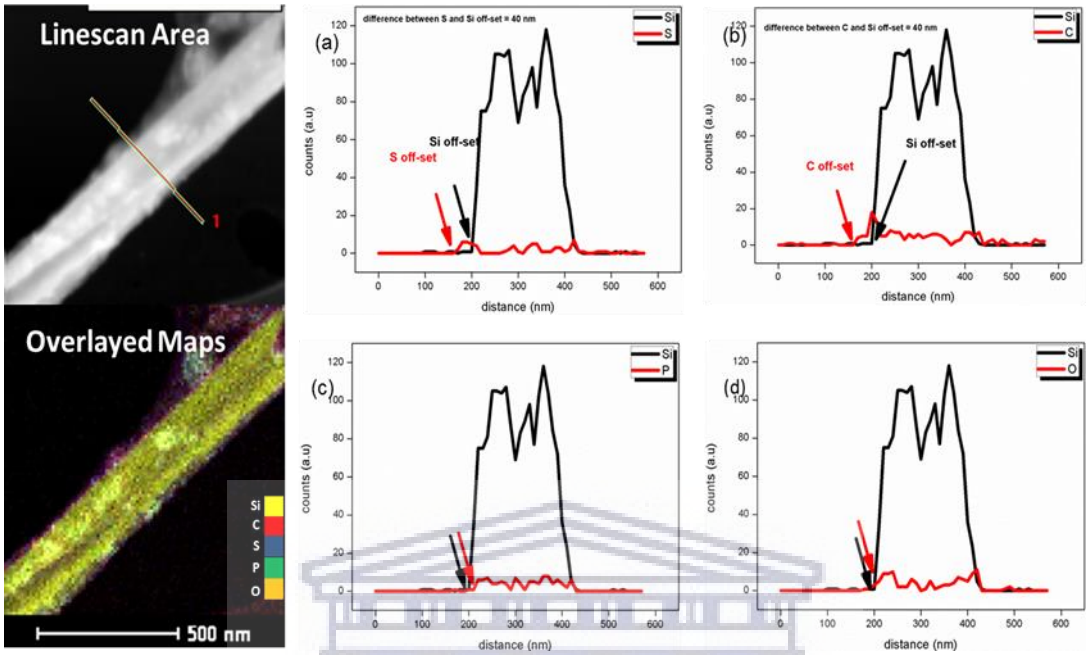

Figure 4.5: EDS lines-cans comparing the Si off-set against the (a) S off-set (b) C off-set (c) P off-set (d) O off-set.

Figure 4.5 (a) and (b) respectively show the S and C off-set at about 40 nm from the Si off-set which can be approximated as the thickness of the polymer blend layer coating the Si NW. In figure 4.5 (c), the P signal offsets within the Si broad peak and maintains a relatively consistent signal throughout the diameter of the Si NW which can be used as an indicator for successful n-doping of the Si NWs subject to validation with other complementary techniques. The spikes observed from the O elemental profile towards the band edges of the Si peak as shown in figure 4.5 (d) confirms that the Si NW has a core shell structure with a Si core surrounded by a thin sheath of oxidised Si.

4.3.1.3 Grazing Incidence X Ray Diffraction Analysis

The GIXRD technique was used to probe the structural ordering of rr-P3HT and its blend (P3HT:PCBM) when loaded with different amounts of n-doped Si NWs and Si NWs of different dopant levels to form the inorganic/organic hybrid matrix. Figure 4.6 shows XRD peak profiles of P3HT, P3HT/C_{71} blend and hybrid thin films with the various Si NW loading ratios. Initially, the addition of Si NWs to the blend results in enhancement of the peak intensity until a certain point where it starts dropping as observed in figure 4.6.

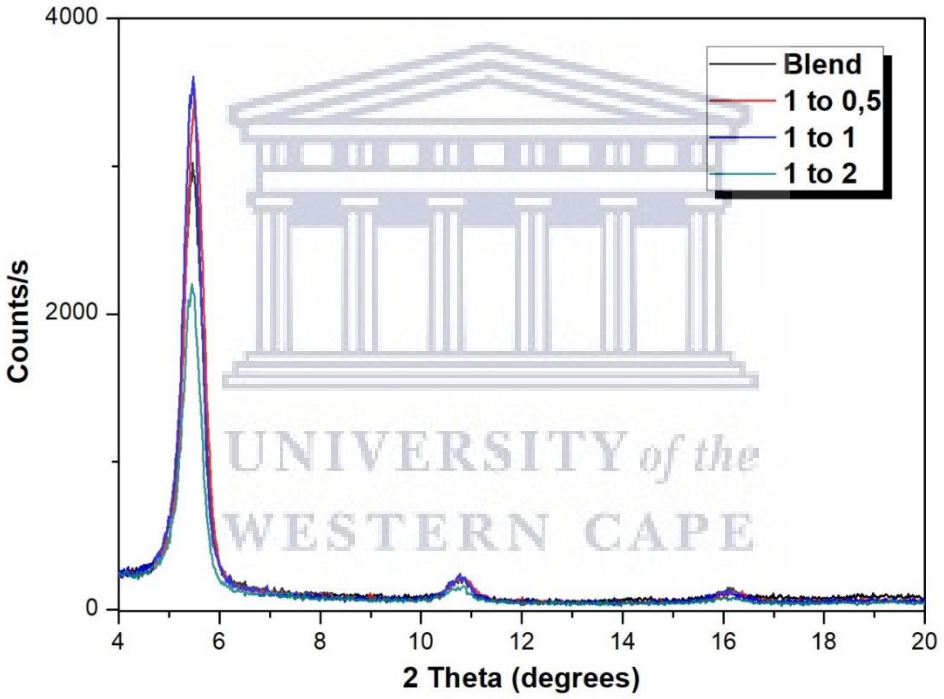

Figure 4.6: GIXRD profile of P3HT:C_{71} blend and the P3HT:C_{71} blend to various Si NW ratios.

From the profiles, it can be observed that smaller amounts of Si NWs (1:0.5) boost the peak intensity and increasing the loading ratio to 1:1 further yields another increase in intensity. However, beyond the this point when the ratio of the Si NWs is increased to 1:2, a significant drop in peak intensity is observed. The observed increase of intensity can be attributed to an increase in the volume or quantity of

ordered domains to a point after which it drops, which is indicative of a structural/bond interaction between the Si NWs and P3HT. Following the observations made after adding different amounts of Si NWs into the polymer blend, it was then inevitable to investigate the effect of the Si NW dopant level on the structure of the hybrid thin films as shown in figure 4.7.

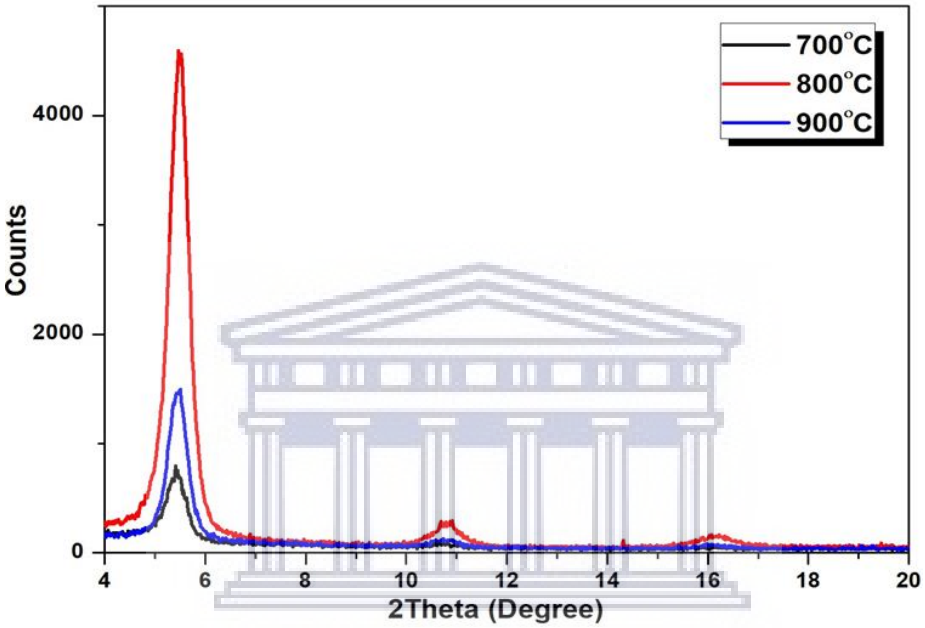

Figure 4.7: GIXRD profiles of polymer blend mixed with Si NWs doped at 700 (low), 800 (mild) and 900 ℃ (highly)

The XRD profiles of all the hybrid thin films presented in figure 4.7 exhibit the P3HT main characteristic (100) and its secondary (200) diffraction peaks at about 5.4° and 10.9° respectively which correspond to the interchain spacing of 1.6 nm. The mildly doped sample (800 ℃) exhibited the strongest peak intensity followed by the highly doped sample (900 ℃) while the lowest doped sample (700 ℃) showed the weakest intensity. These observations can be linked to the different surface morphologies (Si NW/P3HT interface) of Si NW doped at different temperatures as observed in chapter 3.

A summary of the structural parameters of the hybrid thin films are presented in table 4.1 (a) whereby it can be observed that the addition of Si NWs into the polymer blend results in alterations in the structural ordering of the polymer blend as depicted by the peak shifting and minute variations in the FWHM values. The FWHM reduction indicates an increase in “grain-size” or ordered domains upon the addition of higher concentrations of Si NWs. These observed changes can be attributed to chemisorption whereby an interfacial chemical interaction between Si and P3HT can lead to Si passivation and formation of new Si – C bonds that can impact the size of ordered domains in P3HT [4.20]. However, in this study, such a proposition requires further analysis techniques to be validated.

Table 4.1: XRD peak profile parameters for the (a) blend: Si NW ratios and (b) different dopant levels

(a)

Ratio	Peak (°2θ)	FWHM (°2θ)	D Spacing (Å)
1: 0	5.47	0.46	16.1
1: 0.5	5.51	0.43	16.0
1: 1	5.46	0.41	16.2
1: 2	5.45	0.42	16.2

(b)

Sample	Peak Pos. (2θ)	FWHM (2θ)	D Spacing (Å)
700°C	5.4	0.5	16.4
800°C	5.5	0.3	16.1
900°C	5.4	0.3	16.4

From the data presented in table 4.1 (a) and (b), it can be observed that all the samples exhibit a strong P3HT characteristic main peak centred at around 2θ = 5.4° which corresponds to diffraction from the (100) thiophene rings making up the parallel P3HT main chains with alkyl side chains separating them [4.19]. In table 4.1 (a) and (b), changes in FWHM are observed with increasing NW load and dopant temperature of the Si NWs which is indicative of a change in crystallite size. Different NW dopant temperatures result in different Si NW surface states which result in different interfacial chemical reactions and structural disruption of P3HT chains.

Furthermore, the consistent peak position confirms the stability of the crystallization of P3HT even when mixed with amorphous PCBM making it an ideal donor polymer for blends. In a polymer blend, these crystalline P3HT grains interconnect with PCBM to form a matrix whereby smaller P3HT crystals promote charge transfer through a larger surface to volume ratio [4.21]. Furthermore, a smaller P3HT crystallite size can promote charge transfer through creating a shorter diffusion length for excitons hence promoting charge dissociation. During thermal annealing, PCBM molecules may diffuse into each other resulting in the formation of larger PCBM aggregates surrounded by smaller crystallites of P3HT. The presence of bigger PCBM clusters can therefore hinder charge dissociation and transport at the interface due to charge space formation [4.22].

From this work, it is evident that the quantity of Si NWs and the dopant level of the Si NWs has an influence on the structural integrity of the polymer blend. The small variations observed in FWHM can also be attributed to the non-uniform crystallization of the polymer blend thin film upon annealing.

4.3.2 Optical properties

4.3.2.1 Photoluminescence spectroscopy analysis

Photoluminescence (PL) spectroscopy is a powerful tool that can be used to probe the presence of defect states within the bandgap of a material. In a polymer/fullerene blend, this technique can be used to probe the effectiveness of the bulk heterojunction (BHJ) in charge transfer between the donor (polymer) and fullerene (acceptor). PL intensity quenching is one of the properties useful in quantifying the extent of successful exciton dissociation in a sample. The photoluminescence properties of P3HT/$PC_{71}BM$ blend mixed with Si NWs at varying load ratios and a fixed load ratio of Si NWs with different dopant levels were investigated as presented in figure 4.8 and figure 4.9 respectively.

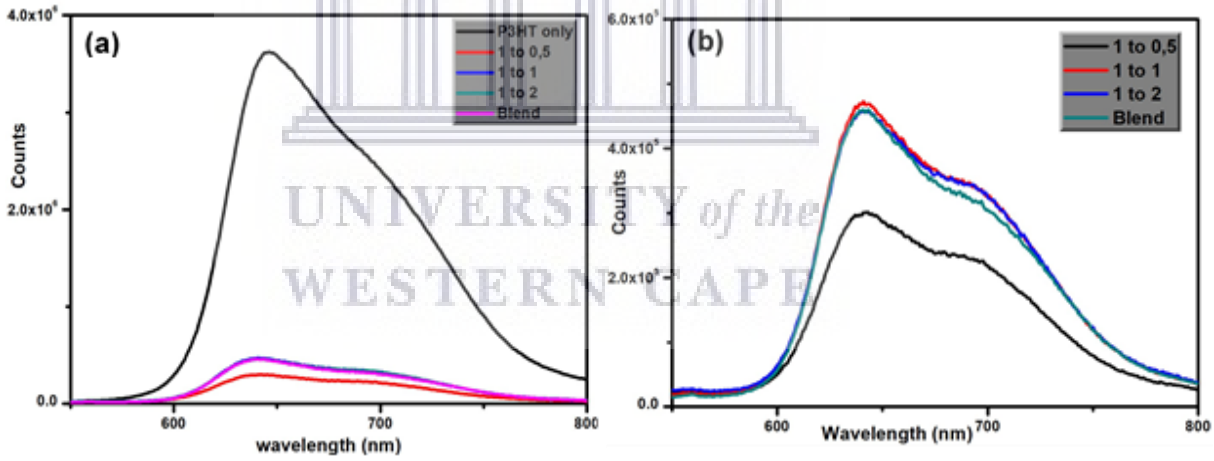

Figure 4.8: PL spectra of P3HT and blends with different Si NW load ratios.

The PL spectra presented in figure 4.8 (a) and (b) show typical P3HT emission spectra characterised by a broad emission band between 600 – 800 nm. Figure 4.8 (a) shows a high intensity PL emission peak from the P3HT only sample which upon mixing with the $PC_{71}BM$ acceptor to form a blend results in quenching of the previously high intensity P3HT PL emission peak. Figure 4.8 (b) shows that, even low loads of

the blend:Si NW (1:0.5) ratio results in effective quenching of the PL emission peak to even below the fullerene acceptor quenching level as demonstrated in figure 4.8(a). This observation provides evidence of an economical benefit since desirable results can be obtained even at low Si NW quantities. Figure 4.8 (b) also shows that, by increasing the Si NW load ratio to 1:1 and 1:2 leads to an increase in PL intensity which then implies that 1:0.5 is the optimal ratio for PL quenching and photovoltaic applications.

Therefore, it can be concluded that hybrid thin films with n-doped Si NWs in smaller concentrations are effective in charge transfer and this can be attributed to the sparse, homogeneous distribution of the Si NWs the 1:0.5 ratio as shown in SEM micrographs (see figure 4.1) and an improved crystallinity as observed in GIXRD. In such hybrid architectures, the LUMO and HOMO of the blend are aligned slightly higher than the conduction and valence band of the Si NWs respectively [4.22]. During quenching, exciton dissociation occurs at the blend/Si NW interface whereby electrons diffuse from the LUMO into the conduction band while holes diffuse from the valence band to the HOMO level [4.23]. In the process of this charge transfer, equilibrium is reached at the Si NW/polymer interface creating a depletion region which then reduces the charge dissociation efficiency of the interface [4.24]. Observations from SEM analysis show that an increase in NW concentration results in more Si NW aggregates or clusters leading to a reduced surface area for exciton dissociation and consequently higher exciton recombination and increased PL intensity as observed.

Having ascertained the effect of different Si NW loading ratios on the PL properties of hybrid thin films, the effects of different Si NW dopant levels were investigated as presented in figure 4.9. As indicated earlier, different dopant levels result in different, defect density, bandgap and eventually optical properties.

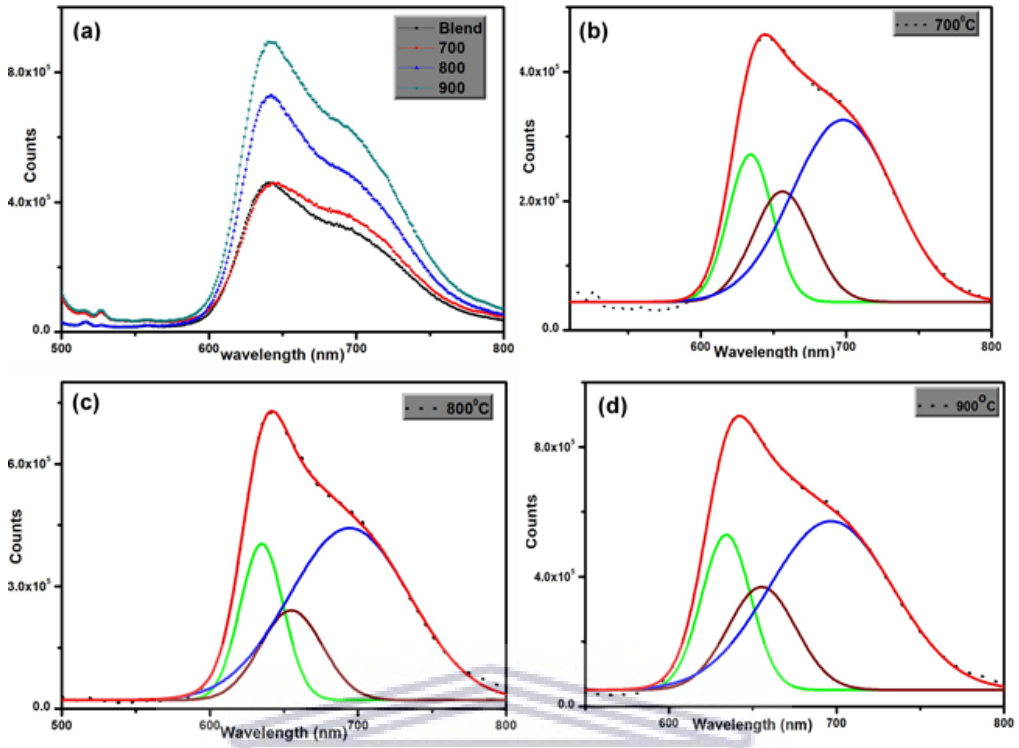

Figure 4.9: PL spectra of a polymer blend only and hybrid thin films with Si NWs doped at 700, 800, and 900 ℃

From the PL spectra presented in figure 4.9 (a), an increase in PL intensity upon the addition of Si NWs is observed and this PL emission intensity increase exhibits a direct relation with the Si NW doping temperature. However, as much as we can observe the effect of the dopant level on the intensity of the peaks, it is crucial to note that these spectra have very similar characteristic features and shape as shown in fig. 4.9 (b), (c) and (d). These PL emission bands can be characterized by the broad emission band between 600 and 800 nm which can be distinctly deconvoluted into three Gaussian peaks centred at about 635, 650 and 725 nm which can be attributed to pure electronic transitions and vibronic transitions respectively.

As evident from figure 4.9, an increase in PL emission was observed for Si NWs doped at higher temperatures and this can be directly linked to an increase in dopant level of the Si NWs with increasing doping temperature. Higher dopant levels result in a higher impurity/defect states density which in turn can become exciton

recombination centres leading to higher intensity PL emission [4.25,4.26]. Observations made in Chapter 3 show that Si NWs have a broad PL emission spectrum (550-800 nm) due to factors such as quantum confinement, SiO_2 surface layer, embedded Si NCs and interfacial defect states. This clearly shows that some of the enhanced intensity observed could be a direct contribution from the Si NWs. From fig. 4.9 (a) it can be observed from the PL spectrum that the highly doped Si NW sample exhibited the highest PL emission intensity because of the high density of defect states due high impurity/dopant content.

4.3.2.2 UV-Vis spectroscopy analysis

Ultraviolet – visible absorption properties of the hybrid thin films were investigated to establish the influence of adding different amounts of Si NWs and Si NWs of different dopant concentrations in a polymer blend. Figure 4.10 (a) shows the UV-Vis absorption properties of a P3HT/PCBM blend and the blend with varying Si NW load ratios to form hybrid thin films.

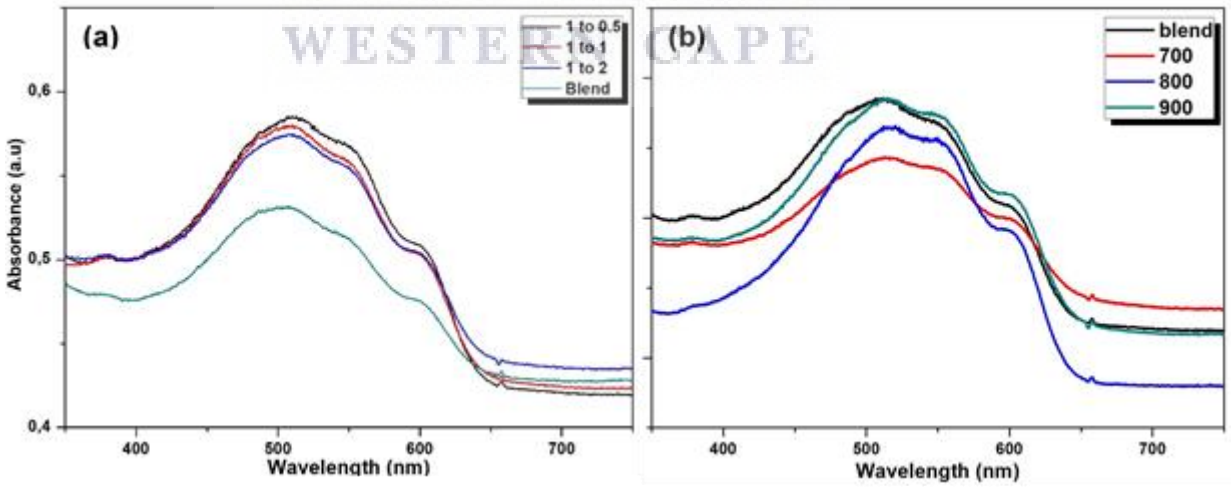

Figure 4.10: UV-Vis absorption of hybrid thin films with (a) different Si NW load ratios and (b) Si NWs doped at different temperatures.

From figure 4.10 (a), it is evident that the blend only film exhibits a relatively weaker absorption band in the visible between 450 – 650 nm characteristic of P3HT thin films. Upon the addition of Si NWs into the polymer blend, an enhanced absorption in the UV-Vis and NIR region is observed and this enhanced absorption can be attributed to the higher absorption coefficient of Si NWs. The best polymer blend/Si NW ratio was found to be 1:0.5 and increasing the NW ratio resulted in a slight decline of the absorption capability of the thin films. This observation can be linked to the non-homogeneous hybrid thin films due to bigger clusters of NWs that can result in non-uniform film thickness.

Similarly, figure 4.10 (b) shows UV-Vis absorption properties of the hybrid thin films produced by the mixing polymer blend with Si NWs doped at different temperatures. These UV-Vis spectra can be characterized by a broad absorption band (400 – 650 nm) which is composed of three (3) characteristic peaks being the onset peak at about 520 nm, the λ max peak at 550 nm and the tailing peak at about 600 nm.

Furthermore, it can be observed from fig. 4.10 (b) that the addition of Si NWs of different dopant levels did not yield enhanced UV-Vis absorption by the hybrid thin films. However, slight variations in sample absorption capabilities were notable whereby the addition of low-doped Si NWs (700℃) resulted in the lowest absorption within the visible range which improves in the near infra-red region while mild-doped sample at 800℃ exhibited lowest absorption in the UV and near infra-red region while the Si NWs doped at 900℃ showed the best performance throughout the range and exhibited no significant drop in absorption when compared to the polymer blend only thin film. These observations indicate that the highly doped Si NWs (900℃) are the

most ideal for the inorganic/organic hybrid thin films applications since they exhibited an insignificant decline in absorption capabilities.

This lack of improvement in UV-Vis absorption properties can be directly linked to the sparse random distribution of the Si NWs within the hybrid thin film which negates the total internal reflection effects offered by vertically oriented as-grown Si NWs. Some samples further showed a significant decline in the absorption and this can be due to non-uniform film thickness resulting in varying absorption coefficients.

4.3.3 Chemical surface analysis (XPS)

Quantitative chemical information about the organic/inorganic hybrid thin films was obtained using a low energy Ar^+ ion beam in an XPS whereby a polymer blend and a polymer blend mixed with Si NWs were analysed. The hybrid thin film with the highest Si NW load (1:2) was analysed to increase the probability of detecting the Si_{2p} signal from the sample. Chemical surface analysis to a depth of about 5-10 nm was conducted as shown by the results in figure 4.11 through monitoring the any variations on the S (sulphur) peak because of the presence of Si NWs.

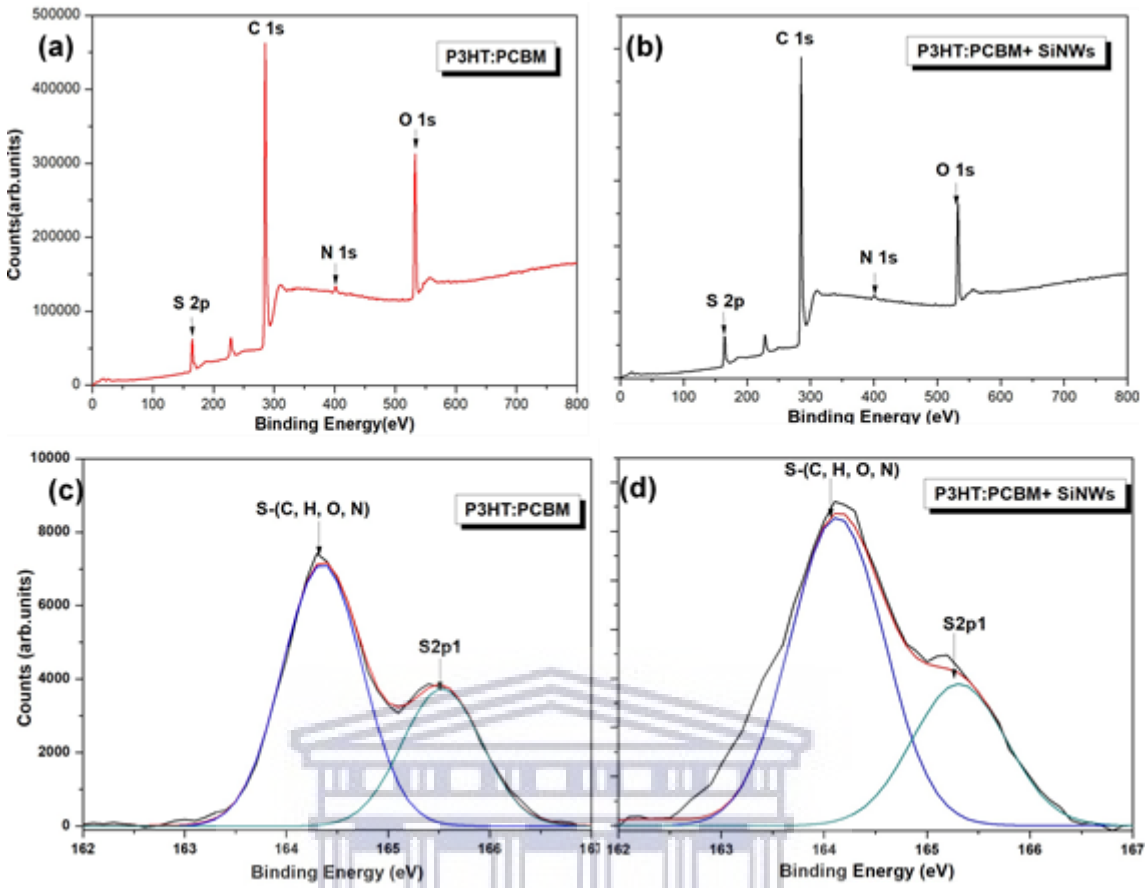

Figure 4.11: XPS survey scan of (a) blend only, (b) blend + Si NWs (1:2 ratio) and their corresponding high-resolution scans in (c) and (d) respectively.

XPS survey scans in figure 4.11 (a) and (b) show an overview of the prevalent surface chemical composition characterised by the signature S-2p line from the P3HT thiophene rings [4.27]. However, it is interesting to note that there is no Si signal detected from the blend+Si NWs sample. This observation can be attributed to very low Si concentration on the survey area and can also be due to XPS probing only the surface of the thin film while other techniques such as GIXRD probe the bulk to confirm the presence of Si NWs in the hybrid thin films.

During XPS analysis, the binding energies of core electrons can be affected by the surrounding chemical environment which may result in slight peak-shifting being observed. The high resolution XPS spectra displayed in figure 4.11 (c) and (d) shows

the two S peaks centred at about 164 eV (S-C) and 165,5 eV (S_{2p}) [4.28] obtained from the P3HT:PCBM surface and originating from the thiophene rings. However, even though the Si signal was not observed during the survey scan in figure 4.8 (b), there is an observed effect of Si NW addition into the P3HT:PCBM blend as observed between figure 4.11 (c) and (d). The peak broadening and early peak onset observed in figure 4.11 (d) due to Si NW loading can be attributed to chain breaking between thiophene rings and polymer chain backbone [4.29] caused by the presence of Si NWs in the polymer matrix.

4.3.4 Electronic properties (hall-effect measurements)

Morphological and structural investigations have confirmed the successful incorporation of Si NWs into organic (polymer/fullerene) blends to form an organic/inorganic hybrid thin film. However, as highlighted earlier, one of the roles of Si NWs is to enhance the electron transport properties of hybrid structures, which in turn addresses challenges like premature degradation of polymer based solar cells. In this work, hall-effect measurements were conducted to quantify the relative enhancements on the several electron transport properties between the different samples. Furthermore, electronic properties of these materials can be used to establish and verify the relative dopant levels between the samples.

Table 4.2: Electronic properties of different Si NW load ratios

Sample (Blend: SiNW)	Bulk Conc. (cm^{-3})	Mobility ($cm^2/V.s$)	Resistivity (Ω.cm)	Conductivity $(Ω.cm)^{-1}$	Sheet Conc. (cm^{-2})
1:0	-4.9 E17	1.87 E03	6.84 E-03	1.4 E02	-9.8 E12
1:0.5	-9.7 E19	4.63 E02	1.39 E-04	7.1 E03	-1.9 E15
1:1	-5.8 E20	4.24 E01	2.54 E-04	3.9 E03	-1.2 E16
1:2	-1.6 E21	1.14 E01	3.34 E-04	3.0 E03	-3.3 E16

As an overview, it can be observed from table 4.2 that the addition of Si NWs at different load ratios resulted in an overall enhancement of the electronic properties when compared to the organic blend only sample. Evidently, it can be observed that, the loading of n-doped Si NWs into the organic blend has a direct impact on the bulk concentration of charge carriers such that the highest NW load ratio corresponds to high carrier concentration. However, the mobility of the charge carriers displayed an inverse relation to the quantity of Si NWs loaded into the organic blend. Furthermore, it is observable from the table that the lowest concentration of Si NWs yielded the highest enhancement in conductivity while the highest load ratio exhibited minimal gains over the polymer blend sample.

Consequently, when the load ratio increases, the quantity of n-doped Si NWs mixed into the organic blend also increases resulting in an overall increase of the negative charge carriers due to the higher proportion of the acceptor (n-type) species compared to the donor (p-type) species hence the direct relation between load ration and bulk concentration. However, charge carrier mobility displays an opposite trend since the mobility of these charge carriers decreased with increasing charge carrier concentration (load ratio), a trend that is analogous to bulk Si behaviour. This

observation can be attributed to the high probability of charge carrier collisions which eventually reduces the mobility of carriers as the carrier density (concentration) increase in a sample.

On the contrary, the low Si NW load ratio (1:0.5) sample exhibited the best carrier mobility and conductivity properties which are crucial parameters in solar PV performance while highest load ratio sample falls short in this regard. This observation correlates well with microscopy observations that show a semi-homogeneous distribution of Si NWs with less agglomeration and clustering when compared to higher NW load ratio samples. These clusters of Si NWs have a lower surface to volume ratio which reduces the charge separation capability of these Si NWs.

Establishing the different dopant levels of Si NWs is one of the most challenging exercises requiring sophisticated techniques with the ability to isolate an individual NW and measuring it properties. However, the hall – effect measuring method can also be used to establish variations in electronic properties which then gives the relative dopant levels between samples. The fixed Si NW quantity among the three samples is very crucial in ensuring that any variations in electronic properties of the hybrid thin films can be solely ascribed to the dopant level (temperature) of the Si NWs present in the sample.

Table 4.3 presents a summary of the Hall-effect measurement results obtained from the P3HT/PCBM polymer blend mixed with Si NWs doped at different temperatures leading to low (700℃), mid (800℃) and high doped (900℃) Si NWs to form hybrid thin films.

Table 4.3: Summary of Hall-effect measurement properties

Sample	Bulk Conc. (cm^{-3})	Conductivity $(\Omega.cm)^{-1}$	Resistivity ($\Omega.cm$)	Mobility ($cm^2/V.s$)	Sheet Conc.(cm^{-2})
700°C	-9.04 E17	2.61 E01	3.84 E-02	1.84 E02	-1.81 E13
800°C	-1.84 E19	2.89 E02	3.46 E-03	9.81 E01	-2.46 E14
900°C	-6.04 E19	8.09 E02	1.24 E-03	8.38 E01	-1.21 E15

The results presented in table 4.3 clearly indicate an increase in bulk carrier concentration with increasing Si NW dopant temperature, consequently indicating a relative increase of the dopant level from low – mid – high doped between the three samples. The direct relation between the Si NW doping temperature and bulk concentration can be attributed to the enhanced phosphorous ability to diffuse into Si as the doping temperature increases. This phenomenon can be further explained by the P dopant diffusion kinematics in Si which are governed by the diffusivity of P in Si and temperature [4.30,4.31]. Therefore, the low bulk concentration exhibited by low doped (700℃) sample can be ascribed to the low n dopant level of Si wafer used and the stunted diffusion of P into Si at 700℃ compared to the higher temperatures of 800℃ and 900℃.

The conductivity values obtained from the samples exhibited an increase with increasing dopant level (temperature) whereby the low and high temperature hybrid samples gave the lowest and highest values respectively. The higher conductivity value exhibited by the higher dopant temperature sample can be attributed to the highly doped Si NWs embedded in the organic blend which increases the quantity of electrically active charge carriers leading to the enhancement of charge conductivity within the sample. As depicted earlier, the dopant temperature of Si NWs has a direct

impact on the carrier concentration of the NW. Furthermore, Pi et al. [4.32] in his work observed that during P doping of Si nanostructures, P atoms can diffuse into the core of the NW while some may reside on the Si nanocrystal surface resulting in even higher electrical conductivity enhancement compared to bulk Si if they can move from one NC to the next at high saturation [4.32]. In other work, Ko et al [4.33], was able to demonstrate that the conductivity of Si NWs can be affected by defects such as vacancy point defects, surface dangling bonds whereby dopant atoms get trapped in these defect sites and render them as redundant charge carriers. To overcome this barrier, higher dopant concentrations may be necessary to observe enhancement in conductivity as exhibited by the highly doped sample in table 4.3.

As observed above, the conductivity enhancement that is displayed by the highly doped sample clearly outweigh the negative effects of high dopant concentration such as the decrease in charge carrier mobility with increasing charge carrier concentration as shown in table 4.3. In solar PV applications, the conductivity and mobility of charge carriers plays a very crucial role in determining the current density (Jsc) and in turn the PCE of the SC. From these results, a clear footprint of the Si NW electronic properties can be distinctly observable through the hybrid matrix electronic properties implying an overall improvement of the organic blend properties as depicted by the gains observed.

4.3.5 Device properties

Several techniques have been used to show improvements in structural, optoelectronic and electron transport properties of P3HT/PCBM/Si NW hybrid structured thin films achieved through the addition of Si NWs of different amounts and dopant levels. However, for solar PV applications, these improvements become more impactful if they have a positive impact on the final solar device performance

parameters. In order to obtain these SC (solar cell) parameters, the J – V characteristics of the hybrid devices with different amounts and dopant levels of Si NWs are investigated. Graphical representations of the different hybrid solar cell parameters are presented in figure 4.12 showing the relative improvements achieved through varying the Si NW load ratio and dopant level of the Si NWs used.

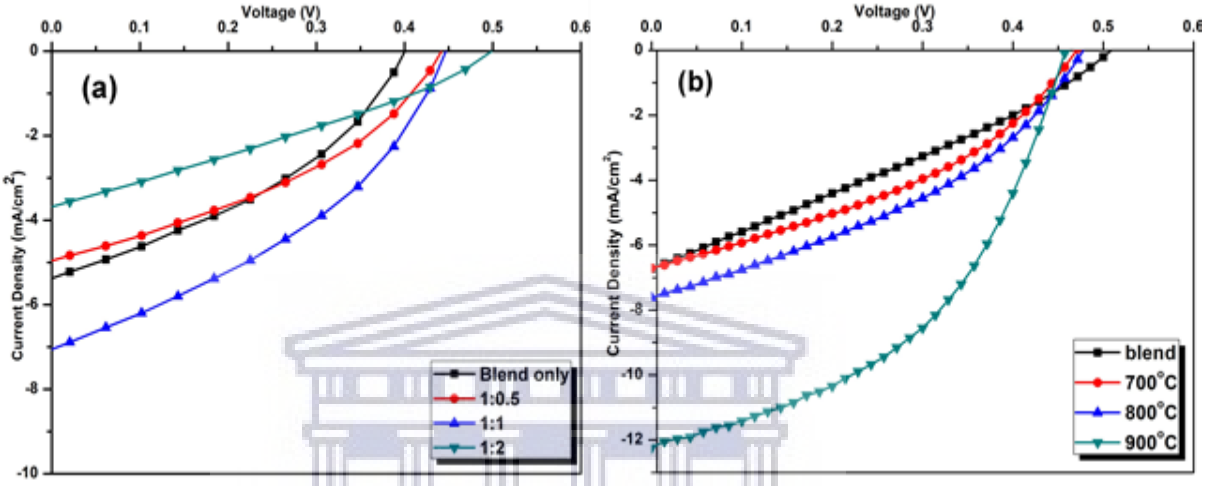

Figure 4.12: J-V curves for hybrid solar cells with different (a) Si NW load ratio, (b) Si NW dopant temperature (level)

The J-V characteristics curves in figure 4.12 (a) show the variations in solar performance parameters as a result of different Si NW load ratios on hybrid solar cells. From the shape of the J-V curves it can be observed that the 1:1 ratio is optimal for solar cell performance while the highest load (1:2) produced the worst performance based on the area under the curves. Similarly, figure 4.12 (b) shows the effects of Si NWs of different dopant levels on the performance of hybrid solar cells. Based on the shapes of the J-V curves, it can be observed that the highly doped sample (900℃) exhibited the best solar performance followed by the mid doped, low doped and blend only samples respectively. These observations made from the graphical presentations can be fully supported in detail by the summary of the solar cell tabulated in table 4.4.

Table 4.4: J – V characteristics of hybrid solar cells with different Si NW ratios

Sample	V_{oc} [V]	J_{sc} [mA.cm^{-2}]	η [%]	FF [%]
1:0	0.39	5.53	0.80	0.37
1:0.5	0.42	5.08	0.82	0.38
1:1	0.43	7.23	1.19	0.38
1:2	0.51	3.80	0.54	0.27

From table 4.4, an overall improvement in PV properties of the organic solar cell are observed after the addition of Si NWs at different ratios. A steady increase in open circuit voltage V_{oc} of about 30% is observed at the maximum Si NW load ratio sample (1:2). This observed trend tallies with observations made by Pietsch et al. [4.1], whereby he observed that the V_{oc} of an organic solar cell is highly dependent on the charge separation efficiency of that solar and this property is dependent on the quality of BHJ interfaces within the active layer [4.1]. Therefore, the high V_{oc} values obtained from the high Si NW load ratio (1:2) SC can be attributed to effective charge separation and less recombination as influenced by the high charge carrier concentration exhibited by the electron transport properties (table 4.2). Furthermore, this observation correlates well with the SEM observations of a dense Si NW distribution (1:2) leading to a higher charge separation capacity.

Similarly, a maximum increase of about 30% in the short circuit current density (J_{sc}) was observed for the (1:1) mild Si NW load ratio hybrid solar cell while the highest load ratio sample yielded the lowest J_{sc}. The high J_{sc} value obtained from the 1:1 ratio device can be attributed to good optical absorption, moderate Si NW clustering and the higher conductivity leading to formation of low resistance interface between aluminium contact and active layer hence the high FF also. The lower J_{sc} observed from the higher load ratio device (1:2) can be attributed to higher defects/alternative current paths within the active layer leading to lower shunt resistance R_{sh}.

In hybrid/organic solar cells, parasitic losses emanating from the quality of the contact electrode, the resistance between the contact and active layer (series resistance, R_s) significantly reduce the J_{sc} and fill factor (FF) of a SC leading to lower power conversion efficiency η. However, in table 4.4 the enhancements in V_{oc} and J_{sc} yielded a 49% increase in power conversion efficiency (PCE) η for the (1:1) sample. The observed increase in PCE can further be attributed to a combination of low R_s and high R_{sh} in the (1:1) sample which results in high J_{sc} and V_{oc} values hence the higher power conversion efficiency [4.34]. The fill factor did not exhibit any significant improvement (2%) upon the addition of Si NWs and this may be attributed to an architectural artefact throughout all the solar cells.

The optimal Si NW load ratio for the performance of hybrid solar cells was found to be (1:1) and this fixed ratio was also used to investigate the effect of different NW dopant levels in SC performance as shown in table 4.5.

Table 4.5: J-V characteristic of hybrid SC`s with Si NWs at different dopant levels

Sample	V_{oc} [V]	J_{sc} [mA/cm^2]	η [%]	FF [%]
Blend only	0.51	6.73	0.98	0.28
700 ^{0}C (low)	0.47	6.71	1.22	0.33
800 ^{0}C (mild)	0.47	7.61	1.37	0.39
900 ^{0}C (highly)	0.46	12.24	2.61	0.46

The summary of J-V characteristics presented in table 4.5 show that there was no direct enhancement of the V_{oc} by changing the dopant level of the Si NWs added while the blend only sample maintained a 10% higher V_{oc}. The observed V_{oc} variations between the low, mid and high doped sample were within 2% which is insignificant considering the change in dopant level. This observation can be attributed to the fact that even though the Si NW dopant levels may increase on the different samples, however the net change in the electron and hole levels minus charge recombination is insignificant. Furthermore, this observation correlates with the PL measurements done on the samples which exhibited and increased photoluminescence with higher doping levels.

From table 4.5, it is evident that there was a huge increase in the J_{sc} with increasing dopant concentration of the Si NWs as observed on the sample with highly doped Si NWs (900℃). Initially, at low dopant (700℃) concentrations there was no enhancement of J_{sc} observed but as the dopant level increased, a significant rise in J_{sc} was evident because of the increase in charge carrier quantity on the acceptor material (Si NWs). For the highly doped sample, current-density values observed were even two-fold compared to the sample without doped Si NWs including the low doped sample. These observations further correlate with the high conductivity values

obtained from the hall-effect measurements. Furthermore, it can be concluded that the higher carrier concentration and conductivity have a positive impact on exciton dissociation and the diffusion length leading to an effective donor – acceptor (D – A) interface.

The FF of a solar cell is a crucial indicative parameter for solar cell performance which is characterized by the shape of the J – V curve and is a combination of V_{oc}, J_{sc} and other cell properties such as parasitic resistances. Clearly, a steady increase in FF with increasing dopant level is observed in table 4.5 and confirmed by the J – V curves in figure 4.12(b). As previously observed, this increase agrees with the enhancement of other parameters such as J_{sc} of the SC`s. The increasing trend displayed by the FF can be directly linked to the reduction in series resistance due to the highly conductive and high dopant concentrations of the Si NWs doped at 900 ℃. Based on the trends set by the V_{oc}, J_{sc} and FF, it is expected that the PCE also follows a similar trend whereby it increases with increasing dopant level. A two-fold improvement in power conversion efficiency for the high doped sample over the blend only and lower doped samples was observed and can be linked to the high J_{sc} and V_{oc} combination. Furthermore, these results correlate very well with the observations made during hall – effect measurements whereby the highly doped sample exhibited the most significant enhancement of electronic properties viz a viz its counterparts.

4.4 Conclusions

Si NW/Polymer hybrid thin films and solar cells were successfully fabricated by mixing a P3HT:PCBM blend with Si NWs at different NW load ratios and dopant level. These hybrid structures were extensively characterized to establish the optimal ratio and NW dopant level for solar cell applications. SEM analysis showed that a higher NW load results in formation of clusters resulting in poor film morphology which can

even hamper optical properties of the film. HRTEM analysis was employed to investigate the NW – blend interface which showed a clear interface on the outer shell without polymer diffusion into NW core as established from EDS lines-cans. Furthermore, the addition of Si NWs into the polymer blend was found not to degrade the fundamental structural properties of the blend indicated by the no-shift in XRD peak position upon the addition of NWs at different load ratios and dopant levels. Optical properties were greatly enhanced by the addition of Si NWs such that the 1:0.5 ratio exhibited the best UV-Vis absorption and PL quenching effect. However, PL emission analysis at different dopant levels showed that the addition of Si NWs introduced new defect states which increased with dopant level resulting in the highly doped sample having the highest PL emission intensity.

During XPS analysis of the samples, the Si signal was not observed from the hybrid thin films due to sensitivity of the technique used. However, the Si NW load effect could be traced and linked to the peak broadening of the S_{2p} peak. The main role and effect of the varying dopant levels in Si NWs was observed in the charge-carrier transport properties whereby conductivity was significantly enhanced by the increase in dopant level owing to the one-dimensional structure and the additional charge carriers from the dopant. Similarly, a proportional enhancement of electronic properties such as bulk concentration and conductivity was observed with increasing NW load ratio. These enhancements in charge transport properties are further confirmed by the solar cell performance parameters whereby the J_{sc} improved significantly with increase in dopant level and NW load ratio. Similarly, the PCE of the solar cells followed the same trend such that the optimal load ratio was found to be 1:1 at the highest dopant level.

These results demonstrate clearly that the unique charge transport properties of standalone Si one-dimensional NWs were successfully transferred and carried over to the organic-inorganic hybrid matrix resulting in a more efficient hybrid solar cell than the purely organic device as shown in the results.

References

[4.1] M. Pietsch, M.Y. Bashouti, S. Christiansen, J. Phys. Chem. C 117, (2013) 9049-9055.

[4.2] Y. Jiang, X. Gong, R. Qin, H. Liu, C. Xia, H. Ma, Nanoscale. Res. Lett. 11(267), 2016.

[4.3] S. Trotzky, T. Hoyer, W. Tuszynski, C. Lienau, J. Parisi. J. Phys. D: Appl. Phys. 42, (2009) 055105.

[4.4] B. Eisenhawer, S. Sensfuss, V. Sivakov, M. Pietsch, G. Andra, F.Falk, Nanotechnology. 22, (2011) 315401.

[4.5] J. Davenas, E. Beyou, A. Balloffet, D. Cornu, S. Vignoli, J. Non-Cryst. Solids. 358, (2012) 2534-2536.

[4.6] D.H. Wang, J.K. Kim, J.H. Seo, O.O. Park, J.H. Park. Sol. Energy Mater Sol. Cells. 101, (2012) 249-255.

[4.7] S. Jang, J. Sung, B. Chang, T. Kim, H. Ko, K. Koo, D. Cho, Sensors. 18, (2018) 3304

[4.8] R. Liu, Materials. 7, (2014) 2747-2771

[4.9] Y.J. Kim, T.K. An, S.J. Oh, D.S. Chung, C.E. Park, APL Mater. 2, 076108 (2014)

[4.10] M. Deshpande, R. Seyezhai, IJIRCCE. 2(3), (2014) 3387.

[4.11] K. Oniy Aghmiyoni, V. Ahmadi, F. Arabpour Roghabadi, Procedia Mater. Sci. 11, (2015) 639-643.

[4.12] E. Garnett, P. Yang, Nano Lett. 10, (2010) 1082-1087.

[4.13] Y. Cui, X. Duan, J. Hu, C. M. Lieber, J. Phys. Chem. B. 104(22), (2000).

[4.14] G. H. Jun, S. H. Jin, B. Lee, B. H. Kim, W. S. Chae, S. H. Hong, S. Jeon, Energy Environ. Sci., 6 (2013) 3000.

[4.15] J. Davenas, E. Beyou, A. Ballofet, D. Cornu, S. Vignoli, J. Non-Cryst. Solids., 358 (2012) 2534-2536.

[4.16] L. Yang, L. Pei, S. Hai-Bo, C. Dan, D. Qian-Min, W. Le, Chin. Phys. B, 23(6), (2014) 067304.

[4.17] N. Nafie, M. Abouda Lachiheb, M. Ben Rabha, W. Dimassi, M. Bouaicha, Physica E., 56, (2014) 427-430.

[4.18] S.M. Sze, K.K. Ng. Physics of semiconductor devices, John Wiley & sons, New York, NY, USA, (2006)

[4.19] U. Zhokhavets, T. Erb, G. Gobsch, M. Al-Ibrahim, O. Ambacher. Chem. Phys. Lett. 418, (2006) 347-350.

[4.20] M. Rahmani, L. Jerbi, A. Meftah, J. Luminesc. 217, (2020) 116805.

[4.21] C. Poelking, K. Daoulas, A. Troisi, D. Andrienko. Adv. Polym. Sci. 12, (2014) 277.

[4.22] V.J. Babu, S. Vempati, S. Sundarrajan, M. Sireesha, S. Ramakrishna. Sol. Energy. 106, (2014) 1-22.

[4.23] H. Saidi, A. Walid, A. Bouazizi, B.R. Herrero, F. Saidi. Mater. Res. Express. 4, (2017) 035007

[4.24] A. Moliton, J. M. Nunzi, Polym. Int. 55, (2006) 583-600.

[4.25] M. Fujii, A. Mimura, S. Hayashi, D. Kovalev, Appl. Physic. Lett., 75(2), (1999) 184-186.

[4.26] X.D. Pi, R. Gresback, R.W. Liptak, S.A. Campbell, U. Kortshagen, Appl. Physic. Lett., 92(12), (2008) 123102.

[4.27] Y. Busby, E.J.W. List-Kratochvil, J.J. Pireaux, Appl. Mater. Interfaces. 9, (2017) 3842-3848.

[4.28] Z. Xu, L.M. Chen, G. Yang, C.H. Huang, J. Hou, Y. Wu, G. Li, C.S. Hsu, Y. Yang, Adv. Funct. Mater. 19, (2009) 1227-1234.

[4.29] K. Norrman, M.V. Madsen, S.A. Gevorgyan, F.C. Krebs, J. AM. CHEM. SOC. 132, (2010) 1688316892.

[4.30] D. Moon, M. Seol, J. Han, M. Meyyappan, Nano Res., 10(8), (2017) 2854-2855.

[4.31] H. Lee, M. Kang, S. Choi, G. Kang, J. Myoung, H. Song, Curr. Appl. Phys., 13(8), (2013) 1718-1722.

[4.32] X. Pi, J. Nanomater., (2012) 912903.

[4.33] Y.J. Ko, M. Shin, S. Lee, K.W. Park, J. Appl. Phys., 89, (2001).

[4.34] P. Singh, N.M. Ravindra, Emer. Mater. Res. 1, (2011) 33-38.

Summary and Conclusions

In this thesis, we have been able to focus on some of main challenges in the development of cheaper, more stable, and efficient organic solar cells. In other works, several approaches have been explored to address these issues, however, in this work we explored the incorporation of inorganic Si NWs with their superior mechanical, optical and electrical properties into the organic blend matrix. This incorporation of Si NWs aims to import the unique properties of individual NWs to enhance those of the overall formed hybrid structure leading to more stable hybrid structures with enhanced optical absorption, charge carrier mobility, electrical properties and the overall power conversion efficiency.

This work began with synthesis of the Si NWs using the well-studied MACE method for quick and effective fabrication of NWs. This part of the study was necessary to ensure that the morphology and other properties of the Si NWs are well investigated and understood before incorporating them in the hybrid matrix. Furthermore, this study exhibited and intricate correlation between a wide range of advanced characterisation techniques to explore the structural defects and their effects in Si NW properties and applications.

Microscopic analysis exhibited a semi-linear relationship between etching duration and length of Si NWs resulting in longer, rougher and less rigid structures with slightly bent tips. Further microscopic analysis revealed a presence of surface artefacts on the NW walls that could have influence on opto-electronic properties. The Si NWs displayed good anti-reflective properties and enhanced optical absorption at wavelength ranges suitable for solar PV applications. A combination of surface analysis and hall effect measurements conducted on the Si NWs confirmed successful doping with no correlation to NW length yet exhibiting an electron mobility trend analogous to that of bulk Si.

Following the successful fabrication of Si NWs which displayed great properties for PV application, it was imperative to explore the effect of these NWs when added into a P3HT:PCBM organic blend thin film. In this investigation, different amounts of Si NWs were loaded into the organic blend resulting in hybrid thin films of different NW load ratios. Morphological analysis revealed that at higher NW loads there is a formation of NW clusters leading to poor film morphology and in turn hamper the optical properties of the film. High-resolution microscopy analysis employed to investigate the NW – blend interface exhibited a clear interface on the outer shell without polymer diffusion into NW core as supported by the elemental line-scans conducted. Structurally, the addition of Si NWs did not exhibit any effects as observed from insignificant P3HT peak variations as shown by GIXRD analysis. The optical properties enhancement observed was attributed to the addition of Si NWs such that the 1:0.5 ratio exhibited the best UV-Vis absorption and PL quenching effect.

Chemical surface analysis of the samples produced inconclusive results since the Si signal was not observed from the hybrid as a result of limitations of the technique. However, the different Si NW load ratios could be traced and linked to the observed peak broadening of the S_{2p} peak. A proportional enhancement of electronic properties such as bulk concentration and conductivity was observed from the hall-effect measurements. Hybrid solar cell devices based on the different NW ratios also showed a great improvement in power conversion efficiency of about 49% increase to 1.2% PCE for the 1:1 device when compared to the polymer blend only sample with 0.8% PCE.

Having identified the ideal ratio for solar cell performance, this ratio was then used to investigate the effect of different dopant level of the Si NWs on the properties of the hybrid system. Opto-electronic analysis displayed that n-Si NWs introduced new

defect states which increased with dopant level resulting in the highly doped sample having the highest PL emission intensity. The change in dopant levels of the Si NWs exhibited no significant effect in optical absorption due to their sparse distribution and horizontal layout. However, significant effects of the dopant level in Si NWs was observed in charge-carrier transport properties whereby conductivity was significantly enhanced by the increase in dopant level owing to the one-dimensional structure and the additional charge carriers from the dopant. This enhancement in charge transport properties led to the enhancement of solar cell parameters such that the J_{sc} improved significantly with increase in dopant level owing to the enhanced conductivity and consequently resulting in the PCE increasing significantly with the dopant level.

These results demonstrate clearly that the unique properties of standalone Si one-dimensional NWs were successfully transferred and carried over to the organic-inorganic hybrid matrix resulting in a more efficient hybrid solar cell than the purely organic device as shown in the results.